Microstructure, Residual Stress, and Mechanical Properties of Thin Film Materials for a Microfabricated Solid Oxide Fuel Cell

by

David J. Quinn

B.S. Mechanical Engineering
Villanova University, 2002

M.Phil. in Engineering by Research
University of Cambridge, 2003

Submitted to the Department of Mechanical Engineering in Partial Fulfillment of the Requirements for the Degree of Master of Science in Mechanical Engineering

at the

Massachusetts Institute of Technology

June 2006

© 2006 Massachusetts Institute of Technology
All rights reserved

Signature of Author...
Department of Mechanical Engineering
May 24, 2006

Certified by...
Brian L. Wardle
Boeing Assistant Professor of Aeronautics and Astronautics
Thesis Supervisor

Certified by...
Sang-Gook Kim
Associate Professor of Mechanical Engineering
Mechanical Engineering Thesis Reader

Accepted by...
Lalit Anand
Chairman, Department Committee on Graduate Students

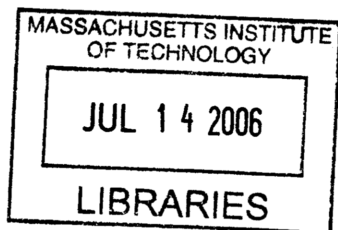
MASSACHUSETTS INSTITUTE OF TECHNOLOGY
JUL 1 4 2006
LIBRARIES

BARKER

Microstructure, Residual Stress, and Mechanical Properties of Thin Film Materials for a Microfabricated Solid Oxide Fuel Cell

By

David J. Quinn

Submitted to the Department of Mechanical Engineering on May 24, 2006 in Partial Fulfillment of the Requirements for the Degree of Master of Science in Mechanical Engineering

ABSTRACT

The microstructure and residual stress of sputter-deposited films for use in microfabricated solid oxide fuel cells are presented. Much of the work focuses on the characterization of a candidate solid electrolyte: Yttria Stabilized Zirconia (YSZ). Stress and structure of reactive RF sputtered YSZ films are explored as a function of thickness (5nm – 1000nm), deposition pressure (5mtorr – 100mtorr), and substrate temperature (room temperature, 300°C and 600°C). Microstructure is characterized by x-ray diffraction (XRD), transmission electron microscopy (TEM), and scanning electron microscopy (SEM). Film composition, specifically impurity content, is investigated with secondary ion mass spectroscopy (SIMS). Results indicate that YSZ films likely have a columnar structure with fully cubic crystalline phases of (100) texture with mixed amorphous/crystalline phases. Residual stress is measured via substrate curvature techniques. Results indicate that the as-deposited residual stress of YSZ ranges from -1.4 GPa to 400MPa with variations in sputtering conditions. Transitions from compressive to tensile stress are identified with variations in working pressure and film thickness. The origins and variations in as-deposited stress are determined to be from two primary mechanisms: tensile stress due to grain coalescence/growth and compressive stresses due to forward sputtering of target atoms (also known as "atomic peening" stresses). Due to the expected high-temperature operation (~1000°C) of microfabricated solid oxide fuel cells, the evolution of residual stress with post deposition thermal cycles is also explored. Results indicate significant stress hysteresis (nearly 1GPa tensile) for films deposited at room temperature and low working pressures with a transition from compressive to tensile stress beginning at approximately 150°C. This hysteresis is believed to be due to the diffusive relief of compressive stresses generated by "atomic peening" during deposition. In addition to stress and structure characterization, preliminary mechanical property characterization was completed through inferences made from stress-temperature cycles of films deposited under various conditions, and a series of nanoindentation tests on room-temperature YSZ films. Results indicate a low in-plane stiffness, believed to be the result of a mixed amorphous-crystalline structure, and an out of plane stiffness comparable to or higher than bulk properties, believed to be due to the texture of crystalline phases. Preliminary residual stress characterization of co-sputtered Pt-YSZ anode and cathode materials and fuel cell trilayers of Pt-YSZ/YSZ/Pt-YSZ is also presented. The implications of this work on the design and fabrication of structurally viable microfabricated solid oxide fuel cell devices are discussed.

Thesis Supervisor: Brian L. Wardle
Title: Boeing Assistant Professor of Aeronautics and Astronautics

Acknowledgements

Several people should be acknowledged for their part in contributing to the work of this thesis. On the technical side of things, first and foremost are my advisors: Prof. Mark Spearing and Prof. Brian Wardle, to whom I am of course forever grateful for their time, energy and guidance. I consider it a divine blessing to have met Mark while I was at Cambridge University and was humbled by his agreement to take me on as he and I both came back to MIT the following year. Despite being disappointed at Mark's decision after my first year to return to the UK to start a beautiful family, I am at the same time honored by Brian's willingness to take me on as one of his first students. Of course, the guidance of Profs. Klavs Jensen, Martin Schmidt, Harry Tuller and the other PI's on the MURI project was also essential in producing this work. In addition, I am forever indebted to Josh Hertz, Kevin Turner and Nathan Wicks for their technical and personal guidance in the last few years. Finally, like all graduate students at MIT, the assistance of various staff members has been essential in the completion of this thesis, including the staff in the Microsystem Technology Laboratories (MTL), the Center for Materials Science and Engineering, the Department of Mechanical Engineering and the Department of Aeronautics and Astronautics. In particular, I'd like to thank Leslie Regan, Joan Kravit, John Kane and Dave Robertson for their time and assistance.

On a more personal note, I cannot imagine having a better group of friends and acquaintances in my life. While too many to name individually, I feel compelled to cite Mike O'Brien, Robin Prince and Kathie Dionisio as well as the entire Dionisio family (including the family minivan) for their support. Their friendship was essential for me in finishing this thesis and it will no doubt out-live my memory of the facts and figures contained here.

Finally, while I offer everything I do in life up to God, I dedicate this particular piece of work to three people: Molly, who I cannot imagine myself without, and my parents, John and Kimberly Quinn, who are the rocks upon which all of my current and future success has been and will be built. I can only hope that I have turned out at least a little bit like them.

Contents

Chapter 1: Introduction and Motivation 13
1.1 Motivation for Microfabricated SOFCs (μSOFC) 14
1.2 Motivation of Thesis Work: Thermostructural Stability of μSOFC Membranes 17
1.3 Objectives and Scope of Thesis 18
Chapter 2: Background and Previous Work 23
2.1 Overview of the Sputtering Process 23
2.1.1 The Basic Sputtering Process 23
2.1.2 DC vs. RF Plasma Sputtering 25
2.1.3 Sputtering Process Characteristics: Yield, Deposition Rate and Uniformity 27
2.1.4 Additional Sputtering Configurations 28
2.1.5 Energetics of the Sputtering Process 29
2.2 Overview of Residual Stress Development in Sputtered Thin Films 31
2.2.1 Tensile Intrinsic Stress Mechanisms 32
2.2.2 Compressive Intrinsic Stress Mechanisms 34
2.2.3 Intrinsic Stress Due to Phase Changes and Precipitation 38
2.2.4 Influence of Temperature on Intrinsic Stress Development 38
2.3 Overview of the YSZ Materials System 39
2.3.1 General Characteristics of YSZ 39
2.3.2 Structure and Phase Characterization of Sputtered YSZ 41
2.3.3 Residual Stress in Sputtered YSZ 42
2.4 Implications of Residual Stress for Microfabricated Structures 43
2.5 Review of Residual Stress Measurement Techniques 45
2.5.1 Residual Stress Measurement by Substrate Curvature Techniques 45
Chapter 3: Experimental Procedures 56
3.1 Sputter Deposition of YSZ and Pt-YSZ Thin Films 56
3.1.1 Sputtering Apparatus and Procedure 56
3.1.2 YSZ Deposition Conditions, Rates and Uniformity 58
3.1.3 Conditions and Characterization of Pt-YSZ Deposition 60
3.1.4 Characterization of Substrate Heating During Deposition 61
3.2 Residual Stress Measurement of Deposited Films 62
3.2.1 Wafer Curvature Measurements 63
3.2.1.1 Calibration of the Curvature Measurement System 64
3.2.2 Uncertainty Analysis of Residual Stress Measurements 66
3.3 Material, Microstructure and Composition Characterization Techniques 68
Chapter 4: Residual Stress and Microstructural Characterization of μSOFC Materials 79
4.1 Characterization of YSZ Films Sputtered at Room Temperature 79
4.1.1 Microstructure and Compositional Characterization 80
4.1.2 As-Deposited Residual Stress Characterization 81
4.1.2.1 Effect of Film Thickness 82
4.1.2.2 Effect of Working Pressure 85
4.1.3 Residual Stress Evolution With Post-Deposition Thermal Cycling 86
4.2 High-Temperature Sputtered YSZ Films 93
4.2.1 Microstructural Characterization 93
4.2.2 Effect of Deposition Temperature on Residual Stress 94

4.2.3 Effect of Film Thickness 96
4.2.4 Effect of Working Pressure 96
4.2.5 Residual Stress Evolution With Post-Deposition Thermal Cycling 96
4.3 Preliminary Residual Stress Characterization of μSOFC Structures 98
4.3.1 Anode/Cathode Material: Pt-YSZ 98
4.3.2 Fuel Cell Trilayer: Pt-YSZ/YSZ/Pt-YSZ on Si 99
4.3.3 Fuel Cell Trilayer: Pt-YSZ/YSZ/Pt-YSZ with Ti adhesion layer on SiN/Si 100
4.4 Conclusions 101
Chapter 5: Mechanical Property Characterization of Sputtered YSZ Thin Films 136
5.1 Polycrystalline YSZ: Aggregate Mechanical Properties and Influence of Crystallographic Texture 137
5.2 Mechanical Property Estimates Based on Thermal Cycling Data 141
5.2.1 Biaxial Modulus and Coefficient of Thermal Expansion (CTE) 141
5.2.2 YSZ Strength Properties 144
5.3 Nanoindentation Tests of Sputtered YSZ 144
5.3.1 Background on Nanoindentation Testing 145
5.3.2 Experimental Methods 149
5.3.2.1 Test Apparatus 149
5.3.2.2 Sample Preparation and Test Conditions 150
5.3.2.3 Results 151
5.4 Conclusions 153
Chapter 6: Conclusions and Recommendations for Future Work 164
6.1 Summary of Results and Contributions 164
6.2 Implications for μSOFC Device Design and Fabrication 168
6.3 Recommendations for Future Work 169
References 173

List of Figures

Figure 1-1: Operating principles of a solid oxide fuel cell (adapted from [2, 14])....................... 21
Figure 1-2: Examples of various failures in representative micro-SOFC device structures: (a) a buckled membrane, (b) a multilayered structure with apparent delamination of underlying layers, (c) a multilayered structure that has catastrophically fractured during heating and (d) an unreleased film with patterned electrodes that has cracked during a thermal cycle. 22
Figure 2-1: Schematic view of typical diode sputtering process. The interactions occurring between the anode and cathode, separated by a working distance d, illustrate incident sputtering atoms, ejected target material and secondary electrons in addition to the presence of sputter gas neutrals. 48
Figure 2-2: Characteristic regions of plasma during sputtering (adapted from [15]). Note that V_{DC} represents the applied voltage in DC sputtering and the DC bias component of the applied voltage in RF sputtering. 49
Figure 2-3: Emission profiles for varying sputtering energy (adapted from [16]). Marker density is proportional to concentration of material, indicating more material deposited at higher and lower angles from the normal for low and high energy bombardments, respectively... 50
Figure 2-4: Development of tensile stress during grain coalescence (adapted from [31]). 51
Figure 2-5: Illustration of the atomic peening process. Interstitials arise from implanted gases and/or the collisions of reflected neutrals (here Ar) and sputtered atoms with film surface atoms. 52
Figure 2-6: Crystal structures of zirconia: (a) cubic (FCC), (b) tetragonal, (c) monoclinic. Lattice sites are occupied by the cation (Zr,Y). 53
Figure 2-7: Representative design space for μSOFC membranes considering the failure modes of linear-elastic buckling and fracture (adapted from [64]). 54
Figure 2-8: Line scan techniques for wafer curvature measurement: (A) scanning stylus, (B) capacitance probe, and (C) scanning laser system (adapted from [23]). 55
Figure 3-1: Schematic of Kurtis Lesker sputtering system used in this work (top and side-view). 70
Figure 3-2: Thickness measurements vs. deposition time under standard deposition conditions. Error bars indicate maximum and minimum measurement values. (Position B data provided by J. Hertz).. 72
Figure 3-3: YSZ Deposition rate vs. working pressure, all other deposition conditions standard. Error bars indicate maximum and minimum values. 73
Figure 3-4: Uniformity profiles of YSZ films deposited under standard conditions. Error bars represent minimum and maximum from at least 5 profilometry measurements. 74
Figure 3-5: Substrate heating during YSZ deposition at room temperature (and standard conditions).. 76
Figure 3-6: (a) Picture and (b) schematic of Tencor FLX wafer curvature measurement system (schematic taken from [79]).. 77
Figure 3-7: Comparison of curvatures measured with old and new/corrected calibration files... 78
Figure 4-1: Typical SIMS depth profile for room temperature, standard condition, as-deposited YSZ films on Si. 103
Figure 4-2: TEM images of two different YSZ films deposited under standard conditions. Images indicate columnar growth and slight widening of grains through thickness. Image (b) provided by J. Hertz. 105

Figure 4-3: X-Ray diffraction profile of YSZ film deposited at room temperature under standard conditions along with peak locations of randomly oriented cubic and tetragonal structures. Peaks indicate purely cubic structure and possible (200) film texture. 106
Figure 4-4: Total measured residual stress vs. thickness for room YSZ films deposited at room temperature and standard conditions over two time periods. Error bars indicate estimated uncertainty as discussed in section 3.2.2. 108
Figure 4-5: SIMS profiles for trace (a) Ca, (b) Na, (c) Al, and (d) Ti impurities in room-temperature deposited YSZ films over two time periods. 109
Figure 4-6: Planar view SEM images of room temperature YSZ films deposited at standard conditions of thicknesses of 62nm, 240nm, 500nm and 988nm. Increasing sizes of grain clusters with film thickness, as well as larger individual grains, supports the hypothesis of tensile stress generation mechanisms with increasing film thickness. 111
Figure 4-7: AFM Z-height images of YSZ films deposited under standard conditions with thicknesses of (a) 240nm, (b) 560nm, and (c) 988nm. 112
Figure 4-8: AFM image of a 560nm film after applying a high pass filter and flattening routine to accentuate contrast at grain boundaries. 113
Figure 4-9: Grain size vs. film thickness for room temperature YSZ films deposited under standard conditions as determined by AFM image measurements. Error bars cover ± one standard deviation of a minimum of 7 average measurements. 114
Figure 4-10: Total measured residual stress in YSZ films deposited under varying working pressure but otherwise standard conditions. Error bars indicate estimated uncertainty as discussed in section 3.2.2. 115
Figure 4-11: Total residual stress vs. temperature during post-deposition thermal cycles for a 241nm thick YSZ film deposited at standard conditions. Data indicates a shift in the intrinsic stress component beginning at approximately 150°C. Stress evolution and hysteresis is typical of all room-temperature deposited samples. 116
Figure 4-12: Residual stress vs. post deposition temperature for the first temperature cycle of several samples deposited under standard conditions and comparable thicknesses (249-295nm). 117
Figure 4-13: XRD profiles of as-deposited (top) and post thermal cycle (bottom) films. Both scans indicate purely cubic phase with slight increases in peak intensities and peak shifting. 118
Figure 4-14: SIMS Argon concentration profiles for as deposited, 500°C (1 hr @ 5 °C/min) and 1000°C (4hr @ 10 °C/min) anneals. 119
Figure 4-15: Diffusion coefficients for FCC metals given by Ohring [18]. 120
Figure 4-16: Residual stress vs. post deposition pressure for films deposited at room temperature under varying working pressure (film thicknesses within 250nm-350nm, all other conditions standard). 121
Figure 4-17: XRD profile of films deposited under room temperature (top) and 600°C substrate temperature (bottom). 123
Figure 4-18: AFM images of YSZ films deposited at (a) room temperature and (b) 600°C substrate temperature. 124
Figure 4-19: Total measured stress vs. substrate temperature for depositions at 10mTorr and 20mTorr working pressures. 20mTorr samples were deposited during the series 1 time period. 10mTorr samples were deposited during the series 2 time period . Film thicknesses are typically between 250nm-350nm. All other conditions are standard. 125

Figure 4-20: SIMS profiles for trace (a) Ca, (b) Na, (c) Al, and (d) Ti impurities in high-temperature deposited YSZ films. 126
Figure 4-21: Total residual stress versus film thickness in YSZ deposited with a substrate temperature of 600°C. 128
Figure 4-22: Total residual stress versus working pressure of deposition for YSZ films deposited with a substrate temperature of 600°C. Error bars indicate estimated uncertainty as discussed in section 3.2.2. 129
Figure 4-23: Total residual stress vs. post deposition anneal temperature for a high-temperature deposited (600°C) film. 130
Figure 4-24: Total residual stresss in a co-sputtered Pt-YSZ composite film versus post-deposition temperature. 131
Figure 4-25: Total average residual stress in a trilayer stack of Pt-YSZ/YSZ/Pt-YSZ on Si versus post deposition temperature. 132
Figure 4-26: Residual stress of 20nm Ti film versus post deposition temperature. Results indicate that the film is not continuous or has delaminated. 133
Figure 4-27: Total average stress of Pt-YSZ/YSZ/Pt-YSZ stacks (layer thickness approximately 250nm each) with Ti a stacks on an Si wafer coated with silicon nitride. Data indicates that the final stress state may be (a) mildly tensile or (b) compressive. 134
Figure 4-28: Total average residual stress versus post-deposition temperature for a Pt-YSZ/YSZ/Pt-YSZ/Ti stack of increased Ti film thickness deposited on an Si wafer coated with silicon nitride. 135
Figure 5-1: Relevant crystal directions and planes for (100) textured cubic crystals. 155
Figure 5-2: Residual stress vs. post deposition temperature of two room temperature YSZ films. Films crack during cool-down, allowing for inference of film strength. 157
Figure 5-3: Cracking of thermally cycled YSZ film (Sample B from Figure 5-2). 158
Figure 5-4: Modulus of elasticity vs. max indentation load for YSZ films sputtered under standard conditions. Data points are averages of a minimum of 35 indents. Error bars indicate one standard deviation. 160
Figure 5-5: Modulus vs. maximum indentation depth for YSZ films sputtered at standard conditions and tested by nanoindentation. Error bars indicate one standard deviation. 161
Figure 5-6: Inferred cross-sectional view of microstructure of room temperature sputtered YSZ films with mixed amorphous and columnar crystalline phases. (Not to scale) 163

List of Tables

Table 3-1: Standard deposition conditions for YSZ. 71
Table 3-2: Deposition conditions for Pt-YSZ films. 75
Table 4-1: Compositional characterization of YSZ films deposited under standard conditions. Error in SIMS characterization is quoted as ± 10-20%. WDS results provided by J. Hertz [77]. 104
Table 4-2: Bulk material properties. 107
Table 4-3: Compositional characterization of films deposited at room and elevated substrate temperatures (WDS data provided by J. Hertz). 122
Table 4-4: Thickness and stress characteristics of sputtered Ti adhesion layers. 133
Table 5-1: Slopes of thermal cycling curves of YSZ films deposited under various conditions. 156
Table 5-2: Load frame compliances and area functions of nanoindentation tests performed. ... 159
Table 5-3: Elastic Modulus of YSZ films indented at shallow depths and analyzed with the experimental and ideal sphere area functions 162

Chapter 1: Introduction and Motivation

Techniques for creating portable power sources with high power densities have received much attention in recent years. In addition to improvement of traditional battery (*e.g.* lithium ion, or metal hydride) technologies, some researchers have focused on the development of power sources using alternative techniques, including those based on hydrogen fuel cells. Hydrogen and hydrocarbon fuels have comparable or higher chemical energy densities (~5 – 35 MJ/kg) compared to materials used for traditional battery technologies (~5 MJ/kg for complex and chemical hydrides) as well as the potential for high efficiencies for electrical power conversion , for example, up to 70% fuel to electrical power efficiencies have been projected for macro-scale fuel cell systems when integrated with turbines [1-3].

The exploration of fundamental science and engineering issues related to the development of portable, micro-chemical power (μCP) devices is the subject of work being done by an interdisciplinary team at the Massachusetts Institute of Technology (MIT) as part of a Multidisciplinary University Research Initiative (MURI) sponsored by the Army Research Office (ARO). One of the focused efforts within the μCP MURI team is the examination of fundamental issues related to the development of a microfabricated solid oxide fuel cell (μSOFC) for use in devices/systems with power requirements on the order of 0.1-10W (*i.e.* portable electronic device applications). This thesis represents a contribution to the μSOFC development effort in the way of enhanced understanding of the structural characteristics and mechanical properties of likely μSOFC materials. Specifically, this thesis focuses on microstructural and residual stress characterization of μSOFC materials and interpreting these results in the context of specific mechanisms of stress/microstructure evolution. These results

and understanding will guide the design of device architectures and microfabrication routes for structurally viable, electrochemically optimized μSOFC devices. The remainder of this chapter establishes the motivation and framework for μSOFC devices and the need for enhanced understanding of stress/structure properties of μSOFC materials, followed by an overview of the remainder of this thesis.

1.1 Motivation for Microfabricated SOFCs (μSOFCs)

In the most general sense, fuel cells[i] are electrochemical devices that combine hydrogen and oxygen to form water, electrical current and heat. Different types of fuel cells exist and provide for a wide range of operating conditions and potential fuels. The different types of fuel cells are well-reviewed in the literature [1-3]. Solid oxide fuel cells are a class of fuel cell devices utilizing a dense ceramic electrolyte capable of conducting gaseous ions, typically oxygen, at elevated temperatures (frequently ~ 600°C or greater). This electrolyte is sandwiched between two electrode catalysts promoting the necessary reactions for the production of an electrical current. A schematic representation of this process is presented in Figure 1-1. At elevated temperatures and in the presence of the catalyst (*e.g.* Ni or Pt), fuel at the anode side of the cell is oxidized to produce electrons and hydrogen ions (*i.e.* protons). This reaction, site A in Figure 1-1, is:

$$H_2 \rightarrow 2H^+ + 2e^- \quad (1\text{-}1)$$

At the cathode, oxygen is reduced by a catalyst (*i.e.* Pt or lanthanum strontium manganite (LSM)) to give oxygen ions which flow through the ion conducting solid oxide electrolyte and

[i] For this discussion and the remainder of this thesis, fuel cell systems under consideration are limited to those using hydrogen-based fuels (*i.e.* pure hydrogen, hydrocarbons etc.). No consideration is made of zinc-air fuel cell systems.

combine with the hydrogen ions at the anode to form water. The relevant reactions at locations B and C in Figure 1-1 are, respectively:

$$2H^+ + O^{2-} \rightarrow H_2O \tag{1-2}$$

$$\frac{1}{2} O_2 + 2e^- \rightarrow O^{2-} \tag{1-3}$$

The catalytic reactions at sites A and C occur at the interface between the electrolyte, anode/cathode and fuel/oxidant. This interface makes up a "triple phase boundary" (TPB). The anode and cathode materials are often times highly porous in order to increase the length of this triple-phase boundary and improve reaction rates. In competing proton exchange membrane (PEM) technologies, a similar process takes place, with the distinguishing feature being the conduction of hydrogen ions (*i.e.* protons) through a polymer electrolyte at lower temperatures (~90 – 100°C).

One advantage of solid oxide fuel cells over competing fuel cell systems is fuel versatility. Compared to competing fuel cell devices, such as proton exchange membrane fuel cells (PEMFC's) which are typically made of polymers that are poisoned by the presence of contaminants such as carbon monoxide, SOFC's require significantly less fuel processing and purification, allowing for a wider range of hydrocarbon fuels to be used, possibly eliminating the need for fuel processing completely through the introduction of steam with the fuel at the anode [2]. This steam is readily available from the overall reaction products because of the high temperature of operation. In macro-scale systems, similar integration of the hot gaseous exhaust of SOFC's with turbine systems have allowed for overall fuel to electrical power conversion efficiencies of 57% with projected efficiencies with continued work approaching 75% [1-3].

In addition to the general performance advantages of SOFC's discussed above, there are several factors that make SOFC's attractive devices for microfabricated, portable power generation systems. One motivating factor for μSOFC's is the reduction of the thermal mass of the system to help avoid typical issues of long start up times associated with raising the system to the required temperature. Another motivation for the use of microfabrication/MEMS technologies in the development of μSOFC's is the potential for tailoring and increasing the triple phase boundary length at the anode and cathode to improve overall electrochemical performance. There is also the possibility of improved electrochemical performance through the use of a thinner electrolyte layer. Thinner electrolytes (as well as thinner anode and cathode layers) decrease the internal electrical/ohmic resistance of the fuel cell stack, thus improving the net power output. Perhaps more important, however, is the potential for improved ionic conductivity with reduced thickness or, alternatively, the potential for maintaining adequate ionic conductivity and reducing the operating temperature of the fuel cell. This possibility was explored by Steele, who proposed that the typical operating temperature of the most common electrolyte material (yttria stabilized zirconia, YSZ) may be reduced from ~800-1000°C down to ~600°C using electrolyte thicknesses on the order of ~1μm [4-6].

These potential advantages of SOFC's in portable power applications have been noted by several others attempting to develop microfabricated SOFC materials and devices [7-12]. These efforts have been successful in demonstrating the potential for power densities ranging from 0.1 W/cm^2 – 1 W/cm^2. However, long-term power stability is a noted problem with these devices. Although not discussed in much detail in that work, such instabilities are likely related to contamination of anodes and cathodes (*i.e.* coking where Ni-based anodes are used) and possible structural degradation of the electrolyte and electrodes. Also, it is important to realize that these

"devices" are not fully packaged and self-contained. It is generally accepted that the issues involved in packaging SOFC devices, such as thermal isolation, are substantial. Addressing such packaging issues are a parallel effort in the MIT μCP MURI. As established below and in later chapters, results from this thesis serve to help guide overall device design, fabrication and packaging routes.

1.2 Motivation of Thesis Work: Thermostructural Stability of μSOFC Membranes

Many of the technical limitations and hurdles associated with the development of SOFC's at both the macro and micro scales are inherently linked to the high operating temperatures (600-1000°C) of SOFC systems. This requirement complicates the issues of thermal management for optimal net power output, the need for fast start-up time and thermostructural stability[ii] of the SOFC device. The last of these is the major motivating factor for the work contained in this thesis. Traditional fuel cell architectures are multilayered membrane structures comprised of different classes of materials (*i.e.* low tensile strength ceramic oxides and metals) with differing mechanical properties, most notably differing coefficients of thermal expansion (CTE). In addition to the CTE mismatch of individual layers, there is also the possibility of a net CTE mismatch between the fuel cell stack and the supporting structure/package. Matching the CTE's of the fuel cell materials is difficult due to the limitations imposed by electrochemical requirements of the anode/electrolyte/cathode materials as well as the high oxidation environment and possibility of reactions between the anode/cathode and electrolyte materials.

[ii] For this thesis, the term "thermostructural stability" will be used to describe the general mechanical and structural viability of a fuel cell structure. This is distinguished from crystallographic structural phase stability in the material science literature and the strict definition of elastic stability (*i.e.* buckling) in mechanics and structures literature.

Thus, the mismatch strains/stresses generated by these architectures at elevated temperature limit the thermostructural stability of released membrane structures.

At the macroscale, the most effective way of reducing the effects of these mismatch strains/stresses has been the introduction of axisymmetry through the construction of concentric tubular SOFC's. However, such tube structures are generally not possible through typical microfabrication routes where the vast majority of processes are planar in nature. Thus, microfabricated fuel cell structures ultimately require the deposition of the fuel cell stack materials onto either a sacrificial membrane structure or onto a bulk substrate which is then etched to release the fuel cell stack. Such structures are subject to a host of possible failure modes, including buckling of membranes, catastrophic structural failure of layers in the structure, delamination of individual layers and the cracking of deposited films/layers. In preliminary work done during the MURI program, all such failure modes have been observed in the fabrication of device-level structures during μSOFC development. Examples of these observations are shown in Figure 1-2. Avoiding such failures necessitates the development of different levels of thermostructural analysis which all depend on knowledge of the mechanical properties and residual stress state of fuel cell materials. Inherently linked to both characteristics is the film microstructure. These observations and requirements motivate the work presented in this thesis.

1.3 Objectives and Scope of Thesis

The general objective of this thesis is to experimentally characterize the microstructure, mechanical properties and residual stress state of materials for a μSOFC. As mentioned previously, the generic μSOFC device architecture is that of an electrolyte membrane sandwiched between two porous anodes/cathodes. This porosity may significantly reduce the

structural effect of the anode/cathode layers. Therefore, to first order, the properties of the electrolyte layer will control the mechanical response of the SOFC membrane structure. This thesis focuses predominantly on investigating the properties of the most likely electrolyte material: sputter-deposited yttria stabilized zirconia (YSZ). Generally, YSZ has been a focus in the MURI program because it is the most common electrolyte material at the macro scale (in large part due to cost and availability). Furthermore, at the outset of this work, the YSZ deposition process was the most advanced process/material system being investigated within the MURI initiative capable of producing large-area (greater than 1cm x 1cm) films free of cracks after deposition and capable of adhering to standard substrate and underlying film materials (*i.e.* silica, silicon, silicon nitride). As such, it was believed that YSZ would be most easily integrated into a μSOFC device fabrication route. Previous work done in the MURI initiative firmly established the presence of residual stress in sputtered YSZ as a major contributing factor to the stability of SOFC membrane structures [13]. It is well-known that the residual stress state of thin films is inherently linked to the microstructure of the material. Therefore, the main objectives of this thesis are:

- Characterize the as-deposited residual stress state in sputtered YSZ with variations in processing conditions.
- Characterize the evolution of residual stress with post-deposition thermal cycles to elevated temperatures.
- Identify the dominant mechanism(s) of residual stress development and evolution by coupling residual stress characterization with microstructural characterization.
- Provide a preliminary assessment of the thermoelastic properties of sputtered YSZ films.

- Identify the implications of as-deposited stress, stress evolution with temperature and mechanical property assessment on μSOFC device architectures and fabrication routes.

The approach taken for meeting these goals is almost entirely experimental. Considering the need for a broad range of information in the development of μSOFC devices, the experimental approach focused on gaining insight using readily available testing methods and apparatus, rather than designing and developing original techniques and test apparatus which would have reduced the knowledge gained in the time available. In Chapter 2, the necessary background on the sputtering process, the YSZ material system and stress evolution in sputtered films is established. This is followed by the experimental procedures (Chapter 3) used in the characterization of stress and structure presented in Chapter 4. In addition to work done on sputtered YSZ, sections in Chapter 4 also contain preliminary work done on the residual stress characteristics of a novel anode/cathode material (co-sputtered Pt-YSZ) as well as the behavior of representative fuel cell trilayers comprised of Pt-YSZ/YSZ/Pt-YSZ stacks. Chapter 5 contains a preliminary assessment of mechanical properties of YSZ films using inferences from stress vs. temperature experiments as well as data from a series of nanoindentation tests intended to guide future mechanical property characterization work. Chapter 6 summarizes the results from this thesis, highlights the major contributions, discusses their implications for μSOFC device development and provides suggested directions for future work.

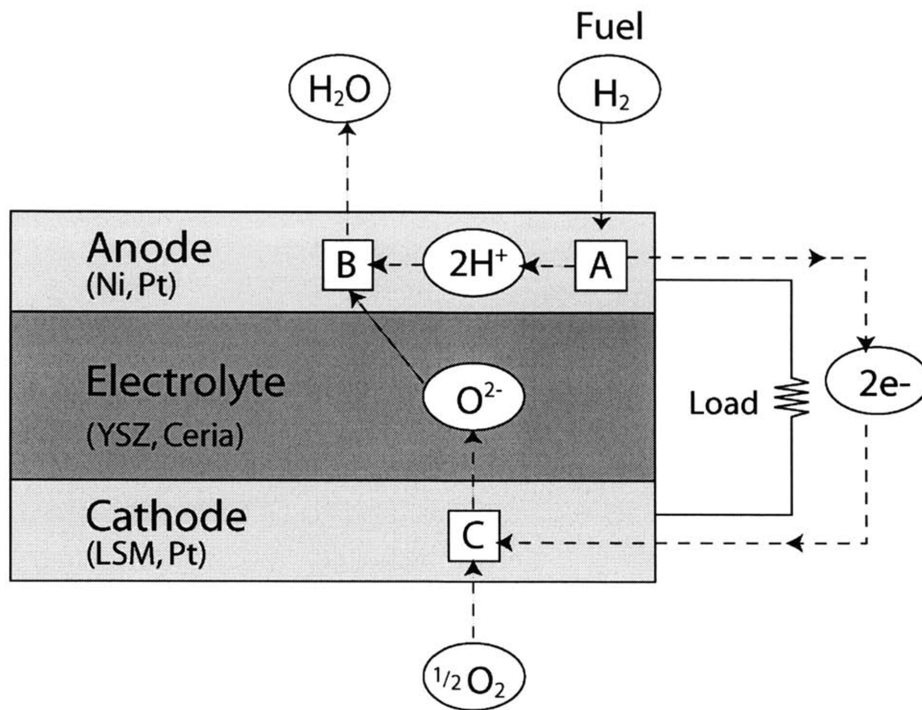

Figure 1-1: Operating principles of a solid oxide fuel cell (adapted from [2, 14]).

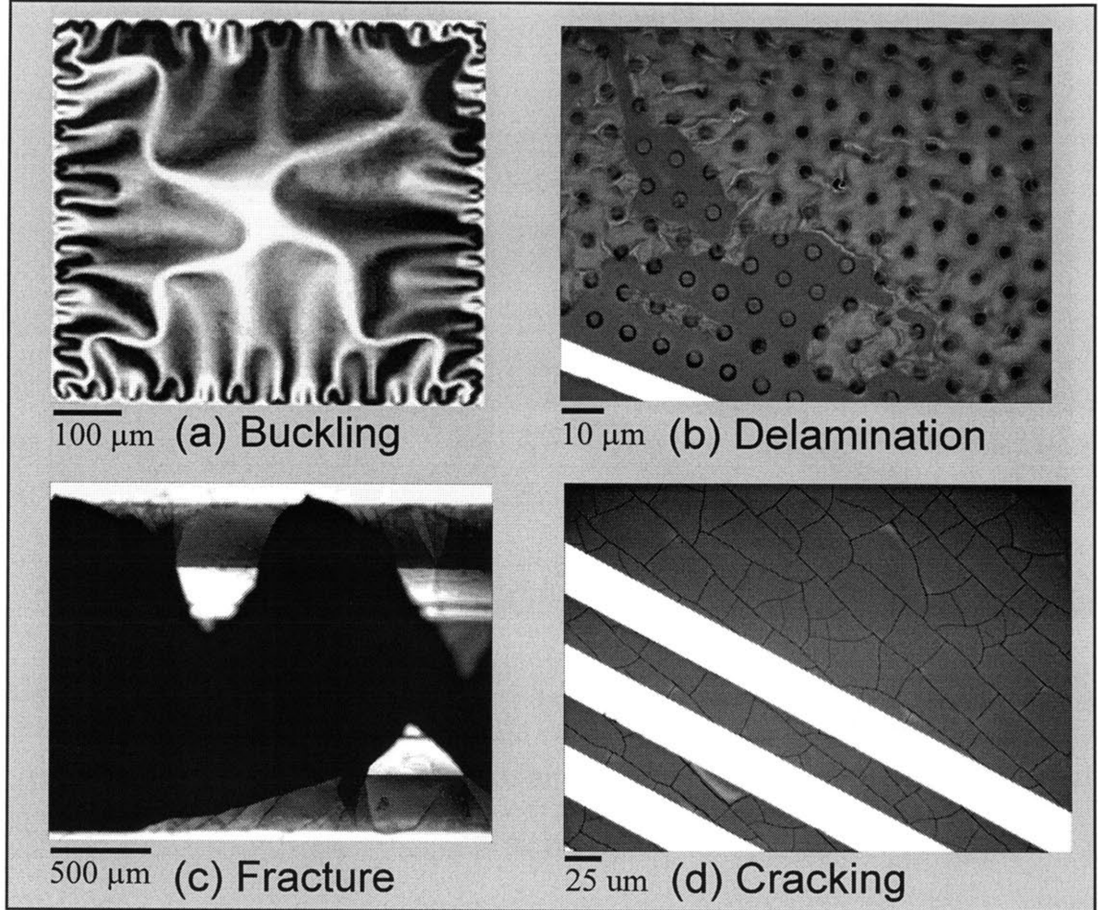

Figure 1-2: Examples of various failures in representative micro-SOFC device structures: (a) a buckled membrane, (b) a multilayered structure with apparent delamination of underlying layers, (c) a multilayered structure that has catastrophically fractured during heating and (d) an unreleased film with patterned electrodes that has cracked during a thermal cycle.

Chapter 2: Background and Previous Work

Much of the work presented in this thesis involves thin films prepared by sputter deposition processes. Therefore, it is important to first give an overview of the critical aspects of the process. This will be followed by an overview of residual stress generation mechanisms in sputter-deposited films and results from the most relevant work done to date for yttria stabilized zirconia (YSZ) films, the most prevalent material examined by this thesis. Finally, a survey of residual stress measurement techniques is presented.

2.1 Overview of the Sputtering Process

The following sections review the relevant aspects of the sputter deposition of thin films. First, a basic overview of the physical processes involved in sputter deposition is presented, followed by a description of the distinguishing characteristics of DC and RF sputtering and important process characterization parameters. Finally, an overview of the energetics of the sputtering process and the influence of process conditions on the relevant energy quantities is presented. In these discussions, the focus is on conditions that most influence film structure and residual stress in processes most relevant to this thesis, where RF magnetron, reactive, unbiased sputtering is used.

2.1.1 The Basic Sputtering Process

Sputter deposition is a member of a class of physical vapor deposition (PVD) processes for thin films. Like other members of this class of deposition processes such as thermal and electron-beam evaporation, sputtering relies on a physical process to produce the deposited film, rather than a series of chemical reactions such as those prevalent in chemical vapor deposition

(CVD) and wet physical processes (*e.g.*, sol-gel methods). In evaporation processes, the physical process is the vaporization of material that has been elevated to sufficiently high temperature. In sputtering, the physical process involved is ejection of the film material from a target through bombardment by energized gas particles.

The classical configuration of a plasma sputtering system is shown schematically in Figure 2-1. In this system, two parallel electrodes in a low pressure, typically 1 – 100mTorr, inert gas atmosphere are separated by a distance on the order of a few to tens of centimeters ("d" in Figure 2-1). A DC or AC voltage on the order of several kV applied to the electrodes creates an electric field large enough to cause dielectric breakdown and ionization of the surrounding inert gas. Ions are accelerated toward the cathode electrode (*i.e.*, the target) at a large enough energy to eject the target material. In a sputter-deposition process, the cathode/target is made up of the material to be deposited, whereas in a sputter etching process such as ion milling, the cathode/target contains the material/substrate to be removed.

In addition to the ejected target material, a host of other particles may be emitted from the target, such as reflected gas atoms, x-rays, photons and secondary electrons. The emission of secondary electrons is important for maintaining the sputtering process. In addition to the free electrons created during ionization of the inert gas, secondary electrons help create an "avalanche" of energizing and ionizing collisions that make up and sustain the plasma while giving it a characteristic glow. Deposition progresses as ions continue to be accelerated toward the cathode target. While a detailed description of the physics and design of sputtering systems is beyond the scope of this thesis, relevant aspects of these areas will be covered for a more complete understanding of previous work and the work presented here. Much of the material

presented in this section has been drawn from overviews given by Madou [15], Rossnagel [16], Hopwood [17] and Ohring [18].

2.1.2 DC vs. RF Plasma Sputtering

Discussions of plasma sputtering systems are typically divided according to the use of either a direct current (DC) or radio frequency (RF) power source. DC sputtering systems typically require conductive target/deposited materials so as to produce enough free electrons to sustain the plasma. In a typical DC system, the initial supply voltage across the electrodes is around 150kV when using an argon atmosphere in the pressure range of 0.001 – 10 Torr. The initiation of gaseous breakdown and plasma generation creates a discharge current on the order of 100's mA, dropping the potential difference between the electrodes to the order of 150V [15]. At this point, the plasma between the electrodes is composed of three characteristic spatial regions: the cathode sheath, the glow and the anode sheath. These regions, along with their characteristic voltage drops are depicted in Figure 2-2. As depicted in the figure, V_{DC} is the cathode voltage and V_P is the plasma voltage in the glow region.

The cathode sheath, also known as the cathode "dark space" with a potential difference of $V_{DC} - V_P$, is the negatively charged area near the cathode attracting the positively charged gaseous ions responsible for material ejection. The greatest potential drop across the electrodes occurs in this region. The glow region is where ionization is maintained. In this region there exists a net positive, relatively constant, charge (and voltage V_P) due to electron loss to the walls which is explained by kinetic theory [15, 17].

The positively charged anode sheath/dark space, with a voltage drop of V_P to ground, absorbs free electrons from the plasma. In a manner similar to e-beam evaporation, this bombardment with free electrons leads to substrate heating during a deposition process. This

heating effect is minimized in modern sputtering processes through the use of a *magnetron* sputtering system. In these systems, permanent magnets placed below the cathode create a magnetic field perpendicular to the applied electric field. The effect of these crossed fields is to force electrons into tight helical paths near the cathode. This has two important results: (1) ionizing collisions between electrons and gas neutrals become more likely due to an increased path length, resulting in higher plasma density and (2) electrons arrive at the anode (*i.e.*, substrate) with lower energy, thus reducing the substrate heating effect.

RF systems share many characteristics of DC systems, with the major difference being the use of an RF power source at 13.56 MHz[iii] that applies an AC voltage between the electrodes. The resulting oscillating field excites free electrons thus promoting ionizing collisions and reducing or eliminating the dependence on secondary electrons for a sustained plasma. An important result of this phenomenon is the ability of RF-generated plasmas to deposit/etch dielectric materials with fewer free electrons than the conductive materials typically required for DC plasmas. The three characteristic potential regions described for DC plasmas and shown in Figure 2-2 also make up the space between electrodes for RF plasmas. In the application of alternating voltage to the cathode, charge builds up to create a DC bias, also called "self-biasing". This bias component (V_{DC} in Figure 2-2) of the applied RF voltage is responsible for the acceleration of inert gas ions toward the target.

An important component of the RF system is the circuit accompanying the RF power source. The RF system is designed to operate under a specific load resistance, typically 50 Ohms. Since the impedance associated with the potential drops across the electrodes will change with target material and processing conditions such as pressure, an "impedance matching" circuit

---

[iii] This frequency is standard as it is free from interference from radio transmissions.

is used to give the required resistive load [17]. This circuit consists of a fixed inductor and capacitor in series with a parallel shunt capacitor.

Finally, an important variation on the sputtering process described thus far is *reactive* sputtering processes. In reactive sputtering, a gas in addition to the inert plasma gas (typically Ar) is introduced into the chamber. The target material reacts with this second gas prior to deposition on the anode/substrate, thus allowing for the deposition of compounds such as oxides and silicides. The exact mechanism for this reaction is not well understood. A proposed model is given by Berg et al. [19]. It is hypothesized that at lower working pressures (*i.e.,* less than 10mTorr), the reaction takes place upon arrival at the substrate, whereas higher pressure promotes the reaction at the target. In either case, reactive sputtering of a target of the appropriate composition allows for good stoichiometric control in the production of complex compounds.

2.1.3 Sputtering Process Characteristics: Yield, Deposition Rate and Uniformity

A standard quantity used to characterize the sputtering process for a given material and sputtering conditions is the sputter yield (S). Defined as the number of atoms removed per incident ion, this quantity is typically proportional to deposition rate. For metal targets sputtered in argon, the sputter yield ranges from 0.1 – 5 but is typically between 0.5 – 2. Generally, the amount of material in atoms (W) sputtered from the cathode is proportional to the sputter yield and is related to the working voltage (V), discharge current (i), working anode/cathode distance (d), and sputtering gas pressure (P) by

$$W = \frac{KVi}{Pd} \tag{2-1}$$

Where K is a proportionality constant [15]. Compared to evaporative techniques, sputtering processes typically have very low deposition rates (one atomic layer per second for sputtering vs. thousands per second for evaporation), allowing for greater control of very thin (*i.e.* submicron) films.

The emission profile of sputtered material varies with process energetics and cathode voltage. Characteristic profiles are shown in Figure 2-3. Generally, emission profiles for sputtered materials can roughly be described according to a cosine distribution law [16, 18]: deposition rates vary with the cosine of the angle (θ in Figure 2-3) from the normal. However, lower cathode voltage/energy depositions typically give rise to more material sputtered away at higher angles from the normal. Conversely, higher voltage/energy depositions produce more sputtered material at or near the target normal than that predicted by the cosine law.

2.1.4 Additional Sputtering Configurations

Sputtering systems and phenomenon described thus far have been focused on diode (*i.e.*, two electrode) systems with planar anode and cathode. Other configurations do exist, including triode systems, cylindrical and hollow cathode systems as well as ion beam sputtering, where the sputtering energy is supplied by a controlled inert gas ion bombardment rather than a plasma. These configurations may also be combined with ion bombardment for ion-assisted deposition processes. However, the most common additional feature for a sputtering system beyond that described thus far is the availability of an applied substrate/anode voltage bias. In these systems, a negative voltage is applied to the anode/substrate in order to induce higher levels of substrate bombardment via attraction of ionized gas atoms. The effects of this bombardment on resulting film structure and properties are discussed below.

2.1.5 Energetics of the Sputtering Process

It is widely recognized that the resultant structure and properties of sputtered films are determined largely by the energetics of bombardment associated with the sputtering process [20]. It has been shown that gas ions are neutralized and retain a large portion of their energy when reflected from the target [20, 21]. These back-reflected neutral atoms, combined with the sputtered atoms and secondary electrons are the three most important sources of film bombardment in an unbiased, diode sputtering process such as that used in this work (when applied substrate biases are used, inert gas ions are attracted to the substrate for an additional source of bombardment). Of these particles, secondary electrons are recognized to be the primary source of substrate heating but do little to alter film structure [20]. On the other hand, sputtered atoms and back reflected neutrals both give rise to a bombardment energy that affects the evolution of film structure and properties.

The total bombardment energy (E_t) in the case of unbiased deposition is proportional to the sum of the energy of sputtered atoms (ε_s) and back-reflected neutrals (ε_r) and has been quantified according to the following relationship [20]:

$$E_t = \frac{R\varepsilon_r + S\varepsilon_s}{\alpha} \qquad (2\text{-}2)$$

Where α is the sputtering energy efficiency (fraction of incident ion energy transferred to the target), S is the sputter yield, and R is the particle reflection coefficient (ratio of reflected and incident flux). It is this energy (E_t) that is mainly responsible for variations in film structure and properties. Low-energy bombardments (typically < 30eV) generally result in a columnar (*i.e.*, grain height > width) microstructure with significant void content. Intermediate levels of bombardment (30eV – a few 100 eV) serve to enhance atomic mobility and help densify the

film. High bombardment energies (several 100 to thousands of eV) commonly result in the reduction or elimination of columnar structure in favor of an equiaxed (*i.e.*, grain height ~ width) structure resembling an initially columnar film that has undergone plastic deformation. Moderate to high energy bombardments also induce a series of collisions that are particularly important for the development of film stress as will be discussed in more detail below. Considering the relative contributions of sputtered and reflected atoms to the total energy, the sputtered atoms arrive at the substrate with energies on the order of 5eV – 50eV. This energy typically scales with the atomic mass of the particle [20, 22]. These energy levels are low compared to the energy of reflected neutrals. The reflected neutral energy is highly variable depending on sputtering process conditions and can be up to an order of magnitude larger than the sputtered atom energy.

Adjustment of the bombardment energy level is easily achieved in ion beam and ion assisted sputtering of films, where the incident particle energy is a directly controllable quantity. In more traditional diode plasma systems such as those used in this work, the bombardment energy is controlled by the alteration of process parameters such as sputtering gasses, compositions and working pressure, as well as process geometries, such as working distance and angle of incidence. Altering the sputtering gas for a particular material alters the ratio of the atomic masses of the gas (M_1) and the target (M_2). It has been shown that the flux of high-energy reflected neutralized gas atoms increases as the square of the target/gas mass ratio, $(M_2/M_1)^2$ [20]. Thus, increases in M_2/M_1 typically result in higher total bombardment energy. Similarly, in mixed gas environments, such as that in reactive sputtering, changing the gas composition also changes the M_1/M_2 ratio, depending on the particular gasses used. Working pressure influences the bombarding energy due to associated variations in the mean free path

length of the gaseous atoms. Decreased pressure leads to increased mean free path length, resulting in fewer collisions in traveling between the anode and cathode. As a result, particles arrive at the substrate with higher levels of kinetic energy.

Finally, it has been shown that geometric and configurational considerations also influence bombardment energy. The working distance between the anode and the cathode influences bombardment energetics similar to working pressure. Because the working distance is typically many times the mean free path of the sputtering gas, increases in working distance increase the probability of collisions, resulting in lower bombardment energy. Additionally, reducing the orientation angle of the target to the substrate will also result in lower imparted energy by the change in the velocity component normal to the substrate for the sputtered and reflected atoms [20].

2.2 Overview of Residual Stress Development in Sputtered Thin Films

Residual stress in a deposited film is commonly thought to arise due to a mismatch strain between the film and its underlying substrate [23]. This stress/strain is typically thought of as being composed of two components: intrinsic and extrinsic. Intrinsic components are those stresses typically associated with the growth process of the film during deposition. Extrinsic stresses are a result of external influences after deposition, such as a temperature change in the presence of mismatched thermal expansion coefficients, and the application/removal of applied loads to the substrate/film system. The most common mechanistic understandings of the development of intrinsic stresses in sputter deposited films are reviewed in the following section. Several reviews have been drawn upon for the review herein, most notably are those by Windischman [20], Hoffman [24], Doerner and Nix [25], and Freund and Suresh [23].

2.2.1 Tensile Intrinsic Stress Mechanisms

Intrinsic stress development mechanisms can be loosely divided into those that describe the development of tensile stress and those that describe the development of compressive stress. The most commonly accepted tensile stress mechanisms are those involving the development and evolution of grain structure, originally proposed by Hoffman [26] and Doljack and Hoffman [27] and more recently modified by Doerner and Nix [25], Nix and Clemens [28] and Freund and Chason [29]. The model for this mechanism considers film growth in the Volmer-Webber mode whereby vaporized atoms condense on a substrate surface to form adatoms that grow to clusters which then meet to form grains and grain boundaries. This process is depicted in Figure 2-4. It is believed that in the formation of grains, the film minimizes its free energy by reducing surface energy in favor of lower grain boundary interface energy. This energy minimization drives the formation, or "zipping up", of grain boundaries that is counterbalanced by elastic deformation of the grains, which are assumed to be firmly adhered to the substrate. In the initial stages of grain formation, this elastic deformation process results in a sharp rise in tensile stress.

The mismatch strain generated in this process is the ratio of the gap closure length (δ_{gap}) to the grain size (d_{gr}) at coalescence (*i.e.*, when clusters meet) [20]. Therefore, for a given grain/film biaxial modulus ($E_f/(1-\nu_f)$) the stress (σ) generated in this process can be estimated by [23]:

$$\sigma = \frac{E_f}{1-\nu_f}\frac{\delta_{gap}}{d_{gr}} \qquad (2\text{-}3)$$

Freund and Chason have developed a model of this process based on the coalescence of cylindrical islands [29]. This model results in an expression for the average film stress:

$$\sigma_{avg} = 0.44 \frac{E^{1/3} \gamma^{2/3}}{R^{2/3}} \quad (2\text{-}4)$$

where γ is the difference between the surface energy and one half the grain boundary energy (γ_s – ½ γ_{gb})[iv], E is the elastic modulus of the material and R is the radius of cylinders (*i.e.*, the grain size at coalescence, $d_{gr}/2$). For representative values of E = 150GPa, γ = 1 J/m^2 and grain size at coalescence R = 10nm – 100nm, tensile stresses of 100-500MPa develop. These predictions are generally consistent with stress magnitudes observed experimentally [23, 30, 31].

A related model considers grain growth after coalescence. If significant grain growth continues beyond coalescence, the model presented by Chaudhari predicts an increase in tensile stress [32]. Similar to the grain coalescence mechanism presented above, this model predicts tensile stress development due to the minimization of free energy. However, rather than reduction in surface energy in favor of a lower combination of grain boundary and elastic strain energy, it is the reduction of only grain boundary interface energy in favor of relatively lower elastic strain energy which drives grain growth and the development of tensile stress.

More commonly observed over longer depositions and thickening films, is the onset of relaxation mechanisms reducing the overall level of stress [31, 33, 34]. The most prevalent relaxation mechanism is surface diffusion and diffusion into the grain boundaries. These diffusion mechanisms serve to relax the lattice distortions associated with the residual stress/strain in the film. This mechanism is typically most prevalent in high mobility materials and may motivate a tensile to compressive stress transition when combined with compressive stress generation mechanisms discussed below [33, 35]. It is important to note that as a

[iv] The factor of ½ is used because the eliminated surfaces share energy of the newly formed interface between two grains.

diffusion-based process, this mechanism is highly temperature dependent. The influence of temperature on both compressive and tensile stress mechanisms is considered separately below. Additionally, it should be noted that this discussion does not consider deformation mechanisms typically associated with plastic deformation, such as yielding and the creation and motion of dislocations.

A final related tensile stress generation mechanism is due to the closure of microscopic voids. Such voids commonly occur as deposition rates exceed the timescales over which surface atoms can rearrange themselves to achieve a fully dense film [25]. The closing of such voids after their formation is achieved by diffusion processes driven by the concept of free-energy minimization described above. In sputtered films, this activity is thought to be further enhanced with moderate bombardment energies promoting film densification.

2.2.2 Compressive Intrinsic Stress Mechanisms

There are three prevalent mechanisms believed to be important in the development of compressive residual stress in sputter deposited films: surface stresses, stresses due to impurities, and stresses induced by cascading collisions of bombarding species (*i.e.*, "atomic peening").

It has been hypothesized that films develop compressive average intrinsic stress due to the combination of stress present at the free surface of the film and stress at the film-substrate interface [36]. At the free surface, the presence of fewer atomic bonds gives surface layers a larger equilibrium spacing. However, the surface atoms are constrained against reaching that spacing by the underlying layers, thus resulting in a compressive mismatch strain at the free surface. At the interface of the film and substrate, compressive surface stresses likely arise in the early stages of growth. Prior to coalescence, it is believed that islands grow unconstrained to the substrate until a critical island/film thickness is reached (thought to be on the order of 1nm) [36].

At this point, the island is thought to be fully adhered to the substrate and continued growth prior to coalescence results in atoms at the free surface of the island to be constrained against expansion to a larger equilibrium bulk atomic spacing. The combination of these free and interface surface stresses are thought to result in the compressive stresses routinely observed in films prior to coalescence [30, 31, 33, 35]. It is estimated that the contribution of these surface stresses can be on the order of -2GPa [36]. Upon coalescence, grain evolution mechanisms of tensile stress described in the previous section may dominate over this stress level. However, as described above, relaxation mechanisms during continued growth may lead to reduced tensile stress and possibly a transition to overall compressive stress. It has been proposed that this transition is due to the domination of surface stresses with decreasing contribution of tensile stress mechanisms [33, 35, 36].

Compressive stress due to film impurities generally results from distortions of the crystal lattice. This may be realized through the inclusion of different size atoms in the lattice or at grain boundaries. These inclusions may be brought about by impurities already present in the sputtering chamber or by reactions due to the chemical nature of the sputtered material and gas environment. Of particular importance to the work presented here is the occurrence of oxidation at grain boundaries, which may produce phases of different stoichiometry and molar volume than the overall film, potentially inducing a compressive stress [20].

A variation of impurity-driven compressive stress is the incorporation of sputtering gasses into the film. It has been shown that the sputtering gas can be incorporated in the deposited film during deposition [20, 24, 37, 38]. Conceivably, such gaseous implantation does generate a level of compressive stress as described above for impurities. In other film growth processes, such as chemical vapor deposition (CVD), stresses due to gas incorporation have been

found to be very significant [39]. However, for sputtered films, the relative importance of these stresses has been a source of debate. In some cases, decreasing working pressure has been shown to correlate with increasing gas content as well as stress, leading researchers to conclude that the role of gas implantation is significant [20, 40, 41]. However, Thornton has demonstrated little stress variation with up to 20X changes in entrapped gas content. Such results have led to the view that the implantation of sputtering gasses has minimal effect on the stress level for sputtered films [42].

In light of the data presented by Thornton [42], it has been proposed that compressive stress arises due to interstitial implantation of sputtered film atoms originating at the surface of the deposited film. This development of compressive stress is a result of collisions between bombarding species and the developing film and is typically described by the collisional cascade theory proposed by Sigmund [43]. The details of this theory are beyond the scope of the work presented here. However, the important characteristic of this theory, captured schematically in Figure 2-5, is that bombardment of a surface with energetic particles results in a series of collisions at and below the surface. At the cathode/target in a sputtering system, incident energies must be high enough to eject target atoms onto the anode/substrate. At the anode/substrate, the energies of the sputtered and reflected gas atoms are sufficiently large to cause distortion of the lattice of the growing film. This distortion is thought to be due to the driving of surface atoms into interstitial sites in the lattice, resulting in compressive stress. However, it is important to realize that some of the literature continues to cite gas implantation as a major source of compressive stress when correlations between gas content and stress are made. Therefore, the process of particle bombardment during sputtering resulting in lattice

distortion and/or implanted gas mechanisms is very generally referred to as "forward sputtering" or "atomic peening."

A model of stress development by atomic peening proposed by Windischmann suggests that stress (σ) is related to ion flux (ϕ), total particle bombardment energy (E_t) and film material properties such as biaxial modulus ($E/(1-\nu)$), molar mass (M) and density (ρ) by [44]:

$$\sigma = k\phi\sqrt{E_t}\,\frac{E}{(1-\nu)}\,\frac{M}{\rho} \qquad (2\text{-}5)$$

The square-root dependence on energy has been substantiated by experimental results [45, 46] and has been used to reinforce the hypothesis that the forward-sputtering mechanism is a momentum-driven process [20]. However, it is important to realize that these experiments typically used a controllable ion source rather than traditional diode sputtering due to the fact that accurately quantifying the bombardment energy of a plasma diode sputtering system is difficult.

The development of compressive residual stress via the forward sputtering mechanism is the most common explanation of observed trends in stress with processing parameters. At low/moderate energy process conditions (such as low substrate bias, high working pressure and low target/mass ratio) stress levels are typically tensile or only slightly compressive. Increased bombardment conditions, while possibly initiating an initial increase in tensile stress due to film densification and void closure as described above, ultimately results in forward sputtering and the compressive stress typically observed in sputtered films. Further increase in bombardment energy may result in a plateau in stress accompanied by the suppression of columnar microstructure in favor of an equiaxed structure, indicative of plastic deformation.

2.2.3 Intrinsic Stress Due to Phase Changes and Precipitation

Intrinsic stress in a film may also arise as a result of phase changes in the film constituients after the film has adhered to the underlying substrate. The exact nature of the stress development depends upon the type and degree of phase change. Changes in crystallographic structure may result in tensile or compressive stress depending on the associated increases or decreases in volume. Similarly, amorphous to crystalline phase changes can result in density changes of 1-2% [25], also leading to compressive or tensile stresses. Precipitation of new phases of material at interstitial sites or grain boundaries may also result in compressive stresses in a similar manner to impurities as described in section 2.2.2.

2.2.4 Influence of Temperature on Intrinsic Stress Development

The discussion of intrinsic stress development above has been limited to deposition carried out at room temperature. However, depositing at high temperature has significant effects on the development of stress and structure in sputter deposited films. Generally, elevated temperatures serve to relax stresses in sputtered films, regardless if they are tensile or compressive, via the enhancement of diffusion mechanisms described above. Likewise, compressive stresses may be relaxed by a combination of enhanced mobility that minimizes the lattice distortion associated with the atomic peening process or by the release of implanted gasses prior to film cooling [20]. However, high temperature depositions may also promote different or additional phases and crystallinity. As described above, these new phases may introduce an additional level of tensile or compressive stress that results in a net increase in the magnitude of stress. Similarly, post-deposition anneals may give rise to the same stress relaxation mechanisms as high temperature deposition. However, annealing in oxidizing or reducing environments may promote chemical reactions that alter film structure, and therefore stress.

2.3 Overview of the YSZ Materials System

2.3.1 General Characteristics of YSZ

Zirconia and zirconia alloys are typically known for low thermal conductivities, high strength, toughness, hardness and ionic conductivity as well as good optical properties, such as high refractive index, low absorption and weak losses in the near-UV to mid-IR range [47, 48]. Uses of zirconia include thermal barrier coatings (TBC) and optical components, as well as a material for oxygen sensors and solid oxide fuel cell electrolytes. Pure zirconia (ZrO_2) has a crystal structure that varies with temperature and pressure. In its bulk form, pure ZrO_2 is typically stable in a monoclinic structure from room temperature up to 1170°C, tetragonal from 1170°C – 2370°C and cubic (fluorite, face centered cubic - fcc) at temperatures greater than 2370°C [48-50]. These structures are shown in Figure 2-6. Changes in crystal structure from one phase to another result in a volume change of the lattice. In application, this volumetric strain of a constrained material gives rise to stress. This is particularly common in applications such as oxygen sensors and solid oxide fuel cells, where the activation energy for adequate ionic conductivity requires operation temperatures at or near the monoclinic to tetragonal transition regime of 1170°C. The associated volume/stress change contributes to cracking and structural failure of devices.

In order to alleviate this phase instability problem and improve ionic conductivity through the introduction of increased oxygen vacancies, pure zirconia is typically doped with a second oxide, such as CaO, MgO, Al_2O_3 or Y_2O_3 [50]. The dopant is introduced as a solid solution that acts to stabilize the Zirconia to a particular crystal structure from room temperature to operation temperature. In bulk processed materials, the stable crystal structure at room temperature depends on the fraction of stabilizer. For solid oxide fuel cell (SOFC) applications,

the most common dopant used, and the primary material examined in this thesis, is yttria. In yttria stabilized zirconia (YSZ), a stable tetragonal phase is formed with 2 – 8 mol% yttria, giving what is commonly referred to as partially-stabilized zirconia [51]. Fractions of yttria greater than 10% generate a stable cubic structure at room temperature, typically referred to as fully stabilized zirconia. The stable structure combined with typically high vacancy content make cubic YSZ generally more desirable for electrochemical applications at the bulk material length scale. Intermediate fractions of yttria dopant produce mixed monoclinic/tetragonal and tetragonal/cubic phase materials.

For macroscale applications, YSZ is most commonly produced via powder processing, tape casting, screen printing or plasma spray techniques that give typical electrolyte layer thicknesses on the order of 10 – 200 μm [50]. However, as discussed in Chapter 1, there exist electrochemical and structural motivations for decreasing the thickness of YSZ when used as a SOFC electrolyte material. Several techniques are available for deposition of YSZ electrolyte layers with the objective of reduced film thickness for enhanced electrolyte performance. These techniques are well-reviewed by Wil *et. al.* [52] and rely on a variety of chemical and/or physical processes. They include chemical vapor deposition (CVD), sol-gel deposition, modified plasma spray techniques and physical vapor deposition (evaporation, pulsed laser deposition and sputtering).

Sputter deposition is particularly attractive for creating films on the order of 1 μm thick (giving nanostructured grains) as it is commonly used for such film thicknesses. YSZ films of larger thicknesses (*i.e.* several microns thick) deposited via sputtering are typically less prone to cracking and have low void and defect densities relative to sol-gel deposition, spray pyrolysis

and tape casting [52]. However, it is important to note that little work has been done on sputtered YSZ in the sub-micron thickness range.

2.3.2 Structure and Phase Characterization of Sputtered YSZ

The primary focus of much of the work done to date on sputter-deposited zirconia/YSZ films has been the examination of crystallographic phase under varying film compositions, sputtering conditions and post deposition treatments. Furthermore, although there has been work on sputter deposition of pure zirconia that has demonstrated the ability of sputtering to produce tetragonally stabilized pure zirconia films [49], the vast majority of prior work has focused on doped zirconia films.

Work done to date on sputtered YSZ shows significant differences in phase and structure than YSZ prepared with macroscale / bulk processing techniques. Film growth structure in sputtered YSZ has been observed to generally be columnar with equiaxed structures forming under conditions of high energetic bombardment such as large applied substrate bias [53, 54]. These films are generally thought to be fully crystalline. However, citations to other work as well as observations made by Ji *et al.* have suggested the likely presence of amorphous phases [47].

Crystalline sputtered YSZ films have been shown to be monoclinic [47], tetragonal [51], cubic [53, 55, 56] and mixed phases [57, 58] in their as-deposited state. The structure of these films is typically determined using X-ray diffraction (XRD) techniques, although e-beam diffraction and Raman spectroscopy are also used. Film thicknesses used in the studies cited ranged from 0.1 – 5 microns [53, 58], making these results of particular interest for μSOFC applications.

One observed correlation with crystal structure is yttria content. Yttria contents ranging from 2 – 3 mol% show a monoclinic or mixed monoclinic and tetragonal structure [47, 57, 58]. Pure tetragonal structures have been observed in Yttria contents as high as 10 mol% [59]. However, fully cubic structures have also been observed at this composition level [55] as well as for yttria content as low as 4.5 mol% [47, 51]. The combination of these results indicate that the crystal structure of sputtered YSZ films as a function of stabilizer content can vary significantly from the bulk.

Where post-deposition annealing (in the range of 500°C and 1200°C) has been performed, the development of mixed phase films as well as complete phase changes have been observed [47, 57]. Similar variations in the crystallographic texture of the as-deposited films are observed, where both (111) and (200) textures have been observed for all three phases [51, 54]. Again, post-deposition annealing has resulted in texture evolution where existing textures are intensified and/or additional textures develop [47, 59, 60]. In these studies, however, no quantitative characterization of grain size or grain evolution with annealing is presented.

2.3.3 Residual Stress in Sputtered YSZ

Compared to the work done on the structure of sputtered YSZ films, there is less previous work examining the residual stress of sputtered YSZ films. However, the work done has seen a wide range of resulting stress levels, where film stresses have ranged from approximately 2 GPa compressive [61] to approximately 2 GPa tensile, as well as intermediate compressive and tensile values on the order of a few hundred MPa [13]. In these studies, stress is typically determined by substrate curvature methods [13, 61, 62], the details of which are discussed in a later section.

Variations of residual stress of sputtered YSZ have been correlated to crystal structure. Gao *et al.* have observed variations in residual stress with yttria content and resulting film

structure, where films composed of greater than 8mol% yttria and cubic structure have significantly less compressive stress (~0.3 - 0.5 GPa compressive) than those with less than 8mol% yttria and tetragonal structure (~2 - 3 GPa compressive) [51]. Lee and Park have made a related observation of increased compressive stress with tetragonal structure [62].

Stress variations have also been correlated with bombardment energy. Knoll and Bradley observed the stress in RF sputtered YSZ films to have direct correlation with substrate bias, as films deposited under no bias have nearly zero intrinsic residual stress and those under high substrate bias (-200V) have up to ~ 2GPa compressive stress [53]. These results are consistent with standard correlations of compressive film stress with deposition energetics/bombardment due to peening stresses as discussed in section 2.2.2.

Finally, work done specifically in the way of μSOFC development by Baertsch *et al.* revealed a thickness dependence on the residual stress of RF sputtered YSZ [13]. A similar dependence was observed by Carniero *et al.* [61]. Additionally, the annealing of buckled, released YSZ membranes by Baertsch *et al.* revealed a flattening or smoothing of the buckled shape indicative of compressive stress relaxation. Several of the hypotheses put forth for these observed behaviors are tested in the work presented here.

2.4 Implications of Residual Stress for Microfabricated Structures

The presence of residual stress can have a profound impact on the operation of devices utilizing microfabricated structures such as released beams and membranes. Microfabricated resonant structures such as those utilized in accelerometers and gyroscopes will have their resonant frequency altered by the presence of residual stress. Similarly, development of microfabricated optoelectronic devices are severely impacted by the presence of residual stresses and strains. Such devices often require positional control of released structures to less than the

wavelength of light; this requirement can be limited by stress-induced out-of-plane deformations [63]. As a result, designs must take such phenomena into account and fabrication processes must seek to control and characterize residual stress within specified limits. Structural failure (*i.e.*, cracking, fracture, buckling) is also a concern in released structures with sufficiently high residual stress. In applications requiring significant temperature excursions of layered materials with mismatched thermal expansion coefficients, the combination of intrinsic stress and extrinsic thermal stresses may impose constraints on allowable geometries and operating conditions. Srikar *et al.* have considered the impact of residual stresses on thermostructural design of membranes for μSOFC applications [64]. In that work, the failure of microfabricated membranes is modeled considering a combination of residual stress and temperature change leading to either linear elastic buckling or fracture. The combination of these two failure modes gives rise to a design space that can be visualized on a plot of residual stress and temperature change as presented in Figure 2-7. With this design-space, for a particular structure, one can establish the allowable residual stress and temperature excursions for a released membrane of particular size and known mechanical properties.

More recently, it has been recognized that linear elastic buckling of released membranes may be an overly conservative failure criteria for their application to μSOFC's. That is, membranes operating in a post-buckled regime may withstand larger intrinsic stresses and/or temperature excursions than those predicted by a linear elastic buckling failure criteria. Geometrically non-linear, post-buckling analyses used to consider similar problems have been developed by Ziebart et al. [65] and are currently being built upon for the thermomechanical analysis of multilayered μSOFC membranes by others [66]. Application of failure criteria using such analyses typically results in a significant expansion of the allowable design space.

2.5 Review of Residual Stress Measurement Techniques

Several experimental techniques exist for determining the residual stress state of deposited films. These techniques rely on a variety of measured physical quantities related to the overall (*i.e.,* intrinsic and extrinsic) stress state of a film. A review of the common techniques is provided by Srikar and Spearing [67]. The techniques reviewed include the utilization of various microfabricated structures to infer residual stress states typically based on measured deflections and other responses such as changes in natural frequency. However, the work presented in this thesis focuses on residual stress determination via substrate curvature techniques. The important aspects of this technique is presented below.

2.5.1 Residual Stress Measurement by Substrate Curvature Techniques

One of the most widely used class of residual stress measurement techniques are those based on measuring changes in substrate curvature due to a residually-stressed deposited film. The origination of these techniques is attributed to Stoney [68]. Considering a thin, stressed film deposited on a thick, initially stress-free substrate, the stress in the film (σ_{res}) is related to the change in curvature ($\Delta\kappa$) by (known as the Stoney formula):

$$\sigma_{res} = \frac{E_s}{1-\nu_s}\frac{\Delta\kappa}{6}\frac{h_s^2}{h_f} \qquad (2\text{-}6)$$

where h_s, h_f, and $E_s / (1-\nu_s)$ are the substrate thickness, film thickness and substrate biaxial modulus, respectively. For axisymmetric, small deformations, the curvature (κ) of a plate along a particular coordinate axis (x) in the plane of the plate may be related to its out of plane deflection profile (w) by:

$$\kappa = -\frac{d^2 w}{dx^2} \qquad (2\text{-}7)$$

Integrating twice gives the relationship between the curvature and the leading term (a_2) of a parabolic fit to the deflection profile to be:

$$\kappa = -2a_2 \tag{2-8}$$

Proper application of the Stoney equation requires important assumptions to be met. These include assumptions of axisymmetric (*i.e.*, spherical) bending, small deflections, uniform films which are thin compared to substrate thicknesses ($h_f << h_s$) and small relative stiffness of the film compared to the substrate ($E_f h_f /(1-\nu_f) << E_s h_s/(1-\nu_s)$). Additionally, it is assumed that the mechanical properties of the film and substrate are in-plane isotropic. Deviations from these assumptions and their effect on curvature measurements have been considered by several authors [23, 69-74]. Finot *et al.* introduced a parameter (A) to help evaluate the effect of deviations from these assumptions associated with the presence of geometric non-linear substrate deformation that would make the application of the Stoney equation invalid:

$$A = \sigma_{res} \frac{D_s^2 h_f}{h_s^3} \tag{2-9}$$

where D_s is the substrate diameter. They have shown that, for substrate diameter to film thickness ratios $D/h_f > 50$, the Stoney equation correlates to fully non-linear finite element analysis predictions to within less than 5% provided the following criteria is met:

$$\frac{A}{A_c} < 0.1 \tag{2-10}$$

where A_c is a critical value that, under the same assumptions, depends only on the mechanical properties of the substrate used. For silicon substrates, A_c = 680GPa.

Curvature measurements used in the determination of thin-film residual stress on substrates are done in several ways. The most common technique involves extracting changes in curvature ($\Delta\kappa$) using eq. (2-8) and measured deflection profiles taken by single line scans across a wafer before and after film deposition and calculating the stress using Stoney's formula. Line scans can be taken by a capacitance probe scanned across a wafer, a stylus in physical contact dragged across the wafer, or a laser reflection system, as shown schematically in Figure 2-8 [23]. Two-dimensional wafer deflection profiles have also been taken using a full-field interferometric technique termed the coherent gradient sensor method (CGS) originally developed by Rosakis *et al.* [75]. This technique is particularly useful when all three curvature components are needed.

An important final note on substrate curvature techniques is their application to in-situ monitoring of residual stress during film growth. Such work has been done using films deposited on suspended beams whose deflection is monitored using capacitive measurements [30]. In these measurements, deflections due to thermal bilayer bending are minimized by the use of radiation shields to achieve thermal isolation. A related technique based on monitoring the end deflection of a cantilever substrate during deposition using a reflected laser has also been developed [33]. As with stress measurement techniques using plate structures as substrates, deflection profiles of the beams in these systems are used to calculate changes in curvature. These changes in curvature are related to stress by Stoney's equation (2-6) with the minor change that only Young's modulus (E_s), rather than the biaxial modulus ($E_s/(1-\nu_s)$), is the leading factor. Finally, Carniero *et al.* have developed an in-situ stress measurement system using strain-gage rosettes mounted to the back side of wafers to monitor the strain and curvature of the wafer during film deposition [61].

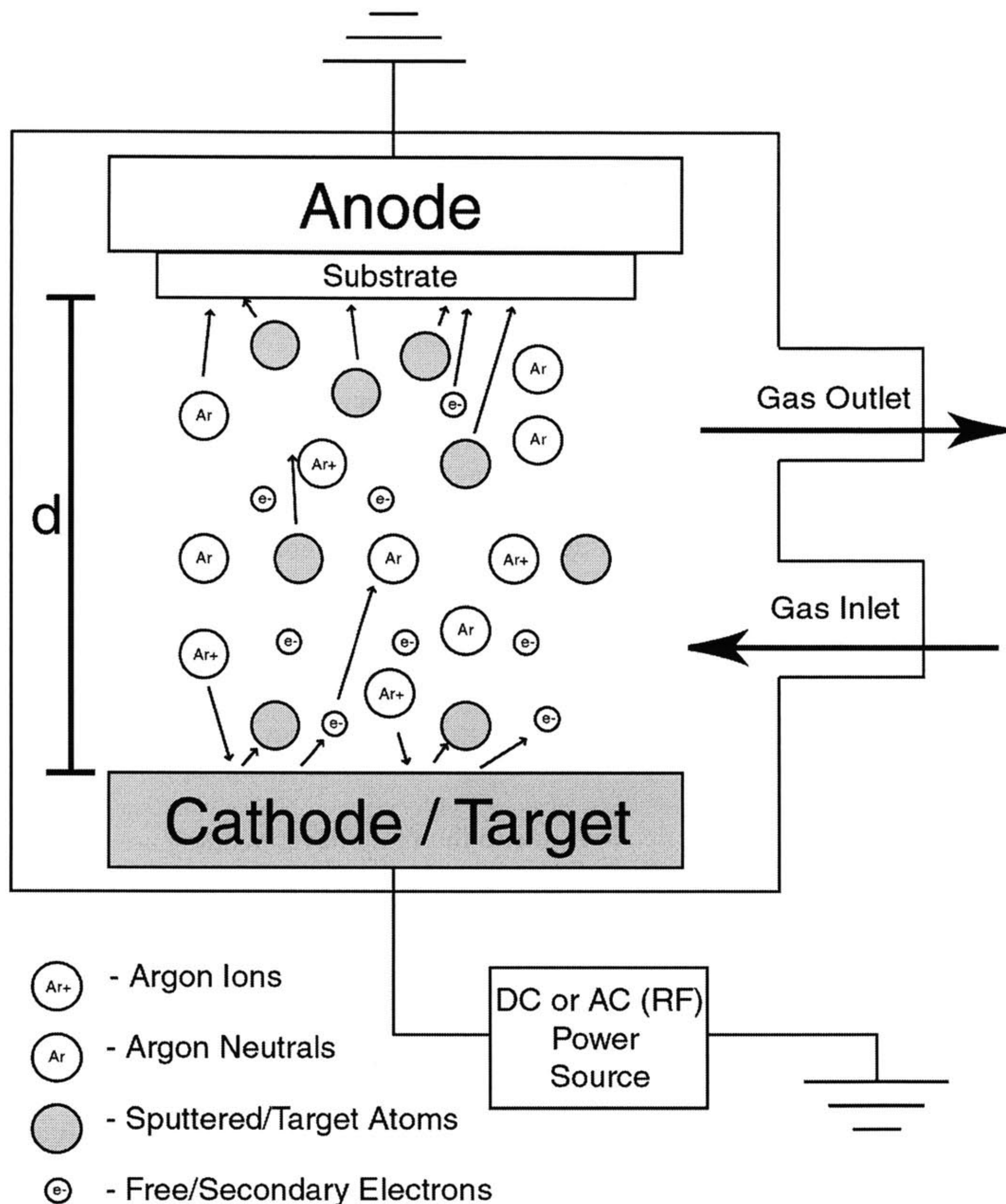

Figure 2-1: Schematic view of typical diode sputtering process. The interactions occurring between the anode and cathode, separated by a working distance d, illustrate incident sputtering atoms, ejected target material and secondary electrons in addition to the presence of sputter gas neutrals.

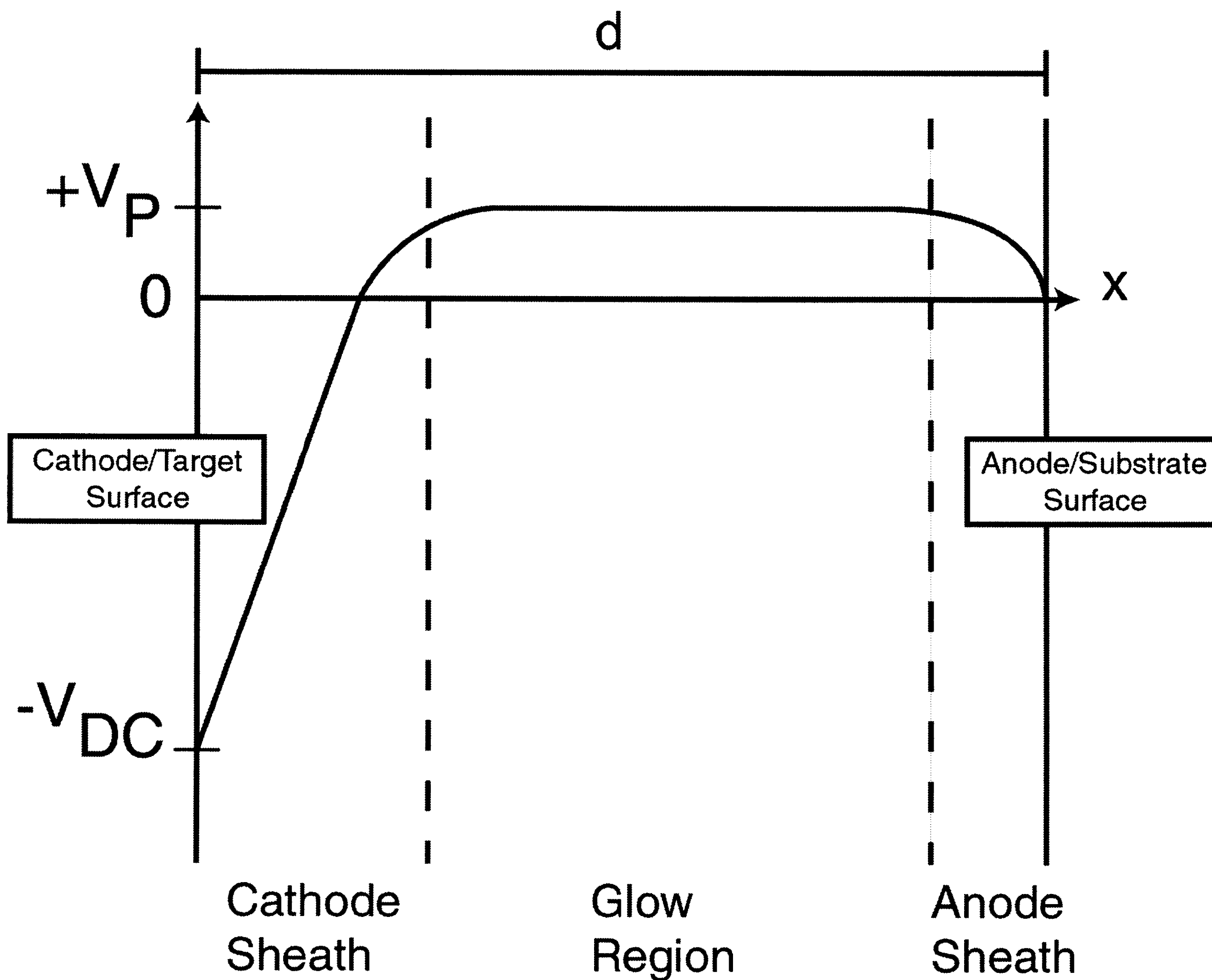

Figure 2-2: Characteristic regions of plasma during sputtering (adapted from [15]). Note that V_{DC} represents the applied voltage in DC sputtering and the DC bias component of the applied voltage in RF sputtering.

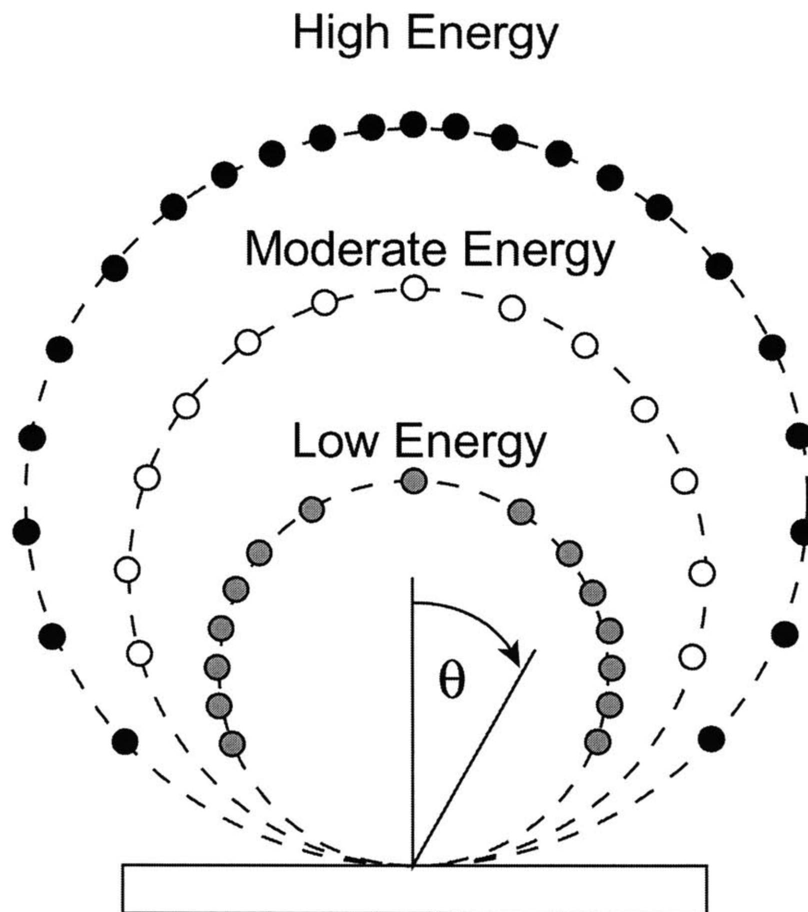

Figure 2-3: Emission profiles for varying sputtering energy (adapted from [16]). Marker density is proportional to concentration of material, indicating more material deposited at higher and lower angles from the normal for low and high energy bombardments, respectively.

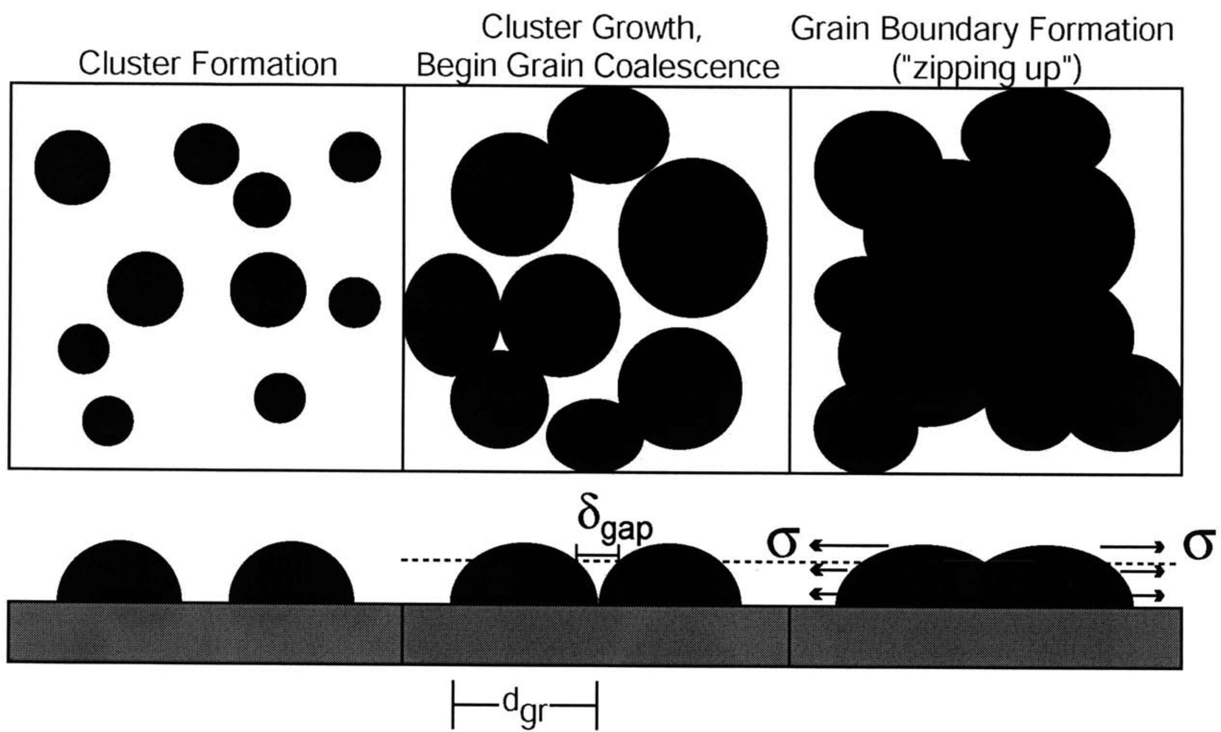

Figure 2-4: Development of tensile stress during grain coalescence (adapted from [31]).

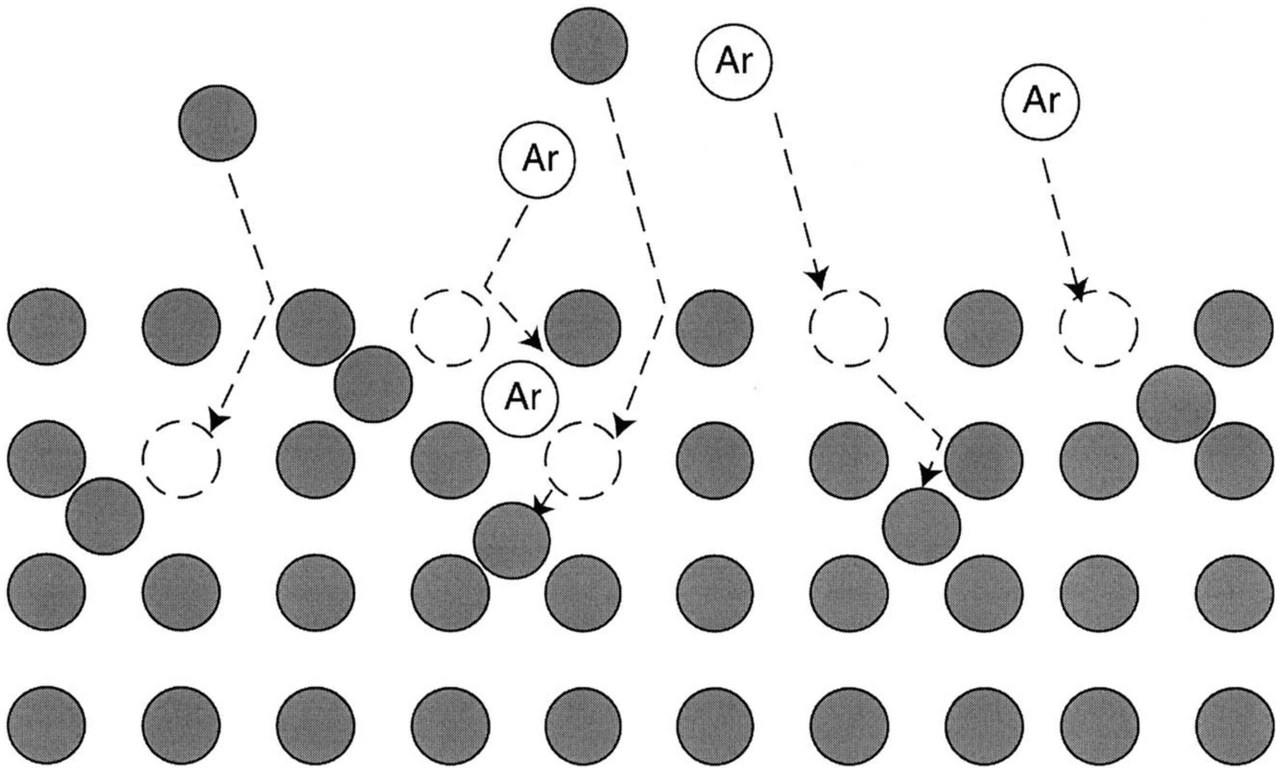

Figure 2-5: Illustration of the atomic peening process. Interstitials arise from implanted gases and/or the collisions of reflected neutrals (here Ar) and sputtered atoms with film surface atoms.

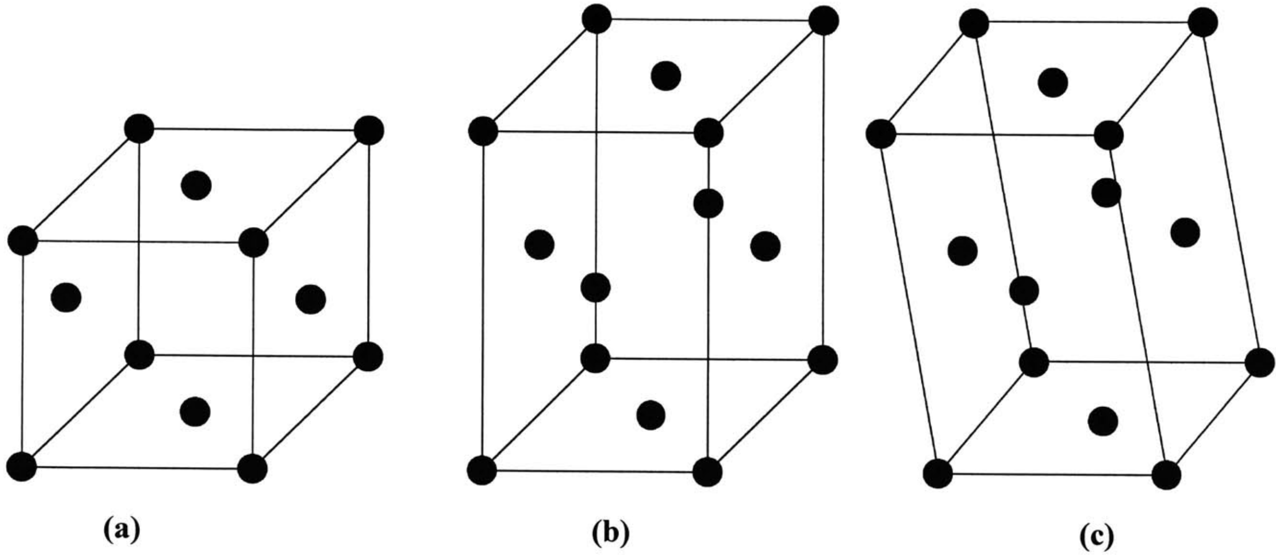

Figure 2-6: Crystal structures of zirconia: (a) cubic (FCC), (b) tetragonal, (c) monoclinic. Lattice sites are occupied by the cation (Zr,Y).

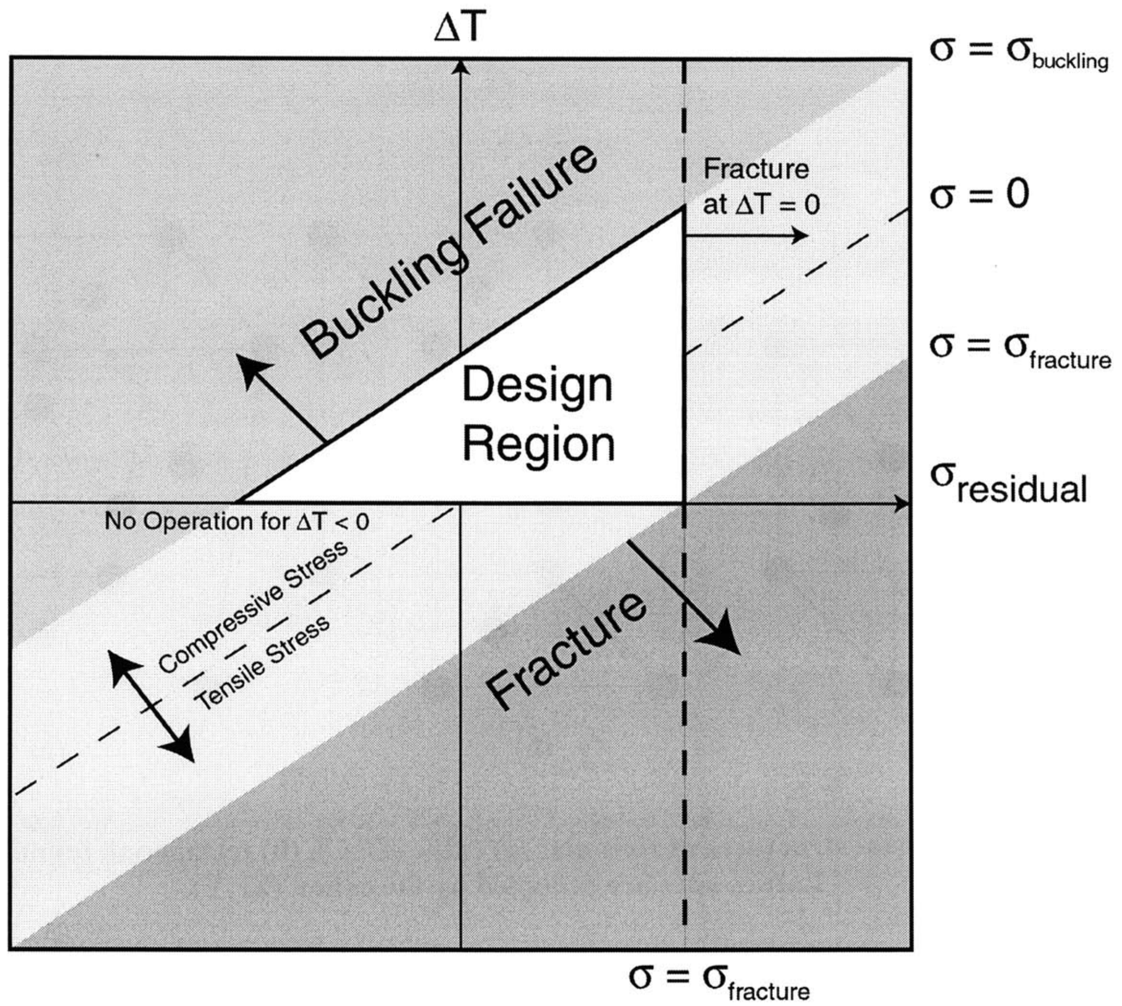

Figure 2-7: Representative design space for μSOFC membranes considering the failure modes of linear-elastic buckling and fracture (adapted from [64]).

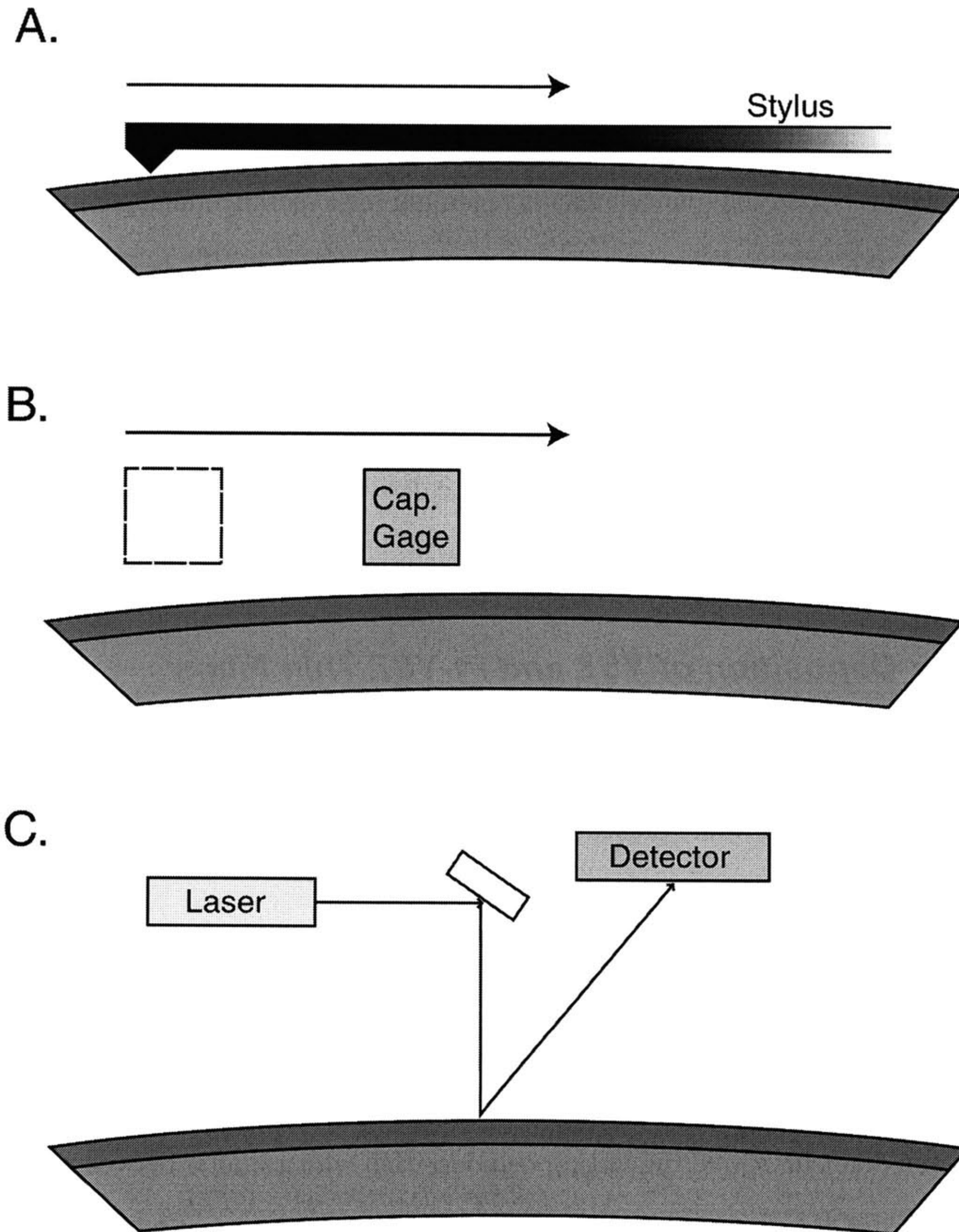

Figure 2-8: Line scan techniques for wafer curvature measurement: (A) scanning stylus, (B) capacitance probe, and (C) scanning laser system (adapted from [23]).

Chapter 3: Experimental Procedures

This chapter covers the relevant details regarding the experimental apparatus and procedures use in this thesis. The apparatus, procedure and characterization of the sputtering processes used are first presented, followed by a discussion of the techniques employed in determining the residual stress of deposited films, including a discussion of the range of validity of these techniques and estimated uncertainties in the derived residual stress states. Finally, an overview of the apparatus and methods used in the materials characterization work is presented.

3.1 Sputter Deposition of YSZ and Pt-YSZ Thin Films

The apparatus, procedures and process characteristics involved in the deposition of YSZ and co-sputtered Pt-YSZ films are presented in this section.

3.1.1 Sputtering Apparatus and Procedure

The sputtering system used is a diode, plasma, planar magnetron system designed by Kurtis J. Lesker, Inc. The system is shown schematically in Figure 3-1. This system is equipped with three 50mm diameter sputtering target positions, each with a shutter between the target and substrate. Magnets are located underneath a copper mounting plate for each target. Each position is water-cooled and uses a grounded cover shield and may use either a DC or RF Power source. Targets are inclined at 30 degrees from the vertical and have a working distance from the substrate/sample of approximately 9 cm. Unless stated otherwise, the samples in this work were 100mm diameter prime grade, single sided polished, (100) Si wafers (typical thickness ~530μm). Samples/substrates are cleaned by a sequence of rinses with acetone, methanol, isopropanol and deionized water. Nothing is done to remove the native oxide layer of the Si

wafers. After cleaning, the samples are put into an appropriate holder which is then inverted and mounted to the sample stage. The substrate/sample is rotated during deposition (~0.25-0.5 rev/s) and also may be heated up to 600 °C by a halogen heat lamp controlled by a thermocouple mounted near the sample.

In a typical sputtering process, after the target and sample have been loaded, the system is pumped down to a pressure of 0.8 Torr with a mechanical pump, followed by a high vacuum pump down to the desired base pressure using a Cryo-Pump. High vacuum pressure levels are monitored using an ionization gage capable of measuring pressures down to 0.1×10^{-7} Torr. The ionization gage is degasified with a heating filament prior to every reading. In this work, base pressures < 1×10^{-6} Torr are used, typically requiring pump down times of 10 hours or greater. Once the desired base pressure is achieved, the substrate temperature is set by a programmable controller with a resolution of 1°C. When the substrate temperature is reached, the required sputtering gases are introduced into the chamber. The sputtering gas pressure (*i.e.*, "working pressure") and gas ratios are controlled by a capacitance gage and an MKS multi-gas MASSFLO 647C controller capable of controlling four gases simultaneously.

A plasma is ignited with the application of a DC or AC voltage controlled by adjustable DC or RF Power sources. Details on the physical process involved are provided in Chapter 2. This system is not equipped with a separate substrate bias voltage control. Typically the plasma is ignited at a low power (*i.e.*, ~20W for RF sputtering) and gradually increased at ~3-5 W/s to avoid the possibility of target cracking due to thermal shock. The target is then "cleaned" by pre-deposition sputtering with the shutter closed for a period of time based on the previous use of the target, typically ranging from 5-30mins. After this sputter-cleaning process, the shutter is opened and deposition proceeds for the desired time period. When the desired film thickness is

reached, as determined by the deposition time and a previously calibrated deposition rate (discussed in section 3.1.2), the shutter is closed and the power is gradually reduced at ~3-5 W/s to extinguish the plasma. The temperature is then lowered to room temperature, sputtering gases are evacuated and, when the system has returned to room temperature (typically at ~5 °C /min), the sputtering chamber is vented to atmospheric pressure and the sample is retrieved. The total time for the entire sequence of processes is largely determined by the pump-down time and deposition time. For a typical base pressure < 1 x 10^{-6} Torr, the pump down time is ~10hrs. Typical depositions (see next section for deposition rate characteristics) are 1-2hrs, giving a total process time of ~12hrs.

3.1.2 YSZ Deposition Conditions, Rates and Uniformity

This work began with a given target composition and a set of "standard" deposition conditions inherited from previous work done within the larger multidisciplinary μSOFC device design initiative. These standard conditions are presented in Table 3-1. The composition of the target, a nominally 50mm diameter x 1cm thick cylindrical target supplied by ACI Alloys, is 91% Zirconium and 9% Yttrium by mass. The majority of the electrochemical characterization of YSZ films done within the μSOFC MURI group had been done on films deposited using this same target and under these conditions. Firmly establishing the evolution of residual stress and microstructure under these standard conditions was an important goal of this thesis. Another important task was the exploration of the effects of variations in deposition conditions away from these standard conditions. An important process characteristic required for both initiatives is the deposition rate under a given set of process conditions. Deposition rates are determined by measuring the film thickness achieved after a known deposition time for a given set of conditions. Films for these measurements are typically deposited on pre-cleaned glass

microscope slides with one area masked off from deposition through use of vacuum tape or a non-volatile hardening paint such as commercial office supply "white-out". After deposition onto these samples, the masking material is removed and the surfaces cleaned by alternating ultrasonic rinses in solvent and deionized water baths. A minimum of two rinses were used. The film thickness is then measured on a Tencor P10 profilometer using a stylus force of 6mg, 20μm/s scan speed, 50Hz sampling rate, and 13μm range setting with a quoted resolution of 7.81 x 10^{-3} Angstroms. Prior to each series of measurements, a Veeco 4500 Angstrom step-height standard is measured to ensure accurate calibration of the machine. A discrepancy of less than ±2% is observed for all calibration measurements. For a given deposition rate sample, an average of a minimum of 5 profilometry measurements is used.

In Figure 3-2, the deposition thickness vs. time characteristics of YSZ under standard conditions are shown. Error bars represent minimum and maximum thickness measurements. Deposition rates are determined by dividing the average thickness measurement by the deposition time. In Figure 3-3, the deposition rate of YSZ as a function of deposition working pressure is presented, all other deposition conditions are standard. Where multiple deposition rate calibrations were performed, each data point represents the average rate and error bars represent the range of measured rates over all samples. Deposition rates are presented for two different target positions. Differences in deposition rates for different targets may be attributed to different magnet strengths (average strengths of 515 milligaus and 415 milligaus for Positions A and B, respectively) [76] . All data presented in this thesis used position B, with the exception of data presenting the variation of film stress with working pressure of room-temperature deposited films, which was done at position A. However, it is important to note that the comparable deposition rates of both target positions make it unlikely that the overall mechanisms

governing film growth and stress development change significantly between the two targets. Fits of these two data sets indicate a linear decrease in deposition rate with increasing working pressure, as expected from the discussion in Chapter 2. Calibrated deposition rates did not change with elevated deposition temperature.

Another important process attribute is the film thickness uniformity across the sample. This was characterized by masking off spots along the radius of a wafer and measuring film thickness via profilometry as described above. Measured uniformity profiles from three depositions are presented in Figure 3-4. Profiles along two radii from one sample, oriented approximately 90 degrees from each other, are also shown. These two radial profiles indicate minor variations (<5%) in uniformity along different radii which may be attributed largely to uncertainties in profilometry measurements. In general, the uniformity profiles indicate film thickening in the radial direction with a maximum thickness variation of approximately +20% with the observed non-uniformity largely confined to the outermost 20mm. From 0 – 40mm radially, the thickness variation is +9%. This is reflective of a low to moderate bombardment energy deposition profile as discussed in Chapter 2. Actions taken to account for the effects of this thickness non-uniformity in curvature/stress measurement are discussed in section 3.2.1.

3.1.3 Conditions and Characterization of Pt-YSZ Deposition

While the primary material examined in this thesis is Yttria-stabilized Zirconia (YSZ), some preliminary work using a co-sputtered Pt-YSZ composite film for use as a novel anode/cathode material is also presented. This material is particularly attractive for μSOFC applications due to its potential for a high triple-phase-boundary length and its ease of integration with YSZ deposition into fabrication processes. The deposition conditions and deposition rates for this material are presented Table 3-2. The final film composition with these deposition

conditions is approximately 50/50 wt%. Deposition of this material was initiated by and continues to be refined by J. Hertz [77]. In the work done to date, it was found that this material required deposition at high temperatures to ensure crystallization of the Pt phase of the film, which is necessary for the film to act as a good electrode/current collector for μSOFC applications.

3.1.4 Characterization of Substrate Heating During Deposition

As discussed in Chapter 2, secondary electrons emitted during the sputtering process typically result in substrate heating. Previous work done by Knoll and Bradley indicate that this heating during a nominally room temperature deposition can be substantial [53]. In that work, substrate temperatures of 250°C and 270°C were measured during unbiased and biased YSZ depositions, respectively. This level of substrate heating is particularly significant for the work presented here when considering its effect on film structure through its influence on the diffusive mobility of films. This, combined with the added thermal stress component due to coefficient of thermal expansion (CTE) mismatch between film and substrate, make the characterization of substrate heating during room temperature depositions important for understanding the development of stress and microstructure in sputtered YSZ films.

Substrate heating during a single room temperature deposition was monitored using a K-type thermocouple bonded to the back side of a 4" Si wafer using a thermally conductive, electrically insulating ceramic paste (Omegabond 300). The thermocouple was fed through a high vacuum instrument feed-through on the top of the sputtering machine to a digital thermocouple read-out. A deposition process representative of an approximately 1 μm thick YSZ film was carried out and temperatures were read at approximately 15 minute intervals. This deposition included a 60 minute pre-sputter/sputter clean time. During this pre-sputter time, as

can be seen in Figure 3-5, secondary electrons reflected from the shutter still serve to heat the substrate over 100°C. Presumably, this is done either through direct reflected collisions and/or conduction through other parts of the chamber and sample stage. During deposition, it can be seen that the temperature rises to and remains relatively constant at about 185-190°C until the shutter is closed and the temperature rapidly falls as the heat is conducted to the outer portions of the substrate chamber. This observed level of heating is comparable to that observed by Knoll and Bradley. Chapter 5 considers the implications of this heating effect on the evolution of stress and microstructure in YSZ films.

3.2 Residual Stress Measurement of Deposited Films

This thesis uses wafer curvature measurement techniques for the determination of residual stress states in YSZ films. Wafer curvature measurement was selected primarily because it is a widely accepted, relatively simple technique requiring simple test specimens (thin films on thick substrates). Furthermore, the curvature measurement apparatus available (described below) was capable of performing residual stress measurements at elevated temperatures up to 500°C, which was believed to be important for the investigation of YSZ as it is typically subjected to high temperatures in operation. Finally, curvature measurement was particularly attractive for this work because, where Stoney's equation is valid, stress measurements through curvature differences do not require knowledge of the film's mechanical properties such as biaxial modulus, which is currently unknown for these films.

As presented in Chapter 2, a primary source of error in the application of Stoney's equation in the evaluation of residual stress in thin films is the presence of non-linear deformations in the film-substrate system. Finot *et. al.* established a simple criteria to ensure that a given film-substrate system remains in the linear deformation regime to allow for the

application of Stoney's equation to within 5% accuracy [69]. Combining equations (2-9) and (2-10), this criteria reduces to:

$$\sigma_{res} \frac{D_s^2 h_f}{h_s^3 A_c} < 0.1 \tag{3-1}$$

Where A_c = 680 GPa for a silicon substrate. In this work, 4-inch (100mm) diameter substrates of approximately 530μm thickness are used, indicating that the criteria for non-linearity reduces to:

$$\sigma_{res} h_f < 3.60 \text{ GPa } \mu\text{m} \tag{3-2}$$

In this work, the maximum residual stress magnitudes and film thicknesses are 1.5 GPa and 1 μm, respectively, indicating that non-linear deformation of the substrate is not expected and Stoney's relation is appropriate for the film/substrate combinations in this work.

3.2.1 Wafer Curvature Measurements

The curvature measurement apparatus used in this work was a Tencor 2320 Wafer Curvature Measurement System. This system, pictured in Figure 3-6, uses a scanning laser system such as that discussed in Chapter 2. An incident laser is reflected off the surface of the substrate and onto an optical detector. The position of the laser spot on the detector is used to determine the out of plane deflection of the wafer. The out-of-plane deflection is determined along a line of the substrate (in the case of a circular wafer, a diameter) to give a deflection profile. For a 100mm diameter substrate, the deflection profile is measured only across the center 80mm portion of the diameter. This is done for two reasons: (1) to avoid free edge effects manifested in the rapid increase in the stress and curvature state as one moves radially inward from the traction-free surface and (2) to minimize the effects of film thickness non-uniformity on the residual stress calculation. As discussed above, within the 80mm measurement region, the thickness typically increases by 10% in the outer-most 10mm of the radius. This results in a total

average thickness that is less than 5% greater than the central, nominally uniform portion of the film. It is believed that the effect of this thickness variation on the net change in curvature of the wafer is relatively small and is captured in the uncertainty estimates in the residual stress measurement discussed in later sections.

Deflection profiles before and after the deposition of a film are subtracted and this difference profile is fit with a parabolic equation to determine the net curvature difference due to the residual stress in the film (refer to the discussion in Chapter 2 for more details on this procedure). This curvature difference is used in the Stoney equation, to determine the residual stress of the deposited film.

In taking an individual deflection/curvature measurement, the wafer is placed on a three point stage and located at the center of the stage using locator rings. These locator rings are also used to maintain the relative orientation of the wafer flat, so as to ensure that the deflection profile is measured along the same line for measurements before and after deposition. Prior to measurement, the wafer is leveled by directing the laser to the center of the wafer stage and adjusting a leveling screw until the reflected spot is centered on the position detector. For measurements taken at elevated temperatures, the stage (which also serves as a hot plate) is covered to help limit heat dissipation and minimize thermal losses and gradients.

3.2.1.1 Calibration of the Curvature Measurement System

The FLX system is calibrated by a trained technician from the manufacturer. The calibration procedure utilizes curvature standards which are polished mirrors of uniform curvature, one standard is typically 20m radius (highly curved) and the other is typically >1200m (nominally flat). These standards are measured in the FLX system and software parameters (presumably gains and/or curve fitting parameters) are varied until the system measurements are

correct. Conversations with representatives of Tencor indicate that, once calibrated, the machine generally does not drift significantly out of calibration over time. The Tencor system used in this work was a shared system housed in a research group outside that of the author's. During the course of this work, the machine was maintained and re-calibrated. Unfortunately, this re-calibration revealed that previous curvature measurements were significantly in error. However, investigating the source of this error with other members of the research group housing the Tencor system revealed that this error was due to use of an incorrect calibration file during a software re-install following a hard drive crash that occurred in the Spring/Summer of 2002, approximately two years before this work had begun.

In order to quantify the curvature differences between the "old"/incorrect and "new"/re-calibrated/correct calibrations, the curvature of several samples was measured using both the old and new calibration files. The curvature of four-inch wafers was measured along the same line for the old and new calibration files (*i.e.,* the wafer is not moved for these measurements). This is repeated two more times after taking the wafer out and putting it back in. Measurements were taken on bare wafers and wafers with stressed films to examine a range of curvatures. In addition, the author also independently obtained a set of mirror standards with 20m, 10m, 5m and >1200m (nominally flat) radii of curvatures from the Spaepen group in Harvard University's Division of Engineering and Applied Sciences. These standards were also measured with the old and new calibration files. A comparison of old and new curvatures is shown in Figure 3-7. The curvatures measured prior to re-calibration can be corrected using the given best fit equation. For films where bare wafer and deposited film scans were both done on the incorrectly calibrated machine, the constant term will drop out and the stress magnitudes can be directly increased by a factor of 2.33. All previously measured curvatures fell within the range presented in Figure 3-7.

Therefore, after establishing this relationship, previous work was corrected and new work proceeded with the recently calibrated/corrected Tencor system. In the data presented in this thesis, no distinction is made between old (corrected after re-calibration) and new (initially measured with correct calibration) data.

3.2.2 Uncertainty Analysis of Residual Stress Measurements

The three measured quantities involved in determining the residual stress in a deposited film via the Stoney equation are the film thickness (h_f), the substrate thickness (h_s), and the curvature difference induced by the film ($\Delta\kappa$). The substrate thickness is measured by a standard micrometer with precision better than 5μm and likely nearer 1μm. A minimum of three measurements taken across the wafer are averaged. The range of these measurements was typically less than 3μm. Therefore, a conservative estimate of the uncertainty in substrate thickness of ±5μm was assumed. Film thicknesses are determined using the calibrated deposition rates presented earlier and a known deposition time. The maximum relative variation in these measured rates is ±9%. Taking into consideration possible uncertainties associated with thickness non-uniformity, it is important to realize that confining the deflection profile measurement to the center 80mm diameter region eliminates the vast majority of the thickness non-uniformities discussed earlier. Considering this, the effect of thickness non-uniformities is minimal and a conservative ±10% relative uncertainty in film thickness is assumed for all thickness measurements in the calculations below. Finally, the relative uncertainty in the curvature measurements was determined by examining the variation of 30 measurements taken along the same line of a wafer. Two standard deviations of the curvatures measured gives relative uncertainties less than ±1%. Furthermore, in this work, an average of three curvature

measurements taken after removing and replacing the wafer are used in determining a residual stress datapoint. Taking this small uncertainty into consideration and recognizing that this relative uncertainty may vary over a range of curvatures, a highly conservative estimate of the relative uncertainty in curvature measurements of ±5% is assumed in subsequent considerations of uncertainties in residual stress analysis.

With the uncertainties in the measured quantities described above, the uncertainty in the calculated residual stress of the film according to the Stoney equation can now be calculated. A quantity (g) derived from a function of three variables (g = f(x,y,z)) each with their own measurement uncertainties (δx, δy, δz) has a total uncertainty (δg) that can be expressed as [78]:

$$\delta g(x,y,z,\delta x,\delta y,\delta z) = \left|\frac{\partial f}{\partial x}\right|\delta x + \left|\frac{\partial f}{\partial y}\right|\delta y + \left|\frac{\partial f}{\partial z}\right|\delta z \qquad (3\text{-}3)$$

Thus, the uncertainty in the residual stress when determined by the Stoney equation is given by:

$$\delta\sigma(\Delta\kappa,h_f,h_s,\delta(\Delta\kappa),\delta h_f,\delta h_s) = \left|\frac{\partial\sigma(\Delta\kappa,h_f,h_s)}{\partial(\Delta\kappa)}\right|\delta(\Delta\kappa) + \left|\frac{\partial\sigma(\Delta\kappa,h_f,h_s)}{\partial h_f}\right|\delta h_f + \left|\frac{\partial\sigma(\Delta\kappa,h_f,h_s)}{\partial h_s}\right|\delta h_s$$

(3-4)

$$\delta\sigma(\Delta\kappa,h_f,h_s,\delta(\Delta\kappa),\delta h_f,\delta h_s) = \left|\frac{E_s}{1-\nu_s}\frac{1}{6}\frac{h_s^2}{h_f}\right|\delta(\Delta\kappa) + \left|\frac{E_s}{1-\nu_s}\frac{\Delta\kappa}{6}\frac{h_s^2}{h_f^2}\right|\delta h_f + \left|\frac{E_s}{1-\nu_s}\frac{\Delta\kappa}{3}\frac{h_s}{h_f}\right|\delta h_s$$

(3-5)

Subsequent data on residual stress will typically be presented along with error bars representing ± δσ where δσ is determined from (3-5).

3.3 *Material, Microstructure and Composition Characterization Techniques*

In addition to residual stress characterization, another focus of this thesis is the characterization of film microstructure and composition. The primary features of interest in film microstructure are crystallographic phase and grain structure. Crystallographic phase is determined here by x-ray diffraction (XRD) with a Bruker D8 diffractometer at the MIT Center for Materials Science and Engineering shared experimental facilities. Images of film grain structure are taken by a variety of electron microscopes in the MIT Center for Materials Science, including transmission electron microscopy (TEM) on a Jeol 2000 FX and Jeol 2010 microscope, scanning electron microscopy (SEM) on a Phillips XL30 environmental SEM, and a Jeol 6320FV field emission high resolution SEM. In addition to electron microscopy images, atomic force microscopy (AFM) images of film surfaces are used to characterize grain size. These images are taken on a Digital Instruments Nanoscope IIIa AFM using a tapping-mode, silicon cantilever with a carbon nanotube tip from MikroMasch (model "Hi'Res") with a maximum tip radius of curvature of 3nm.

The primary technique used for film composition and detection of trace impurities is secondary ion mass spectroscopy (SIMS). Samples for this characterization were approximately 1cm x 1cm squares taken from depositions on 4-inch wafers. Characterization was performed by Evans East Ltd. (www.evanseast.com). In this technique, depth profiling of film composition is done by sputtering away the film by ion bombardment (Cs^+ ions in the results presented here) and analyzing the released material with a mass spectrometer. Quantitative compositions of materials can only be determined after calibration of the spectrometer signal against a known fraction of the material of interest in the same matrix as the material to be analyzed. For Y, O, and Zr, a single-crystal material standard of YSZ is used to establish quantitative calibrations.

For compositional characterization of these major constituents, the accuracy quoted from the vendor is ±10-20%. Calibrated trace impurity signals, however, were not available for their presence in a YSZ matrix. As such, only inferences of relative differences amongst samples are possible.

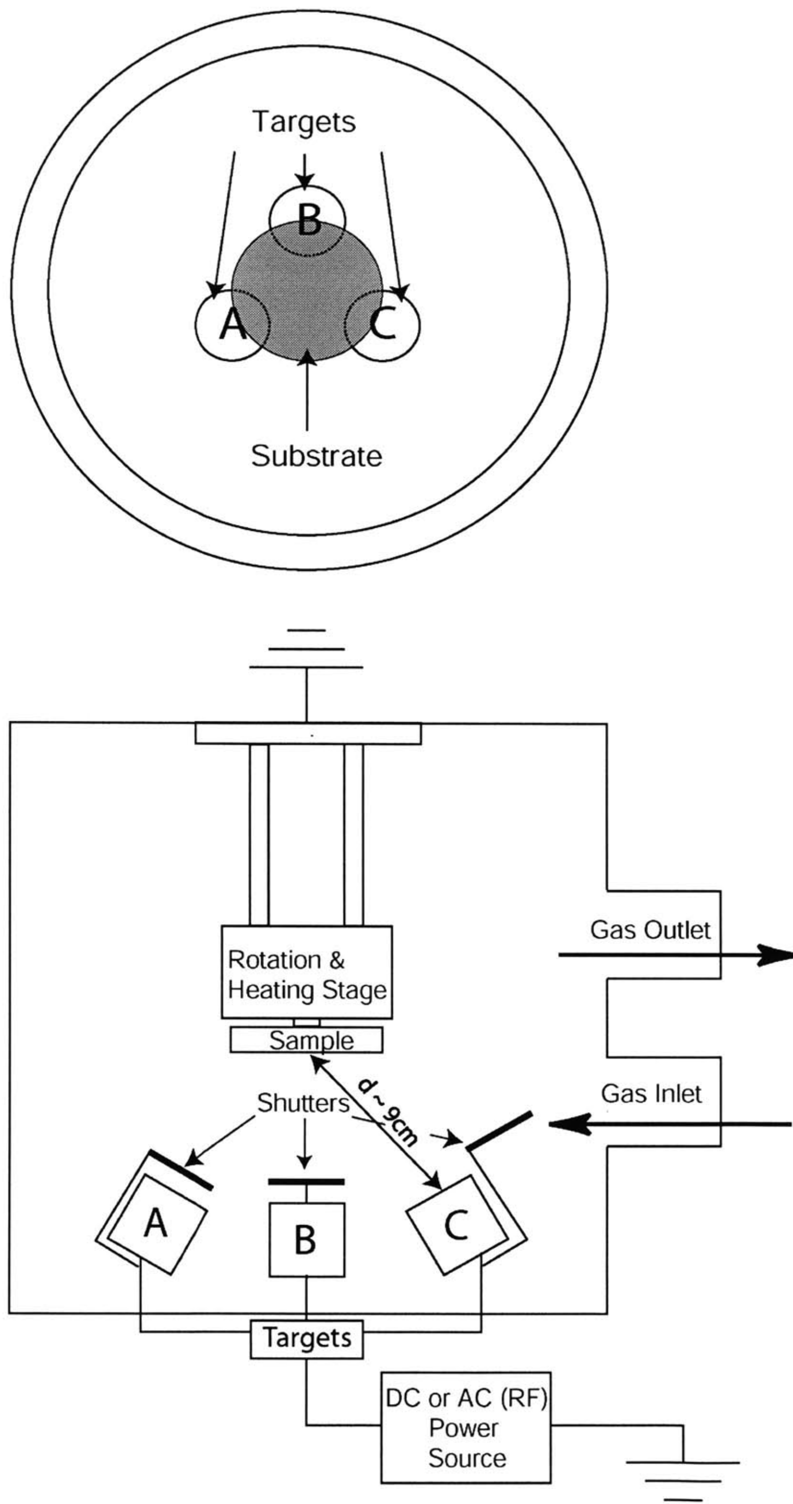

Figure 3-1: Schematic of Kurtis Lesker sputtering system used in this work (top and side-view).

Standard YSZ Deposition Conditions	
Base Pressure	**< 1 x 10^{-6} Torr**
Working Pressure	**10mTorr**
RF Power	**200W (~10W/cm^2 for 2" Dia. Targets)**
Gas Flow Ratio	**9:1 Ar/O_2**

Table 3-1: Standard deposition conditions for YSZ.

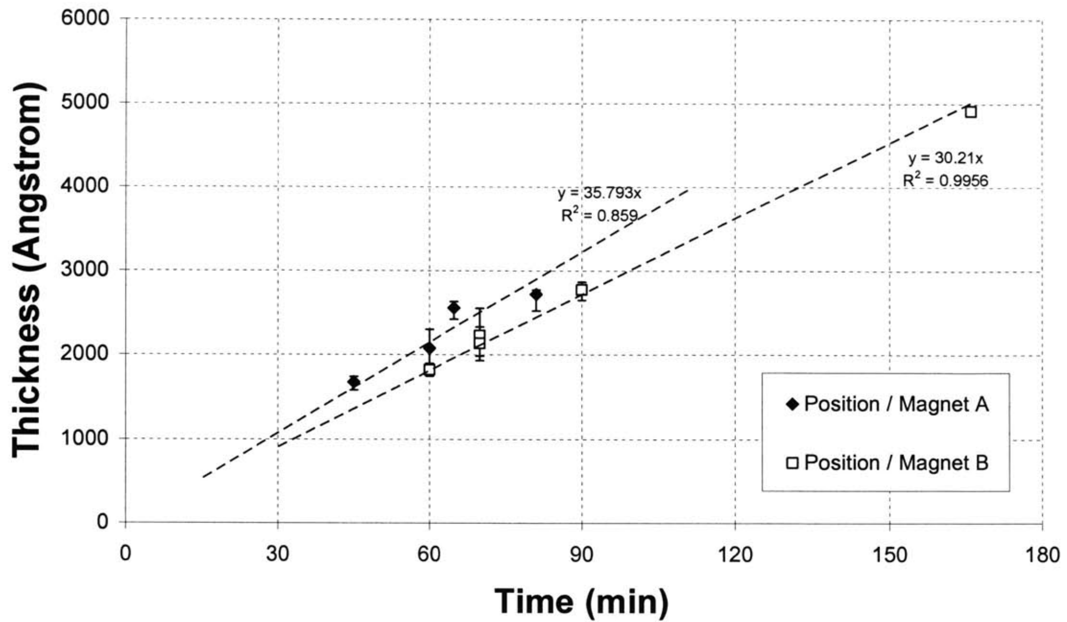

Figure 3-2: Thickness measurements vs. deposition time under standard deposition conditions. Error bars indicate maximum and minimum measurement values. (Position B data provided by J. Hertz)

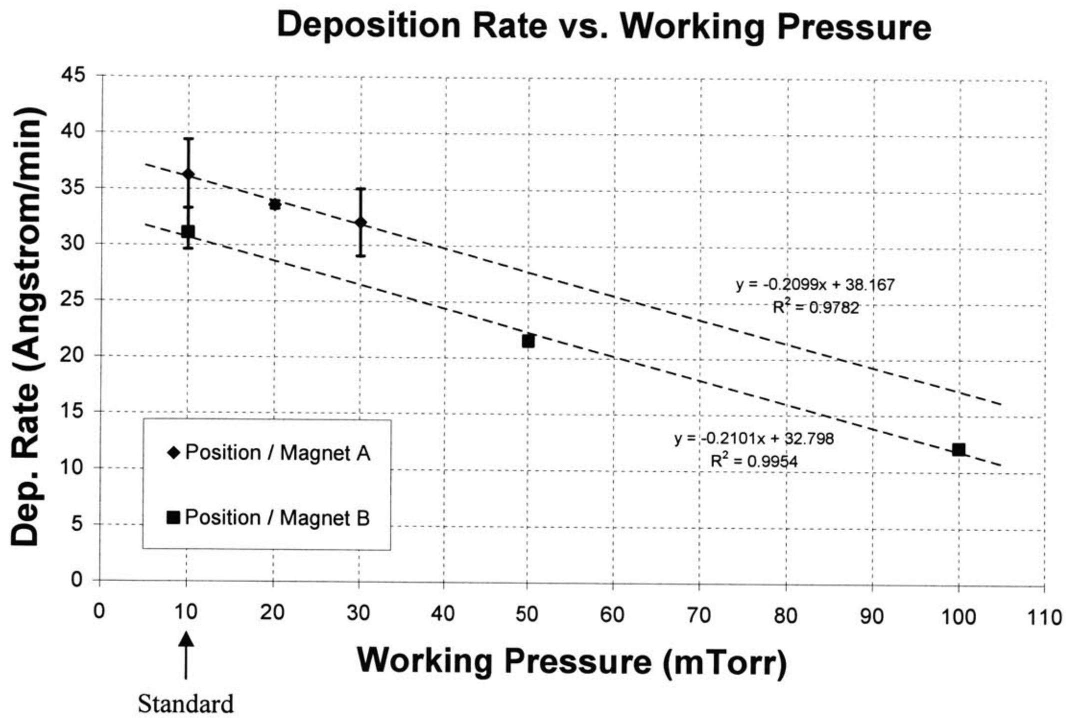

Figure 3-3: YSZ Deposition rate vs. working pressure, all other deposition conditions standard. Error bars indicate maximum and minimum values.

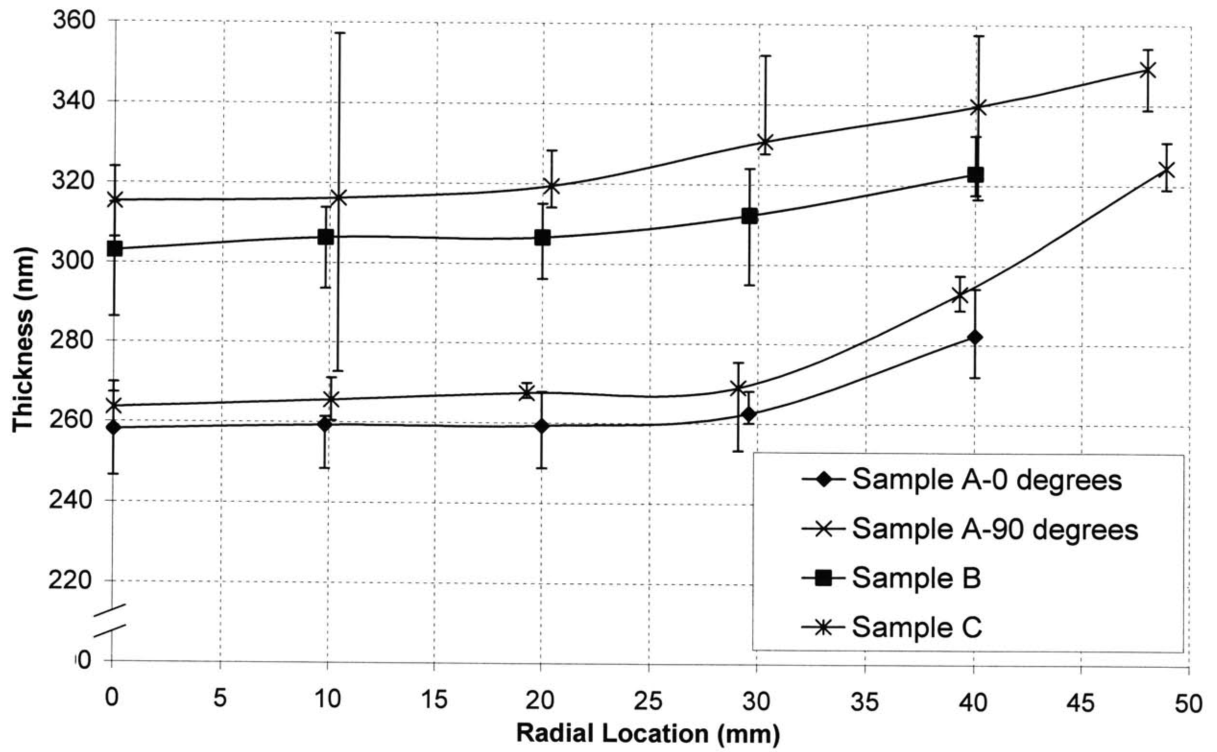

Figure 3-4: Uniformity profiles of YSZ films deposited under standard conditions. Error bars represent minimum and maximum from at least 5 profilometry measurements.

Deposition Conditions for Co-Sputtered Pt-YSZ Composite Anode/Cathode Film (~50/50 wt% composition)					
Power	Base Pressure	Working pressure	Gas Flow Ratio	Substrate Temperature	Deposition Rate
Pt: 20 W – DC (Pos A)	**< 1 x 10^{-6} Torr**	**10mTorr**	**95:5 Ar/O_2**	**600°C**	**145 Ang/min**
YSZ: 200 W – RF (Pos B)					

Table 3-2: Deposition conditions for Pt-YSZ films.

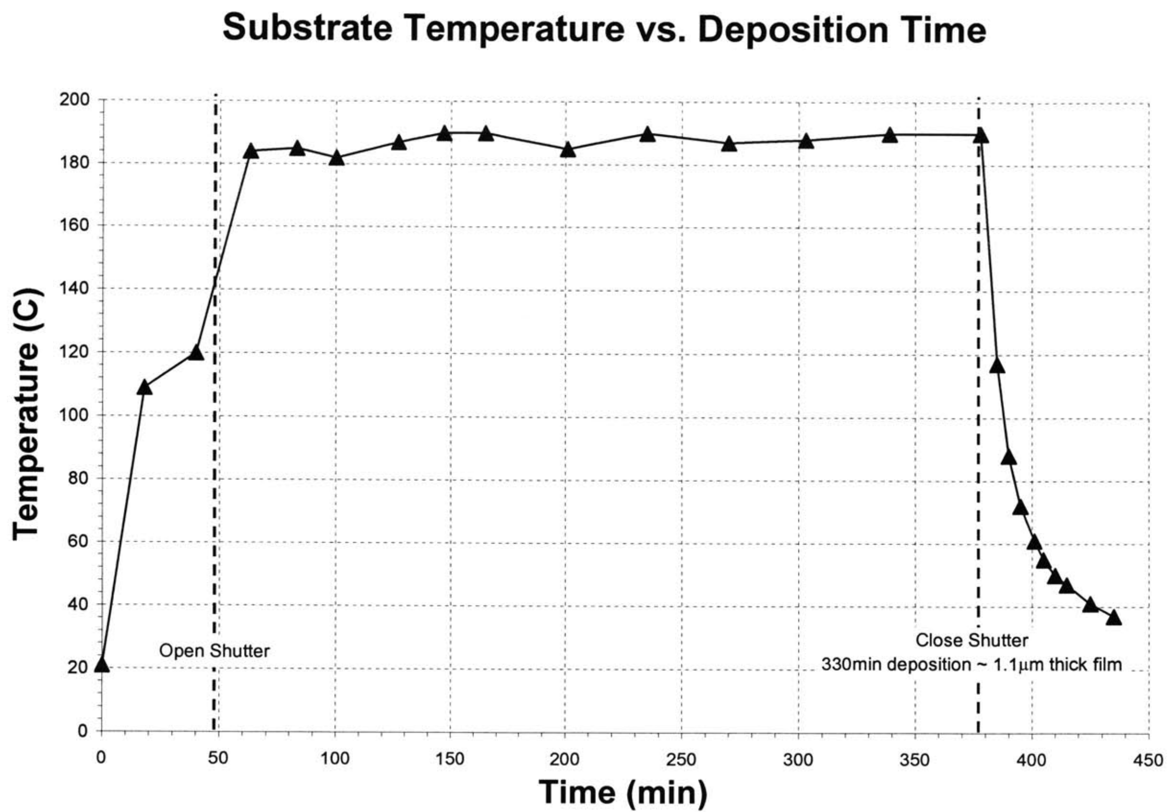

Figure 3-5: Substrate heating during YSZ deposition at room temperature (and standard conditions).

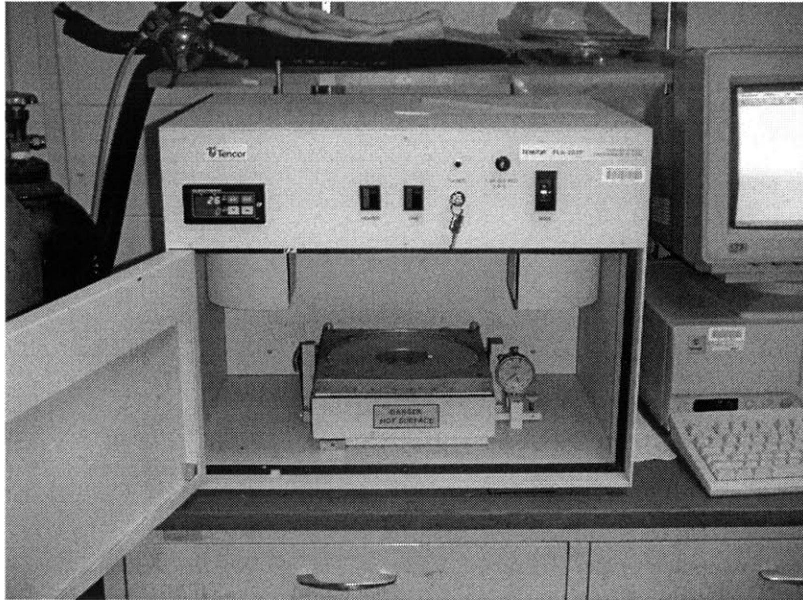

(a)

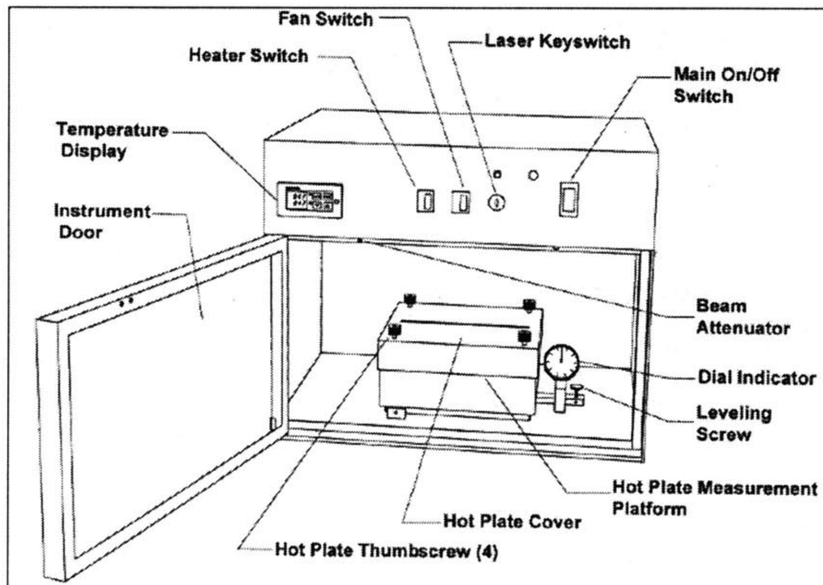

(b)

Figure 3-6: (a) Picture and (b) schematic of Tencor FLX wafer curvature measurement system (schematic taken from [79]).

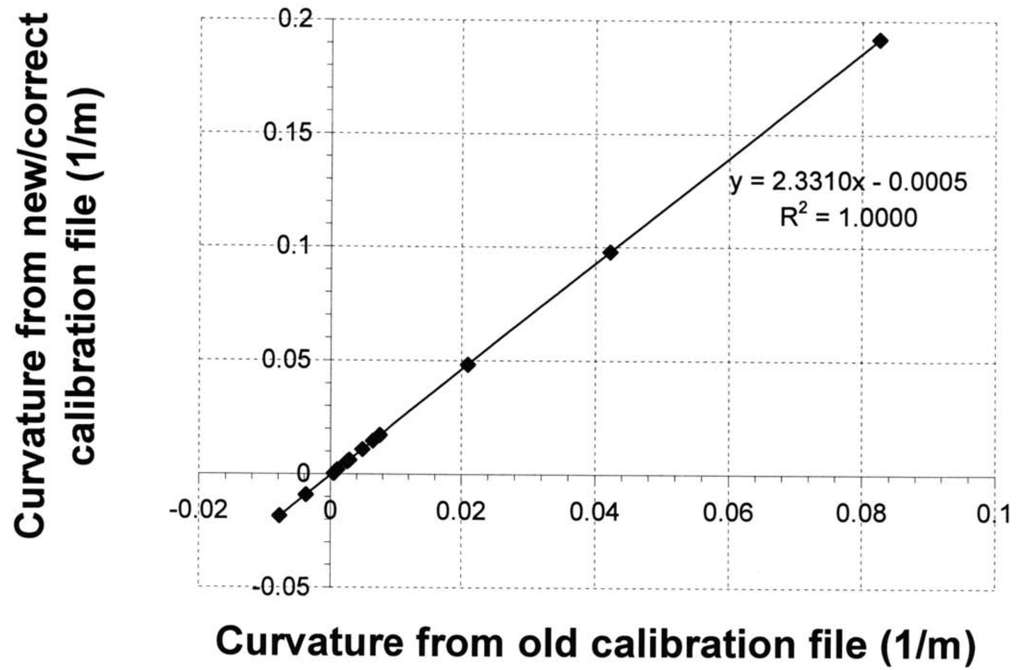

Figure 3-7: Comparison of curvatures measured with old and new/corrected calibration files.

Chapter 4: Residual Stress and Microstructural Characterization of μSOFC Materials

The focus of this chapter is the presence and evolution of residual stress in sputtered yttria stabilized zirconia (YSZ) films. Work done on nominally room-temperature deposited YSZ films is presented first, followed by work done on high-temperature deposited YSZ films. This separation is motivated by the substantially different microstructure and residual stress characteristics observed in high temperature versus room-temperature deposited films. For both room and high-temperature deposited films, composition, crystallographic phase and grain structure are characterized and considered within the context of observed variations in residual stress with deposition process conditions and with post-deposition annealing. This work on YSZ is followed by results from preliminary characterization of residual stress in a representative fuel cell stack structure comprised of a YSZ electrolyte layer sandwiched between composite anode/cathode layers made of co-sputtered Pt and YSZ. Such a structure is currently under investigation for application in microfabricated solid oxide fuel cells (μSOFC's). Where possible, links between observed stress states, microstructure and common mechanisms of residual stress evolution are made.

4.1 Characterization of YSZ Films Sputtered at Room Temperature

Results on YSZ films deposited at nominally room temperature and, unless stated otherwise, standard conditions (see Chapter 3) are presented in this section. Results of microstructural and compositional characterization are followed by the characterization of the as-

deposited residual stress as a function of process conditions as well as the post-deposition evolution of stress with temperature.

4.1.1 Microstructure and Compositional Characterization

Recognizing the inherent link between stress and microstructure, several efforts were made to characterize the composition, structure and morphology of YSZ films sputtered at room temperature. YSZ films were prepared by the reactive sputtering process described in Chapter 3. A 4.7 mol% Y_2O_3 - ZrO2 film ($Y_{0.03}$ $Zr_{0.31}O_{0.66}$ by atom fraction and $Y_{0.09}Zr_{0.91}O_{1.955}$ normalized to one cation) was expected. A typical SIMS composition profile of YSZ films deposited under standard conditions is shown in Figure 4-1, indicating uniform composition through the film thickness. The average results from this sample and two other samples taken over the course of this work indicate an atomic composition of $Y_{0.05}Zr_{0.30}O_{0.64}$ given by SIMS analysis. These results are presented in Table 4-1 along with results gathered by J.Hertz [77] using wavelength dispersion spectroscopy (WDS). The WDS results, along with consideration of the 10-20% error quoted for the SIMS analysis indicates the presence of nearly stoichiometric films.

Two cross-section transmission electron microscopy (TEM) images of films deposited under standard conditions are presented in Figure 4-2. Samples were taken from films deposited on 4-inch Si wafers and were prepared by colleagues in the Department of Materials Science and Engineering at MIT using a standard procedure of bonding, polishing and ion milling. These images indicate films of generally columnar microstructure along with slight widening of grains through the thickness of the film.

A typical x-ray diffraction (XRD) profile of a YSZ film deposited under standard conditions is presented in Figure 4-3. The XRD scan is also presented with standard peak locations and relative intensities of polycrystalline, unstressed, randomly-oriented cubic and

tetragonal YSZ powders. Peaks appear to line up best with cubic structure with slight misalignments attributed to minor differences in composition and the presence of residual strain/stress. This, combined with the presence of the high angle (511) peak and the absence of several of the tetragonal peaks indicates that any crystalline phase of the YSZ film has a cubic structure. Also, the relatively large (200) peak indicates the likely presence of a (200) (*i.e.*, (100)) texture. The observation of a fully cubic structure is consistent with films of comparable compositions deposited by Ji *et al.* [47] as well as the cubic structure observed by Knoll and Bradley [53]. The stabilization of the YSZ cubic structure at room temperature is a result of the standard yttria stabilization mechanism as well as stabilization brought about by decreasing grain sizes, as predicted by Garvie [80, 81] and observed by Ji *et al.* [49].

4.1.2 As-Deposited Residual Stress Characterization

The residual stress present in YSZ films sputtered at nominally room temperature was characterized using wafer curvature measurements following the procedures outlined in Chapter 3. Unless stated otherwise, films have been deposited on 4-inch, (100) Si wafers. Results are presented along with error bars indicative of the uncertainty in stress measurements also discussed in Chapter 3. Total measured stress levels presented in this data include an extrinsic thermal component due to thermal expansion mismatch between the film and substrate in the presence of substrate heating on the order of 185°C (discussed in Chapter 3). After deposition, cooling to room temperature generates a thermal stress component in the film according to:

$$\sigma_{th} = \frac{E_f}{1-\nu_f}(\alpha_{film} - \alpha_s)(T_{final} - T_{initial}) \qquad (4\text{-}1)$$

Implicit in this relationship are standard assumptions including plane stress conditions and uniform through-thickness stresses whereby the relatively low stiffness of the film causes it to be

almost entirely subject to the expansion of the substrate. Using the bulk material properties presented in Table 4-2, one would predict that the cooling process gives rise to a tensile stress component of 268 MPa. It is recognized that the film properties likely vary from the bulk. An evaluation of this possibility and its implications are discussed in Chapter 5.

4.1.2.1 Effect of Film Thickness

The variation of residual stress with film thickness is presented in Figure 4-4. These results include two series of depositions performed over two different periods of time separated by a few months. Comparing the two series of room-temperature depositions, there appears to be a significant increase (~500MPa) in tensile stress levels over time. This observation is further supported by the data of Baertsch *et al.*[13] who used the same apparatus, target and deposition conditions and observed higher levels of compressive stress (ranging from approximately ~2GPa – 400MPa compressive) than those presented for series 1[v].

One hypothesis for this observed behavior was an increased impurity content in films deposited in earlier series of depositions, as during these times the sputtering system was used more frequently with other materials than in more recent depositions. Secondary ion mass spectroscopy (SIMS) analysis was used to characterize trace impurities in the deposited films. Profiles of impurities for samples taken from both series of depositions are shown in Figure 4-5. In this data, results are reported in counts/sec rather than a quantitative percentage or composition because a calibrated profile of these materials in a YSZ matrix was not available. Although absolute quantitative data cannot be extracted relative differences can be inferred. The data indicates that Ca, Na, Ti, and Al are present in both series films. Ca and Al are believed to

[v]This description is taking into consideration the corrected curvature measurements described in Chapter 3 applied to the Baertsch *et. al.* data.

be derived from the sputtering target, as indicated by the compositional data supplied by the manufacturer. Na and Ti are believed to be impurities present in the sputtering chamber due to handling and work done by other users. The SIMS data indicates that relative greater level of Ca impurities in the series 1 depositions may be a cause for compressive stress. However, this can not be said with assurance until a quantitative analysis is performed. In addition, the cause of sharp rise in sodium content through the film thickness for the second deposition series is not explicitly known. However, it is not believed that this could be the cause of compressive stress as the higher sodium content is in the second series data (*i.e.*, the less-compressive series), contrary to what would be required for the observed behavior.

A more likely source of this evolution of stress with time/deposition series is the alteration of bombardment energetics correlating with target wear. Use of a magnetron system creates a characteristic wear in the shape of a ring around the target. This may affect bombardment energetics by increasing working distance and causing a more random emission profile at oblique angles. Both of these phenomenon would serve to increase collisions between sputtered and reflected gas atoms and result in decreased bombardment energy and lower compressive stress generated by the atomic peening mechanism described in Chapter 2. Such characteristic wear has been observed and documented by others [82]. An additional series of stress vs. thickness characterizations using a new, unworn sputtering target would serve as a good indicator of the validity of this conclusion. This is left as a point for future work.

Characteristic behavior of the two series shows a sharp rise in stress (*i.e.*, drop in compressive stress magnitude) with increasing thickness from 0-100nm transitioning to a nearly constant value at thicknesses greater than 300nm. In these films it is believed that the compressive stress component develops due to lattice distortion and interstitials generated by the

atomic peening process described in Chapter 2. The effects of implantation and cascading collisions are most severe within the first few nanometers of the film surface [20]. Underlying atomic layers of the deposited film have more time to relieve some portion of this compressive stress due to diffusion processes which are promoted by temperatures generated by substrate heating, as documented in Chapter 3, and kinetic energy imparted during bombardment. Therefore, thinner films are given less time to undergo such stress relief and a greater portion of the film thickness is affected by peening-generated stresses, resulting in a larger overall level of compressive stress. A second, related mechanism of compressive stress generation is the enhancement of free-surface stresses due to non-equilibrium atomic spacing as described in Chapter 2. Similar to the peening stresses, the effects of these surface stresses would be more pronounced in thinner films than thicker films. Thus, both the peening stress and surface stress mechanisms help account for an increase in net compressive film stress for thinner films due to the enhanced effects of stress in the film surface layers.

Another likely contribution to the sharp rise in stress with thickness is the development of a tensile stress component during the growth process through grain and void coalescence mechanisms described in Chapter 2. Planar view, high resolution SEM images illustrating increased grain size during this growth process are presented in Figure 4-6 to support this view. These images qualitatively illustrate grain growth as well as increasing grain cluster regions, indicative of the progression of coalescence and the "zipping up" processes generating elastic stress/strain. These observations are further confirmed by AFM images where image processing tools are used to measure grain sizes. Z-height images of 240, 500 and 988 nm thick films are shown in Figure 4-7. These images illustrate similar growth behavior as the high-resolution SEM images. Image processing tools within the Nanoscope AFM software were used to

measure the grain size of these films. In this software, a low pass filter was applied to the data, followed by a z-height flattening algorithm. The combined effect of these tools is to accentuate the image contrast at grain boundaries, which are low frequency, high z-height amplitude features. A typical post-processing image is shown in Figure 4-8. With these images, grain size was measured by examining z-height section profiles of zoomed images to identify the distance between grain boundaries. Comparing grain sizes of thinner and thicker films, as in Figure 4-9, reveals the growth of grains with increasing thickness and a plateau of grain growth that roughly coincides with the plateau in residual stress. This stress plateau at "thicker" films is consistent with work done by Hoffman [26] and cited by Knoll and Bradley [53] indicating that the stress of sputtered films varies little in the 0.2 – 1.5μm thickness range.

Finally, the stress magnitudes themselves are in line with the observations of Gao *et al.*, who observed a few hundred MPa compressive stress in ~500nm thick YSZ films with a fully cubic structure [51]. However, the stress levels are lower than other data reported in the literature from Knoll and Bradley [53] and Carniero *et al.*[61]. However, this is not surprising when considering that these studies used deposition conditions that are more likely to promote higher bombardment energetics (*i.e.*, higher power densities, substrate biases, etc.) which would lead to higher compressive stresses due to atomic peening.

4.1.2.2 Effect of Working Pressure

The measured residual stress in YSZ films deposited at room temperature and various working pressures is presented in Figure 4-10. These results are all taken during the time period for series 1 depositions discussed earlier. The data indicate a sharp dependence of stress on working pressure typical of sputtered films under moderate to high levels of energy bombardment. This correlation is attributed to the forward sputtering/atomic peening process

discussed in the previous section and in Chapter 2, whereby higher working pressures result in lower energy bombardments, resulting in reduced compressive stress due to reduced lattice distortion from interstitial surface atoms and/or implanted gasses. Furthermore, results indicate a sharp rise in residual stress levels between 10 – 20mTorr. Over this pressure range, total stress levels transition from compressive to tensile. This is consistent with several previous studies of the variation of residual stress with working pressure in sputtered films of various materials [20, 24].

Finally, it is important to note that changes in substrate temperature during deposition at various working pressures are assumed to be negligible based on the results of Knoll and Bradley, who observed only minor changes in substrate temperature (<10%) between films deposited under low and high bombardment energy conditions (unbiased vs. biased) [53]. Therefore, the extrinsic thermal component is roughly the same as quoted previously regardless of working pressure with the same caveats regarding film vs. bulk material properties.

4.1.3 Residual Stress Evolution With Post-Deposition Thermal Cycling

Several factors related to the design and operation of microfabricated solid oxide fuel cells motivate the need for information on residual stress evolution with post-deposition thermal excursions. First, during operation, μSOFC's will be subject to multiple start-up/shut-down thermal cycles to relatively high temperatures (expected to be ~600°C for the systems being considered here). Knowledge of stress and structural evolution with these cycles is an important input for the design of structurally viable devices. Similarly, this stress evolution with post-deposition temperature is important for maintaining the integrity of both released and unreleased films during fabrication routes as subsequent fabrication steps/routes may also subject deposited films to high temperatures.

In order to investigate the evolution of stress with post-deposition thermal excursions, film stress was measured as a function of temperature using the high temperature apparatus available on the Tencor stress measurement system described in Chapter 3. Films were heated at a rate of approximately 5 °C/min up to maximum temperatures around 400-500°C and then held at this maximum temperature for a period ranging from 15min – 1.5hrs. A typical dataset for room-temperature deposited films is shown in Figure 4-11 (remaining data sets are presented and discussed below). The stress vs. temperature behavior during the first thermal cycle of room-temperature deposited films exhibits four characteristic regions: (1) an initial linear decrease in total stress due to thermal stresses arising from coefficient of thermal expansion (CTE) mismatch between the film and substrate, (2) a sharp rise in total stress beginning at approximately 150-200°C and continuing through the maximum cycle temperature, (3) increasing tensile stress development when held at this maximum temperature and (4) linear tensile stress development during cooling due to CTE mismatch. Subsequent cycles exhibit only the expected linear behavior, following the slope of the cooling portion of the curve seen in the first cycle, indicating that the temperature-driven stress generation or relief mechanisms are complete within the given temperature range after one cycle.

Stress vs. temperature during initial thermal cycles of several other films are shown in Figure 4-12. The data indicate that the hysteretic behavior during the first cycle is consistent for room-temperature deposited films in either deposition series as well as for maximum temperatures ranging from 400°C – 500°C. The final stress state of the film upon returning to room temperature consistently falls within the range of 560MPa +/- 100MPa, indicating that the final stress state of the film is roughly independent of the deposition series, maximum temperature and hold time within the range of variables explored. In addition, this hysteresis

also appears independent of film thickness, as comparable final stress magnitudes were observed for a 95nm thick film.

The data in Figure 4-12 also indicates that a few samples undergo an increase in compressive stress between their initial as-deposited stress (indicated by the first data point in each cycle) and their initial stress state at the beginning of the thermal cycle (represented by the second data point of a cycle). Where observed, this stress development occurs over several months and may result from a combination of environmental and/or creep-like processes. One such possibility is the enhancement of a film's native oxide layer over time. As discussed previously, enhanced oxidation may give rise to compressive stress. However, a detailed investigation of this compressive stress development was not conducted as part of this work.

Several explanations for the observed stress hysteresis were considered. The first was the presence of a crystallographic phase change. This possibility is especially relevant considering the large variations in observed phases in thin-film YSZ discussed in Chapter 2. Also, Ji *et al.* observed unstable tetragonal phase in as-deposited pure zirconia films that began to revert to the expected monoclinic phase during post-deposition annealing [49]. Similarly, Chung discusses low temperature phase degradation of YSZ for long period low temperature anneals [48, 83]. However, as can be seen in Figure 4-13, x-ray diffraction scans of as-deposited and post-thermally cycled films do not show changes and development of peaks that are indicative of a crystallographic phase change. In both scans, the crystalline regions of the film appear to be purely cubic as discussed in section 4.1.1.

Consulting the literature regarding stress evolution of sputtered films indicates that several authors have observed somewhat similar behaviors. Fong [84], Doerner and Nix [25], Harting *et al.* [85] and Hodge *et al.* [86] observe moderate peaks or plateaus in compressive

stress in sputtered metal films during thermal cycling. Oftentimes, however, these behaviors are attributed to classical plasticity and film yielding. The film does not transition from compressive to tensile stress in these studies as it does here. However, in the study done by Fong [84], a sharp peak (rather than a plateau) in the compressive stress of sputtered Cu, resembling that seen here for YSZ, occurs at approximately 200°C and it is proposed that this peak is due to the development of a tensile stress component due to grain growth above 200°C as proposed by Chaudhari [32] and recent revisions of that work by Estrin [87]. However, despite the sharp peak and apparent beginning of a stress transition, the films in that work appear to yield at higher temperatures, keeping the total film stress compressive during heating. Considering the possibility of grain growth, examining Figure 4-13 indicates slight intensification and narrowing of diffraction peaks that may be indicative of the early stages of grain growth. However, the lack of a strong distinction between the annealed and as-deposited scans combined with the relatively low homologous temperatures during annealing ($T/T_m < 0.25$) make significant grain growth unlikely as the source of the observed hysteresis.

In addition, it is possible that tensile stress may develop due to crystallization during heating of amorphous regions present in the as-deposited film. The likelihood of a mixed amorphous/crystalline structure will become more apparent in subsequent discussions of high temperature deposited films and in the preliminary mechanical property assessment presented in Chapter 5. If a mixed amorphous/crystalline film is present, the development of tensile stress due to crystallization would be accompanied by increases in the intensity and sharpness of XRD peaks of annealed films vs. as-deposited films. While the profiles shown in Figure 4-13 do exhibit slight intensification and narrowing, this does not seem conclusive. Thus, the possibility

of crystallization as a source of tensile stress development during annealing remains a matter for further investigation.

Another possible explanation of the observed hysteresis is the diffusive release of implanted sputtering gases from the film. As discussed in Chapter 2, although the experimental evidence presented by Thornton [42] indicates that the impact of implanted gasses on compressive stress is minimal, there does exists some debate over the effects of implanted gasses on the stress state of sputtered films. Therefore, in order to assess whether this stress hysteresis can be correlated with sputter gas implantation and subsequent release during annealing, SIMS profiles of Argon content were taken of as-deposited films and films annealed at 500°C for 1hour and 1000°C for 4 hours. These samples were approximately 10mm square and taken within the center 1 inch diameter of a 4" wafer in order to limit any affects of compositional non-uniformities. Results of this analysis, shown in Figure 4-14, indicate that the Argon content increases slightly for annealed films. This observation is unexpected but believed to be at least in part due to variation amongst samples. Additional detailed consideration is left as a matter of future work. However, the results do establish that it is unlikely that diffusive release of the sputtering gas is the major contribution to the observed stress hysteresis.

It is believed that it is primarily the diffusion of deposited film interstitials and not diffusive release of implanted gases that account for the observed stress relief. Diffusion of interstitial atoms into standard lattice sites, which would tend to relieve compressive mismatch strains, is believed to occur at a faster rate than grain boundary diffusion, which would tend to relieve tensile mismatch strains generated in the grain-coalescence (*i.e.*, "zipping up") process during deposition. This proposed process is supported when considering the fact that both the penetration depth of sputtered atoms and the effects of the cascading collisions that motivate the

forward sputtering/atomic peening process occur predominantly within a few atomic layers of the film surface [20, 44]. A film in its as-deposited state will likely have many more interstitial atoms near it surface than in underlying layers as these layers have had time and energy (provided by substrate heating and bombardment during deposition) for a greater number of interstitial atoms to diffuse into standard lattice sites. Therefore, diffusion of interstitially displaced atoms manifests itself primarily as surface diffusion. General relationships for bulk lattice (L), grain boundary (GB) and surface (S) diffusion coefficients established by Balluffi *et al.* [88] and Gjostein [89] and cited by Ohring [18] for FCC metals as a function of temperature (T) and melting point (T_m) in Kelvin are:

$$D_L = 0.5\exp\left(\frac{-17.0T_m}{T}\right)\frac{cm^2}{s}$$

$$D_{GB} = 1.5\cdot 10^{-8}\exp\left(\frac{-8.9T_m}{T}\right)\frac{1}{\delta_{GB}}\frac{cm^3}{s} \qquad (4\text{-}2)$$

$$D_S = 0.014\exp\left(\frac{-6.54T_m}{T}\right)\frac{cm^2}{s}$$

Where δ_{GB} is the grain boundary width, typically on the order of 5-10 Angstroms. Using an intermediate value of δ_{GB} = 0.7nm and taking T_m = 2500°C these relationships are plotted on log scales in Figure 4-15. Assuming that the relative orders of magnitude of these relations will hold for FCC oxide (such as YSZ) as well as metal films, and also assuming that diffusion distance required for compressive stress relief by interstitial diffusion is on the order of one half the lattice parameter (a = 0.512 – 0.515 nm for cubic YSZ) and tensile stress relief by grain boundary diffusion is at least this large (likely larger), it can be seen from Figure 4-15 that surface diffusion will proceed several orders of magnitude faster than grain boundary diffusion over the

temperature range (25-500°C) explored here, offering support for this proposed mechanism of compressive stress relief and net tensile stress development.

In order to more fully understand the role of distortion by atomic peening on this hysteretic process, thermal cycles were performed on films deposited at varying working pressures. The data, presented in Figure 4-16, indicates that while films deposited at low working pressures (5mTorr and 10mTorr) exhibit comparable stress hysteresis, films deposited at high working pressure (20mTorr) indicate significantly lower total stress hysteresis. This observation correlates with an observed transition in the as-deposited stress state of the film. It is believed that the atomic peening mechanism responsible for this initial stress state is also responsible for the observed decrease in stress hysteresis. That is, films deposited at higher working pressure have fewer implanted/driven interstitials due to reduced bombardment energy, resulting in reduced stress hysteresis. This behavior correlates well with the hypothesis of diffusion-driven stress hysteresis. However, Figure 4-16 also indicates that the magnitude of the final stress state of thermally cycled films deposited under varying working pressures depends on the deposition pressure. This seemingly contradicts this hypothesis that the stress hysteresis is due to reduced lattice distortion due to diffusion. If the hysteretic behavior is predominantly due to lattice distortion by atomic peening, one might expect the final film stress after thermal cycling to be independent of deposition pressure just as it was independent of initial stress state and film thickness. One possible explanation for why this is not the case here is that films deposited at higher working pressures may also have different microstructures. Specifically, the films may have higher void content. Increased void content typically correlates with lower tensile stress levels, as discussed in Chapter 2. Additional characterization and tests that further

support this and the general question of the source of the observed hysteresis are discussed in Chapter 5.

4.2 High-Temperature Sputtered YSZ Films

In light of the fact that film structure and properties (including residual stress state) oftentimes change dramatically with elevated substrate temperature, preliminary work has been done to examine the effects of elevated substrate temperature on sputtered YSZ film properties. High temperature (600°C) depositions were performed using the reactive sputtering procedure described in Chapter 3. In parallel to the previous discussion on room-temperature deposited films, results of microstructural characterization of high-temperature deposited films is followed by as-deposited and post deposition residual stress characterization.

4.2.1 Microstructural Characterization

Compositional analysis of YSZ films deposited at nominally 600°C substrate temperature are presented along with the previously presented averages for room temperature films in Table 4-3. While a SIMS profile of a single high temperature sample indicates the possibility of enhanced oxidation, WDS characterization of films deposited at a comparable temperature indicates that this data may be questionable. Further compositional investigation of these films is left as a matter of future work. However, it is currently believed that high temperature films, as room temperature films, are nearly stoichiometric.

XRD profiles of films deposited nominally at room and 600°C substrate temperatures are compared in Figure 4-17. Both films appear to exhibit a cubic, (100) textured structure. However, there is significantly higher peak intensities accompanied by peak narrowing in the high-temperature deposited films. This is indicative of a different microstructure for high

temperature films, specifically there is a likelihood of increased crystalline phase in the high temperature films. Similar observations have been made in other work where the onset of significant crystallization of YSZ occurs between deposition or post-deposition anneal temperatures of 325 and 450°C [90, 91].

AFM images of as-deposited room temperature and high temperature samples of comparable thickness are shown in Figure 4-18. The images indicate that high temperature films have larger grain structures, comprised of many more distinct, individual grains, rather than many clusters of grains with sometimes indistinguishable grain boundaries that are observed for room temperature films. The observed differences in microstructure can be attributed largely due to enhanced mobility of the deposited film during the growth process.

4.2.2 Effect of Deposition Temperature on Residual Stress

Not surprisingly, the differences in microstructure between high and room-temperature deposited films gives rise to significantly different residual stress states. The total residual stress for films deposited at nominally room, 300°C and 600°C substrate temperatures for two different working pressures (all other conditions otherwise standard) is presented in Figure 4-19. Again, the data in Figure 4-19 includes contributions of stress from the intrinsic (growth) stresses and a thermal component due to cooling to room temperature from the deposition temperature. Thermal stress components for YSZ films on Si are expected to be tensile due to the higher CTE of YSZ. Using bulk material properties, these tensile stress components would be 344, 592, and 1237 MPa at nominally[vi] room temperature, 300°C and 600°C, respectively. Generally, one would expect the magnitude of the intrinsic stress component to decrease with increasing substrate temperature due to diffusive stress relief mechanisms (discussed in Chapter 2).

[vi] As presented in Chapter 3, it was found that nominally room temperature films have a substrate temperature of ~185 °C.

However, the data here suggests that the intrinsic compressive stress increases for high-temperature depositions. This is readily seen in the data of films deposited at 10mTorr, where the total stress for 600°C depositions (~1GPa) is significantly more compressive than room and 300°C depositions. Subtracting the tensile thermal components to isolate the intrinsic stress components would add to this compressive stress evolution. Similarly, taking this tensile thermal stress component into account for films deposited at 20mTorr also indicates the presence of compressive stress development between 300°C and 600°C deposition temperature. A few possible explanations for this behavior are discussed below.

Enhanced oxidation at grain boundaries may generate additional compressive stress levels. As discussed previously, the SIMS data presented in Table 4-3 suggests higher oxygen levels for high temperature vs. room temperature films. Again, however, this data is generally inconclusive, especially considering the 10-20% error associated with compositional analysis quoted for SIMS. A comparison of SIMS impurity profiles of room and high-temperature deposited samples was made in order to investigate the possibility of increased impurity content of the high-temperature deposited films. This data is presented in Figure 4-20. As before, data here is presented in counts per second as no calibrated standard exists for these materials in a YSZ matrix. However, this data does not indicate a significant difference in impurity content that one would expect to cause additional compressive stress.

The most likely cause of the difference in intrinsic stress levels is differences in the crystalinity of the film. While the XRD profiles presented in Figure 4-17 do not indicate differences in crystallographic phase (both appear cubic), the increased crystallinity suggested by the relative peak intensities may help explain the differences in stress. In a more highly crystalline film, one would expect compressive stresses generated by atomic peening

mechanisms to be more pronounced as the mechanism is based on the distortion of a crystal lattice.

4.2.3 Effect of Film Thickness

In order to more fully compare the stress state of high and low temperature deposited films, the stress vs. thickness behavior of high temperature films was characterized and is presented in Figure 4-21. Similar to room-temperature deposited films, stress increases with film thickness. It is believed that this is occurring by the same combination of atomic peening and tensile stress development due to evolving grain structure as discussed with room-temperature deposited films. In considering the tensile coalescence stress evolution mechanism in the context of possible mixed amorphous/crystalline mixed phases in room temperature films, it is important to note that Floro *et al.* [33] have shown that coalescence stress mechanism may also be applied to amorphous films moving from an isolated island to continuous structure during deposition.

4.2.4 Effect of Working Pressure

Residual stress vs. working pressure of sputtered YSZ films is presented in Figure 4-22. The data indicates similar behavior as observed with room-temperature deposited films, again confirming the influence of atomic peening effects on film stress. As in room temperature films, there is a transition in the stress state between 10mTorr and 20mTorr.

4.2.5 Residual Stress Evolution With Post-Deposition Thermal Cycling

In examining stress evolution with post-deposition thermal excursions, the data shown in Figure 4-23 exhibits the same four regions as in room temperature films. There is an initial decrease in stress due to thermal expansion mismatch, followed by a stress transition, additional tensile stress development when held at maximum temperature and finally linear behavior during

cooling to room temperature. As in room temperature films, subsequent cycles also exhibit only a linear development of stress due to CTE mismatch. However, several distinguishing characteristics exist for high temperature versus room-temperature deposited films, most notable is the severity of the stress transition and the temperature at which this stress transition occurs. In the high temperature films, stress relief is delayed until approximately 400°C and does not result in a transition to net tensile stress. Furthermore, the total stress level remains compressive when cooled to room temperature. Another distinguishing characteristic of the high temperature thermal cycles is the greater slope of the linear portions compared to room temperature films. This slope has implications on the apparent mechanical properties of the films and is discussed in more detail for both room and high temperature films in Chapter 5.

The absence of the large hysteretic behavior exhibited in room-temperature deposited films may be attributed to the fact that these measurements are taken after the film has essentially been subjected to an annealing step during the cool-down portion of the deposition process. Because the cool-down portion of the deposition process is programmed to proceed at ~5°C/min, this annealing process is comparable to those used for room temperature thermal cycles. During this process, the proposed stress hysteresis due to diffusive relief of lattice distortion may occur. That is, neglecting the possibility of yielding, the film may have only partially undergone the stress relief process. The behavior observed here for post deposition annealing may be indicative of the completion of this process. In either case, it is clear that more work is necessary to more fully investigate the post deposition thermal cycling behavior of high-temperature deposited films. Suggested paths for investigation are discussed in Chapter 6.

4.3 *Preliminary Residual Stress Characterization of μSOFC Structures*

Until now, this chapter has focused on residual stress and structural evolution of a possible electrolyte layer (sputtered YSZ) for a microfabricated solid oxide fuel cell. However, it is recognized that knowledge of the residual stress evolution of an entire fuel cell stack structure (including any supporting layers present) is also of great interest. While work done by others in the collaborative μSOFC research effort, of which this thesis is a part, has explored deposition and characterization of several anode and cathode materials for integration into fuel cell stacks, many of the deposited materials and processes have not proven robust enough for integration into device-level concepts. However, one novel material which is particularly attractive as an anode and cathode due to its potential for high triple phase boundary length and ease of integration into the fabrication process is a co-sputtered film of platinum and YSZ (Pt-YSZ). The remaining sections present preliminary work done to investigate the residual stress state of this film material as well as representative fuel cell stacks comprised of Pt-YSZ/YSZ/Pt-YSZ trilayers with a Ti adhesion layer.

4.3.1 Anode/Cathode Material: Pt-YSZ

The residual stress evolution with post deposition temperature of a 730nm thick Pt-YSZ film deposited on Si is presented in Figure 4-25. These and all Pt-YSZ layers discussed here are deposited at high temperatures (~600°C). The remaining deposition conditions of Pt-YSZ films were presented in Chapter 3. Beginning from an initially tensile stress state (due in part to an extrinsic thermal component generated upon cooling after deposition), the composite Pt-YSZ film initially undergoes a decrease in stress due to CTE mismatch between the film and substrate. However, at approximately 150°C, the film stress decreases sharply. Currently, the exact reason

for this behavior is unknown. Two possibilities are densification or crystallization of the film. Crystallization at such a low temperature however is believed to be unlikely when considering the fact that the major motivating factor for high-temperature deposition of these films is their lack of crystalline phase at temperatures below approximately 500°C. Further work is necessary to investigate the possibility of densification. Following this decrease in stress and transition to compressive total stress, the film stress plateaus in a manner indicative of compressive yielding. No significant creep is observed when held at 450°C. Cooling exhibits essentially linear stress development due to CTE mismatch, returning the composite film to room temperature with a compressive stress state. A subsequent cycle exhibits essentially linear stress development with some yielding and stress hysteresis at or near the maximum cycle temperature.

4.3.2 Fuel Cell Trilayer: Pt-YSZ/YSZ/Pt-YSZ on Si

As a preliminary evaluation of the residual stress state and evolution with temperature for a representative stack comprised of Pt-YSZ and YSZ, a Pt-YSZ/YSZ/Pt-YSZ trilayer was deposited on Si and subjected to a thermal cycle. Deposition conditions for Pt-YSZ layers are presented in Chapter 3. The YSZ layer is deposited at 600°C and otherwise standard conditions, presented in Chapter 3. The stress vs. temperature evolution of the trilayer is shown in Figure 4-25. Again, initial stages of heating give linear stress development. This is followed by a decrease in stress similar to that seen for the pure Pt-YSZ layer. However, this decrease in stress is then followed by significant tensile stress development and creep-like behavior at the maximum cycle temperature similar to the hysteretic behavior observed for pure YSZ films. This behavior is indicative of a combination of the atomic peening relief mechanism proposed for YSZ, film yielding and the currently unkown compressive stress generation mechanism present in the Pt-YSZ. Unlike the pure Pt-YSZ films, this combination of effects results in a

tensile stress state when returned to room temperature. Similar to the pure Pt-YSZ behavior, a second cycle shows linear behavior combined with moderate hysteresis.

4.3.3 Fuel Cell Trilayer: Pt-YSZ/YSZ/Pt-YSZ with Ti adhesion layer on SiN/Si

During the course of this work, several proposed designs for μSOFC device structures have included the use of an underlying SiN film, either as a structural support or as an etch stop for integration of KOH etch processes. Proper adhesion of the Pt-YSZ/YSZ/Pt-YSZ stack to the SiN film necessitates the use of a thin Ti film. Therefore, preliminary work has been done to investigate the stress evolution of Pt-YSZ/YSZ/Pt-YSZ/Ti stacks on Si wafers coated with a low-stress silicon nitride. The effects of this Ti layer are also characterized.

Residual stress measurements of Ti films of two thicknesses are shown in Table 4-4. It should be realized that the curvature differences measured in these films are close to or within variations of a single measurement. Furthermore, a thermal cycle of a nominally "thick" (~20nm) Ti film, showed in Figure 4-26, revealed no stress evolution, not even the expected linear stress evolution due to CTE mismatch. Thus, while the inverse relationship of film stress with film thickness implied by the Stoney equation results in apparently significant stress levels, it is believed that the Ti films deposited are likely not continuous and/or have minimal levels of residual stress. However, further work presented below indicates that, despite the possible low integrity of the Ti films, they nonetheless are important for structural integrity and residual stress evolution of subsequently deposited films.

The stress evolution of Pt-YSZ/YSZ/Pt-YSZ/ stacks on both nominally thin (*i.e.* 5-10nm) and thick (*i.e.* ~20-30nm) Ti adhesion layers on a SiN coated Silicon substrate was performed. The stress evolution for two different stacks deposited on "thin" (nominally 5-10nm) Ti adhesion layers are shown in Figure 4-27. Like the trilayer stacks deposited on Si, these stacks exhibit

stress evolution indicative of the combined effects of the Pt-YSZ and YSZ layers with the change in compressive stress evolution apparently less drastic than previously observed for Pt-YSZ and trilayer stacks. However, the use of a thicker 20nm Ti adhesion layer, as presented in Figure 4-28, appears to markedly change the characteristics of the stress-temperature profile. In this structure, the stress development in the initial cycle is nearly linear through the heating portion with compressive stress development delayed until the film stack is held at 500°C. This data suggests the possibility that, although the stress in the Ti adhesion layer may not significantly influence the net stress of the stack structure, it may affect the stress state indirectly by inducing changes in microstructure. Investigation of this, along with repeating these preliminary experiments, is a matter for future work. In any case, the important information to come from this preliminary work is the knowledge that the as-deposited, net stress state of fuel cell stacks comprised of Pt-YSZ/YSZ/Pt-YSZ may be either tensile or compressive, is affected by the underlying adhesion layers and may change in sign and magnitude with post-deposition thermal excursions.

4.4 Conclusions

This chapter has focused on residual stress and microstructural characterization of materials for a microfabricated solid oxide fuel cell with particular emphasis on a sputter-deposited YSZ electrolyte film. In columnar, cubic, nanostructured films less than one micron thick, as-deposited stress states are greatly influenced by compressive stresses generated by the atomic peening process during deposition. This peening process, combined with tensile stresses generated by grain coalescence and evolution combine to give as-deposited total residual stress states for YSZ on Si ranging from -1400MPa to 200MPa and -1600MPa to 400MPa for films deposited at room and 600°C substrate temperatures, respectively, over a range of film

thicknesses (5nm - ~1 μm) and working pressures (5mTorr – 100mTorr). Differences in stress states of high temperature and room temperature films are attributed to microstructural differences believed to be manifest in higher degrees of crystallization in high temperature films. Post-deposition annealing up to 500°C causes the development of up to ~1GPa of tensile stress that, for room-temperature deposited films, causes the stress state of the film to change from compressive to tensile. It is hypothesized that this transition is due to diffusion-based phenomena relieving compressive stresses generated by the forward sputtering/atomic peening process.

In addition to the YSZ electrolyte material, preliminary work was also done on a novel composite Pt-YSZ anode/cathode material and on representative fuel cell stacks made of this material and a YSZ electrolyte. In both of these preliminary studies, stress evolution with temperature typically reveals a rapid development of compressive stress (due to CTE mismatch) likely combined with plastic yielding. Data suggests that the use of a nominally thick Ti adhesion layer may eliminate the currently unexplainable compressive stress development in Pt-YSZ films, possibly due to a change in microstructure. In these studies, it was found that the final stress state of Pt-YSZ/YSZ/Pt-YSZ stacks may be mildly tensile or compressive.

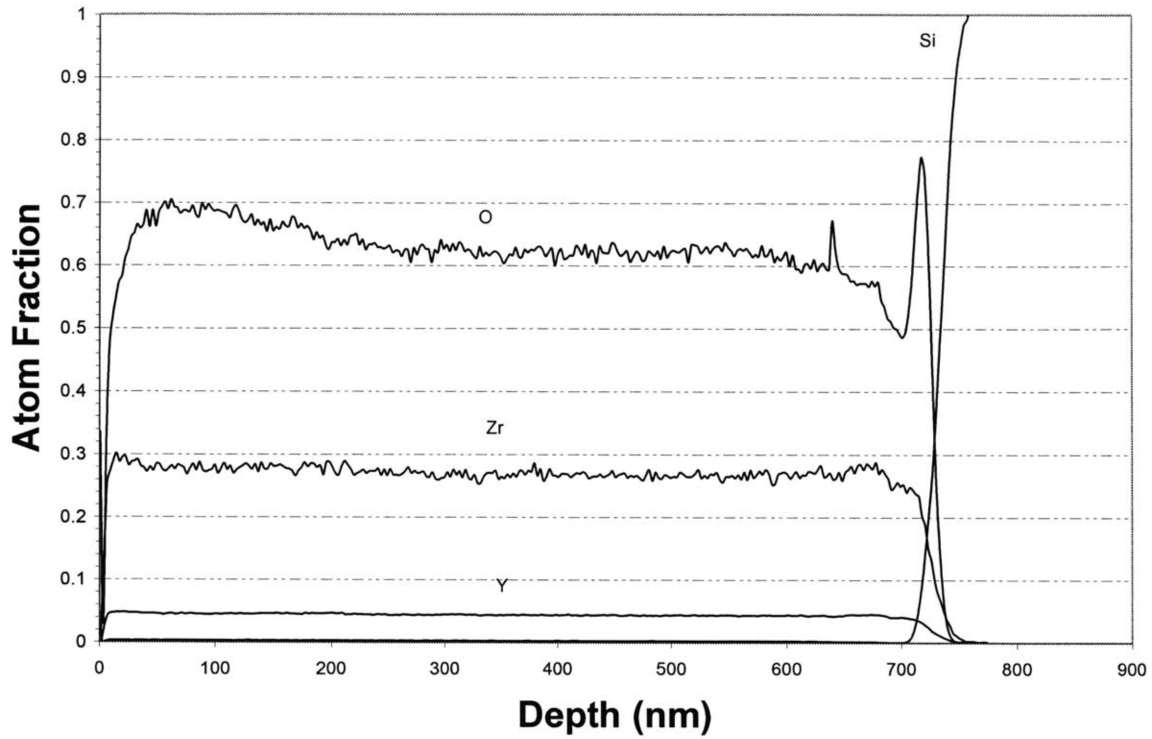

Figure 4-1: Typical SIMS depth profile for room temperature, standard condition, as-deposited YSZ films on Si.

		Atom fractions		
Technique	**Sample**	**O**	**Zr**	**Y**
SIMS	A	63.3	27.2	4.5
	B	64.4	31.7	5.4
	C	65.1	32.2	5.1
	Average	**64.3**	**30.4**	**5.0**
WDS	A	69.5	27.2	3.3
Stoichiometric		66.0	31.0	3.0

Table 4-1: Compositional characterization of YSZ films deposited under standard conditions. Error in SIMS characterization is quoted as ± 10-20%. WDS results provided by J. Hertz [77].

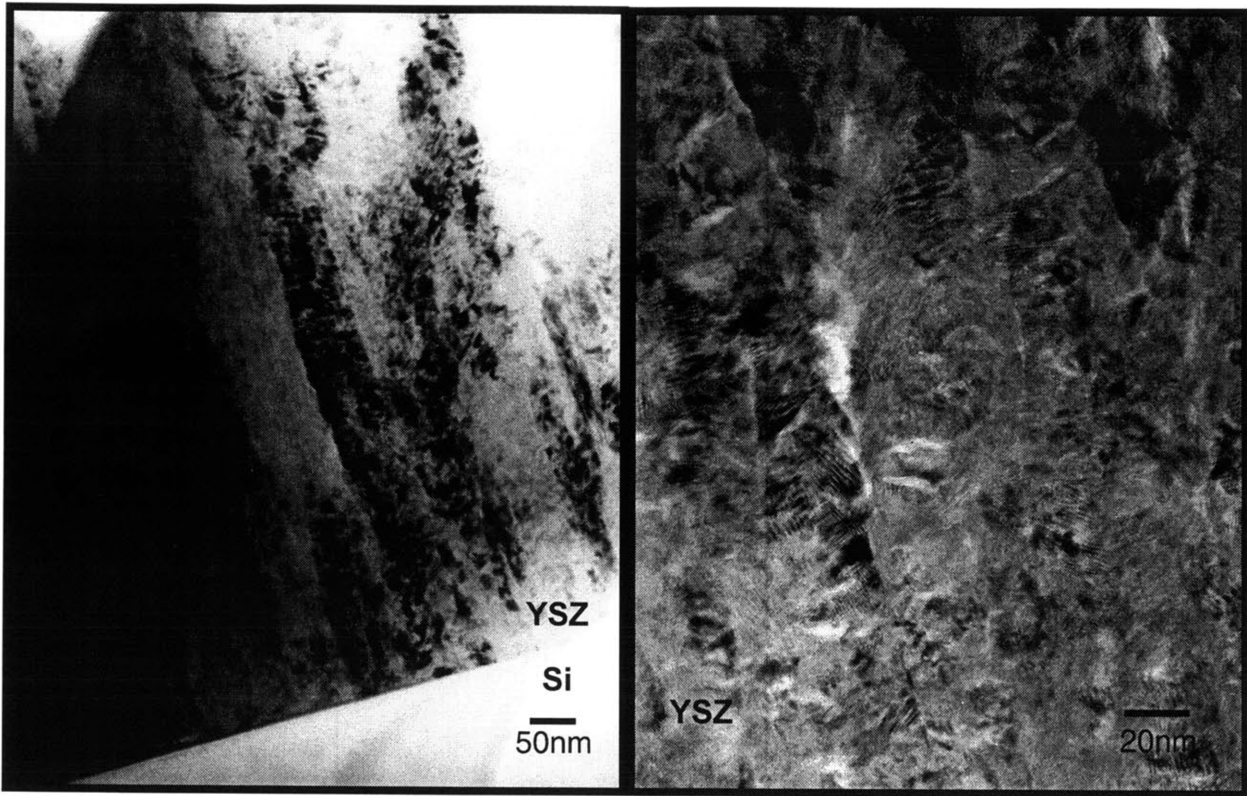

(a) **(b)**

Figure 4-2: TEM images of two different YSZ films deposited under standard conditions. Images indicate columnar growth and slight widening of grains through thickness. Image (b) provided by J. Hertz.

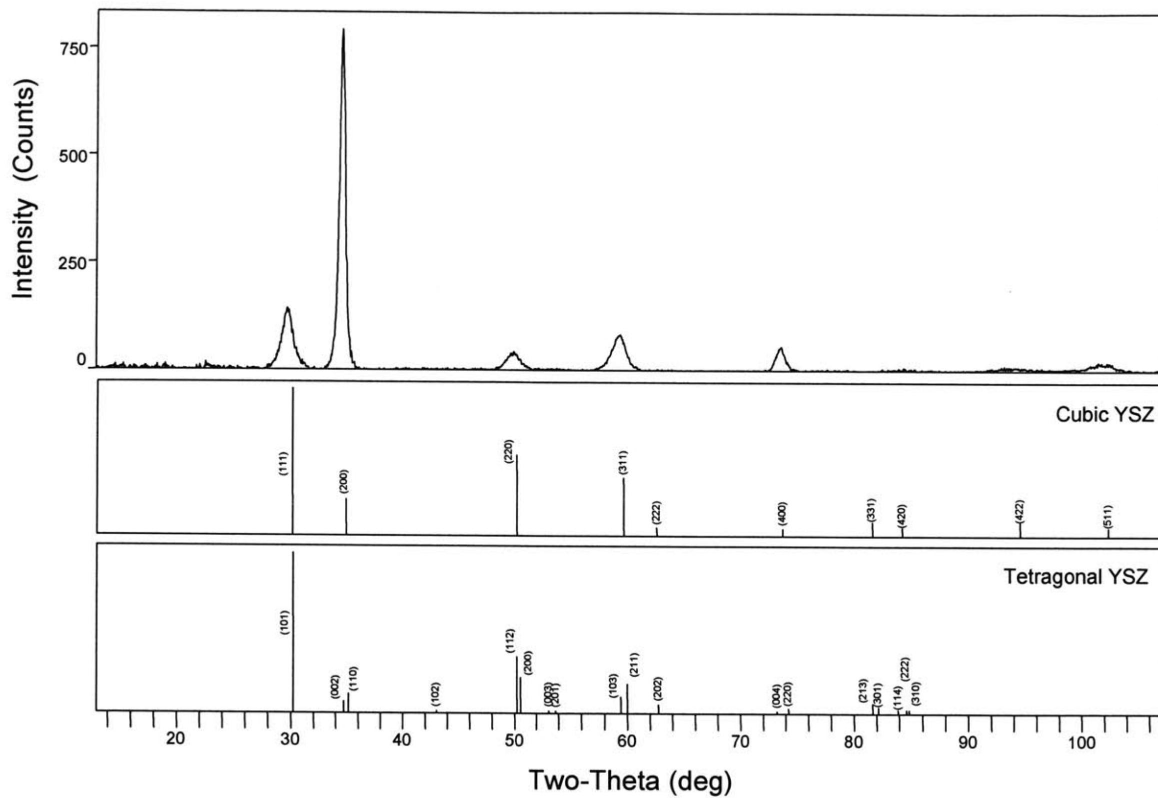

Figure 4-3: X-Ray diffraction profile of YSZ film deposited at room temperature under standard conditions along with peak locations of randomly oriented cubic and tetragonal structures. Peaks indicate purely cubic structure and possible (200) film texture.

	Yttria Stabilized Zirconia (YSZ)	Silicon (100)
Young's Modulus, E	220 GPa	150 GPa
Poisson ratio, ν	0.315	0.17
Biaxial modulus ($E/(1-\nu)$)	321 GPa	180.7 GPa
Coefficient of thermal expansion (CTE), α	10×10^{-6} K^{-1} from 298K - 1200K	2.53×10^{-6} K^{-1} @ 298K
		3.57×10^{-6} K^{-1} from 298K - 798K*
		3.93×10^{-6} K^{-1} from 298K - 1000K*
Melting Temperature, T_m	2500°C	1400°C

***Average values calculated using mathematical relationship given in [92].**

Table 4-2: Bulk material properties.

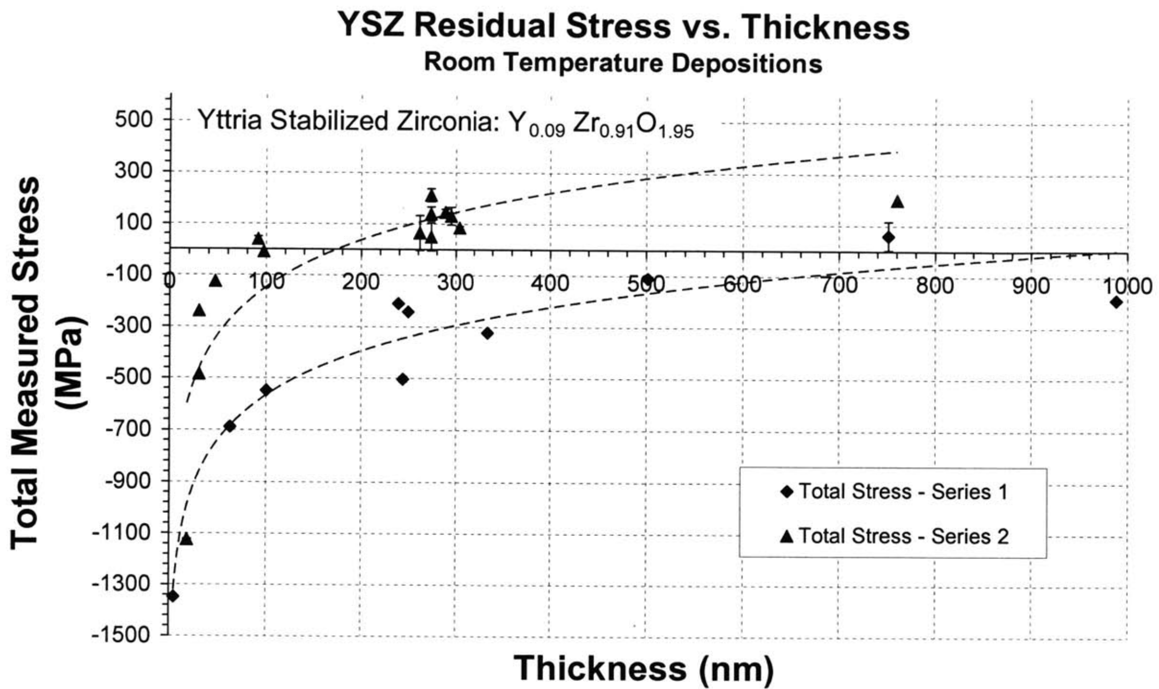

Figure 4-4: Total measured residual stress vs. thickness for room YSZ films deposited at room temperature and standard conditions over two time periods. Error bars indicate estimated uncertainty as discussed in section 3.2.2.

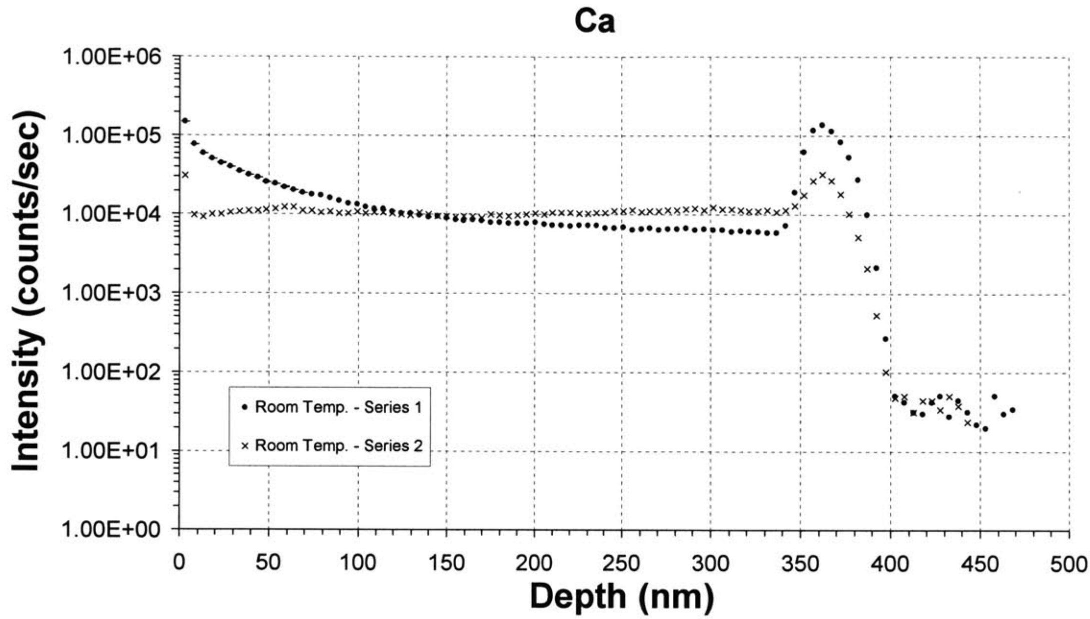

(a)

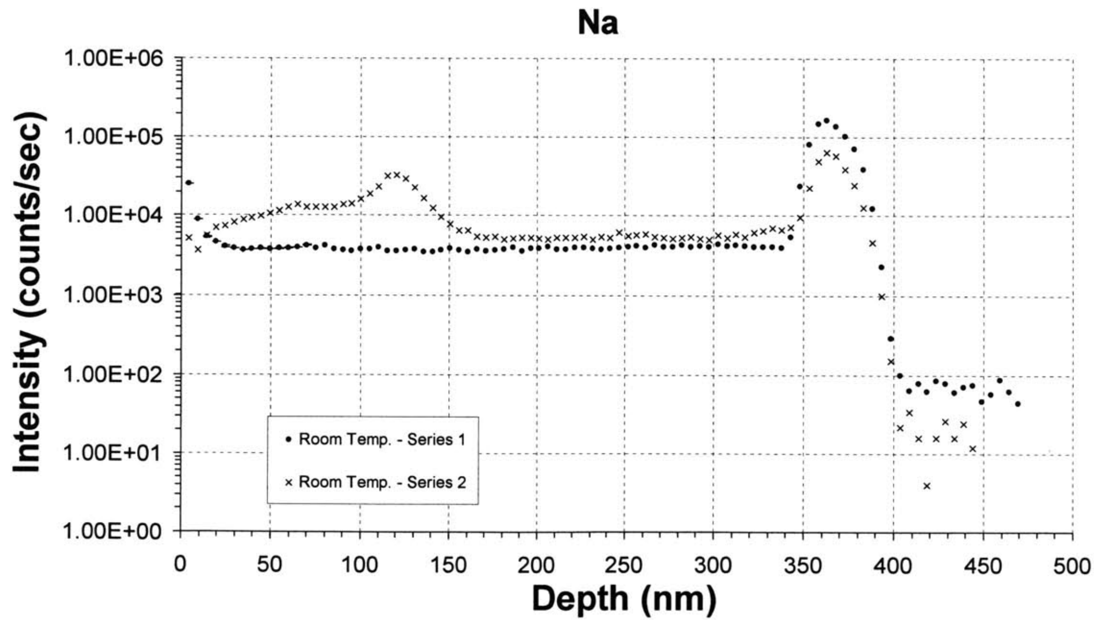

(b)

Figure 4-5: SIMS profiles for trace (a) Ca, (b) Na, (c) Al, and (d) Ti impurities in room-temperature deposited YSZ films over two time periods.

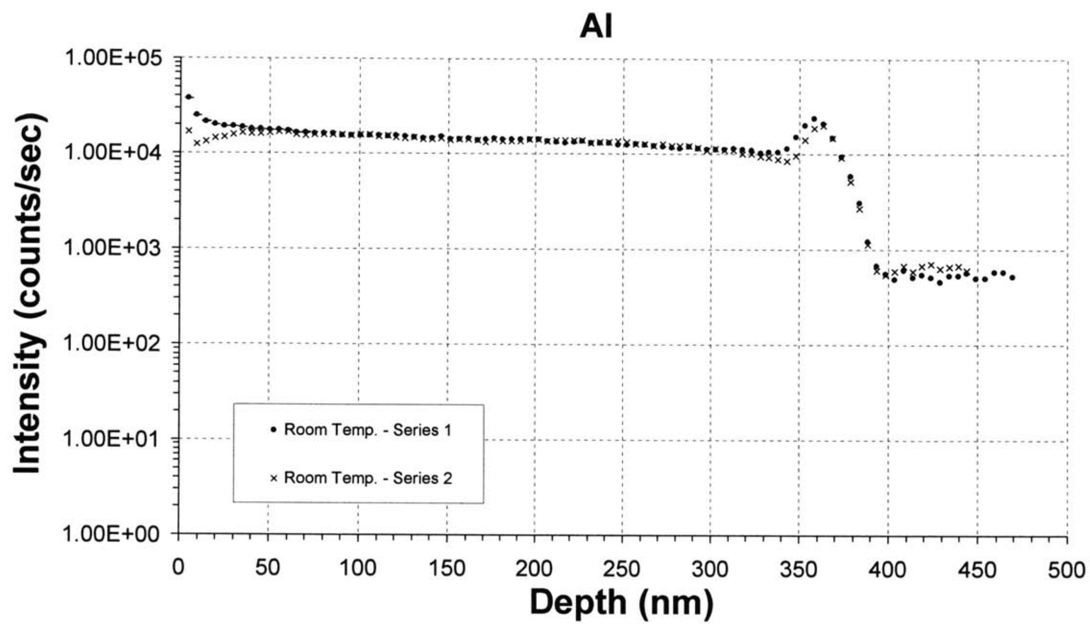

(c)

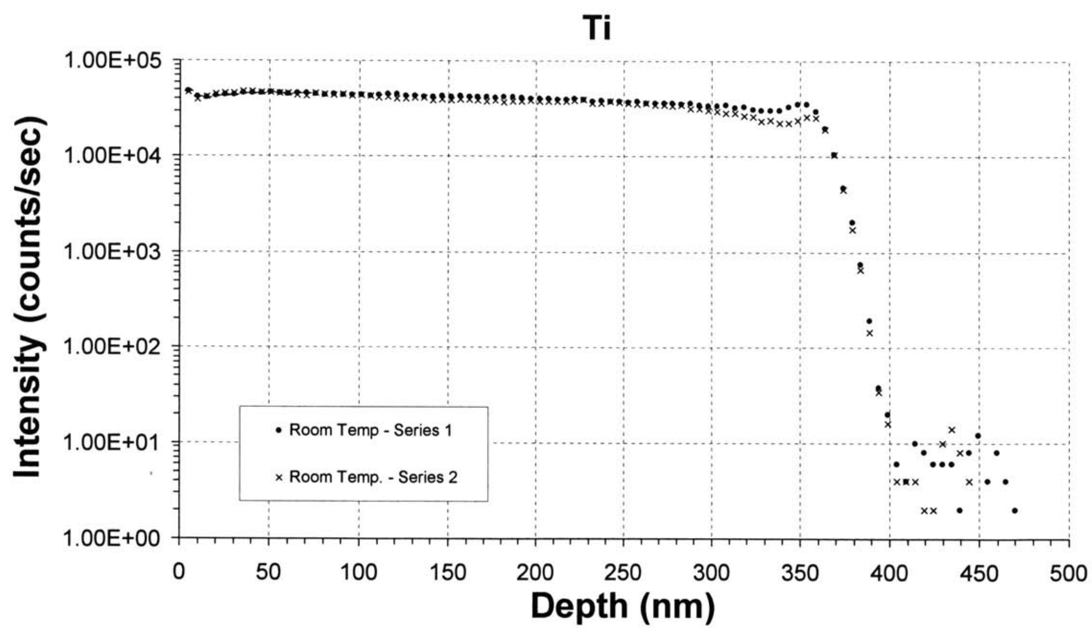

(d)

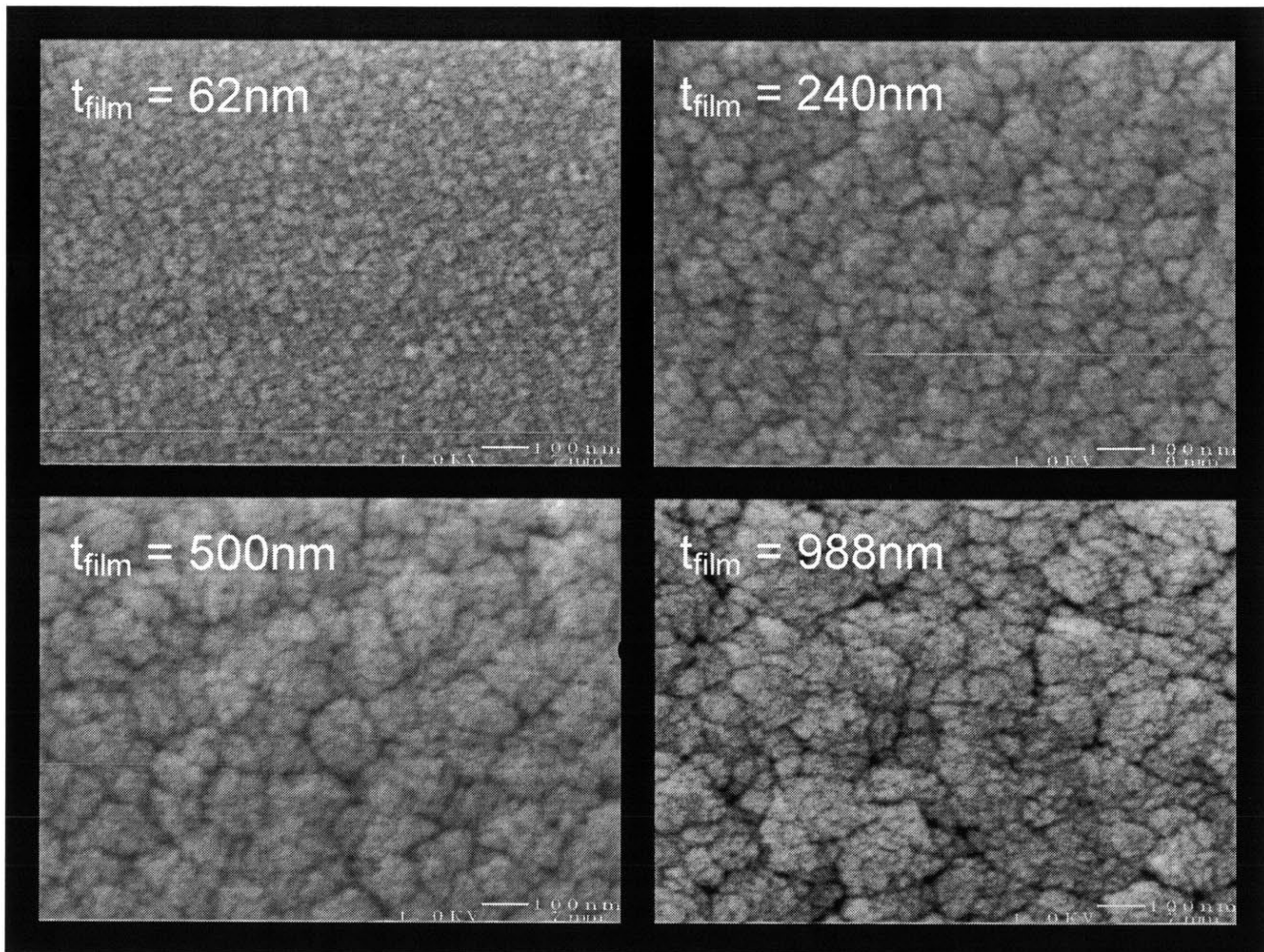

Figure 4-6: Planar view SEM images of room temperature YSZ films deposited at standard conditions of thicknesses of 62nm, 240nm, 500nm and 988nm. Increasing sizes of grain clusters with film thickness, as well as larger individual grains, supports the hypothesis of tensile stress generation mechanisms with increasing film thickness.

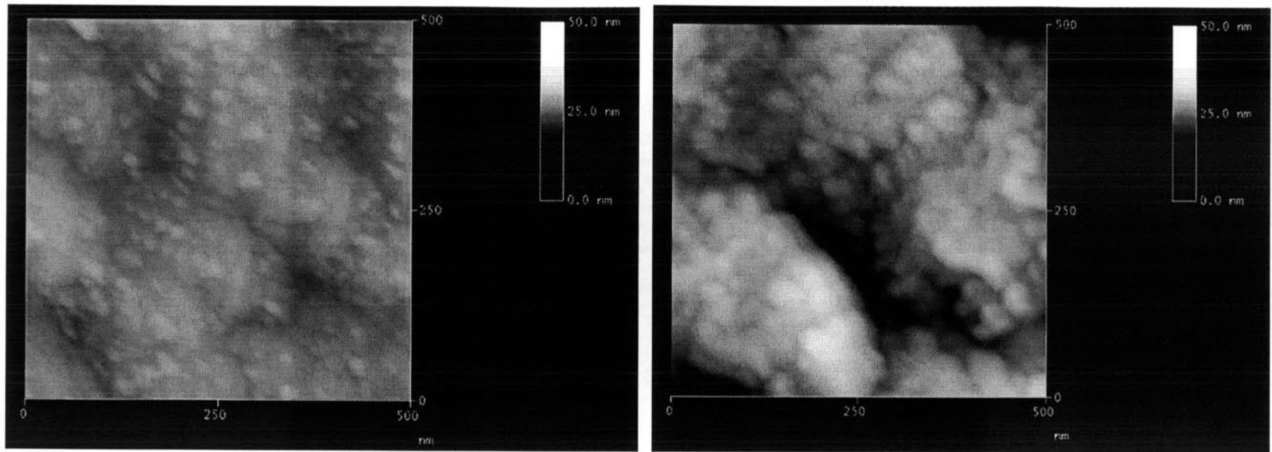

(a) **(b)**

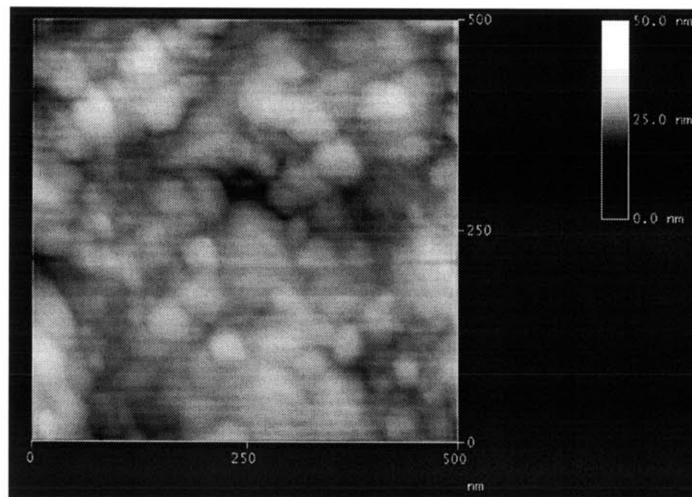

(c)

Figure 4-7: AFM Z-height images of YSZ films deposited under standard conditions with thicknesses of (a) 240nm, (b) 560nm, and (c) 988nm.

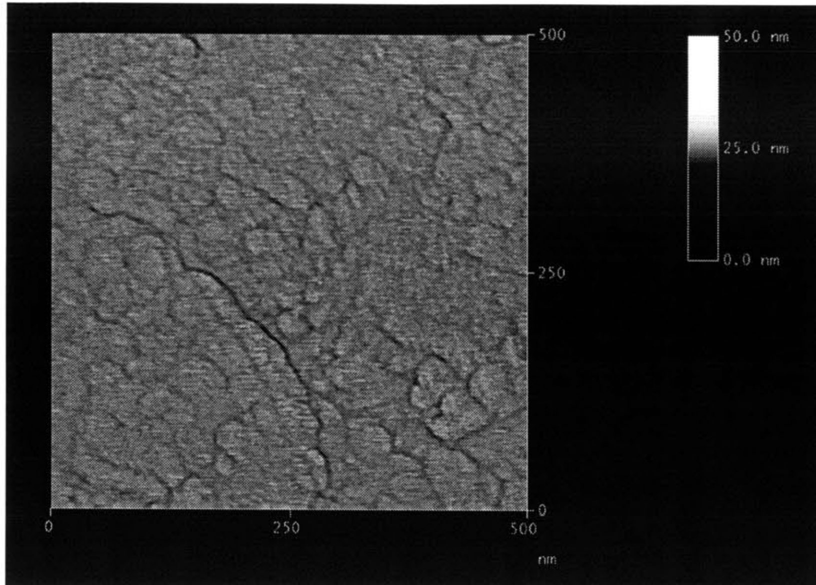

Figure 4-8: AFM image of a 560nm film after applying a high pass filter and flattening routine to accentuate contrast at grain boundaries.

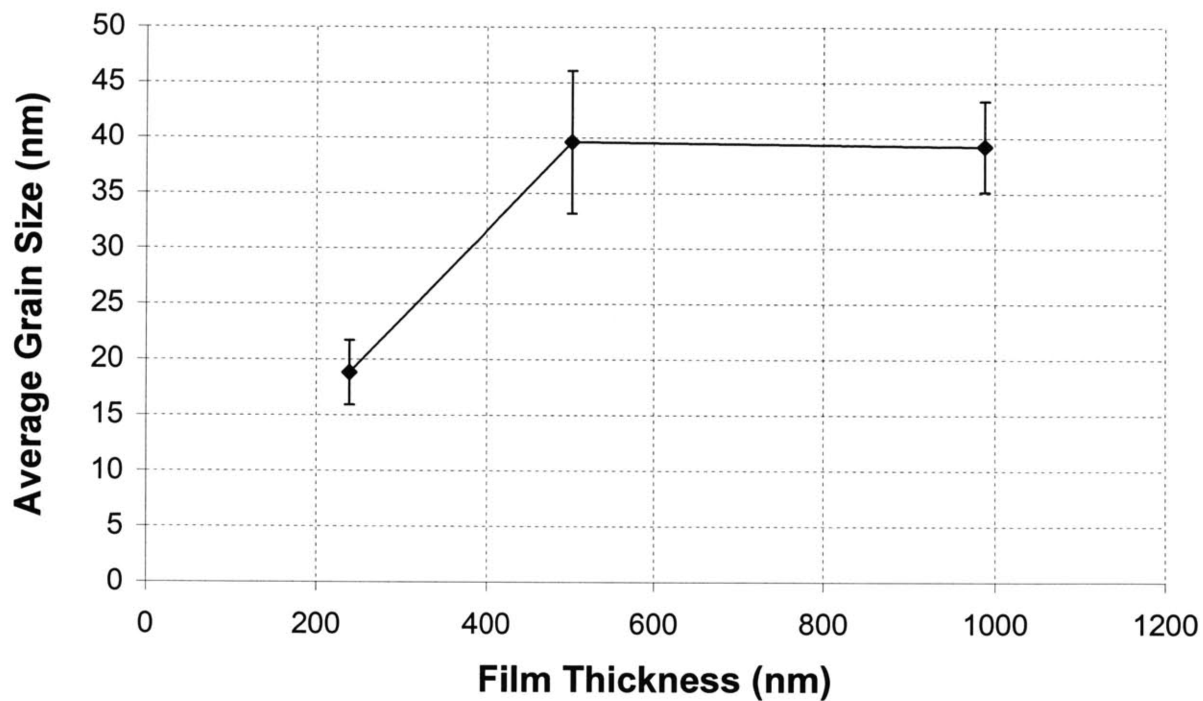

Figure 4-9: Grain size vs. film thickness for room temperature YSZ films deposited under standard conditions as determined by AFM image measurements. Error bars cover ± one standard deviation of a minimum of 7 average measurements.

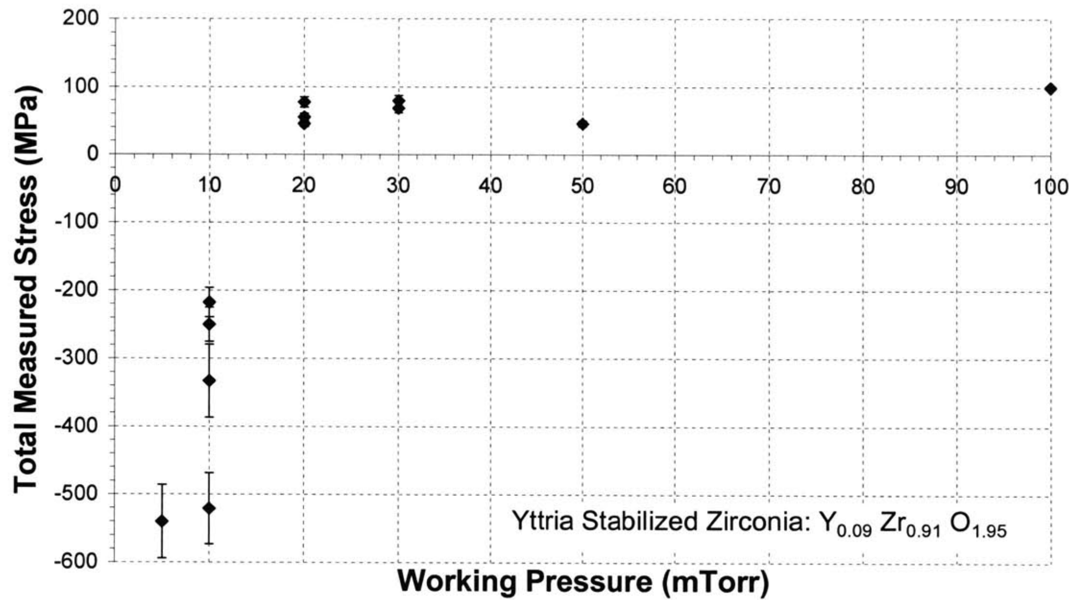

Figure 4-10: Total measured residual stress in YSZ films deposited under varying working pressure but otherwise standard conditions. Error bars indicate estimated uncertainty as discussed in section 3.2.2.

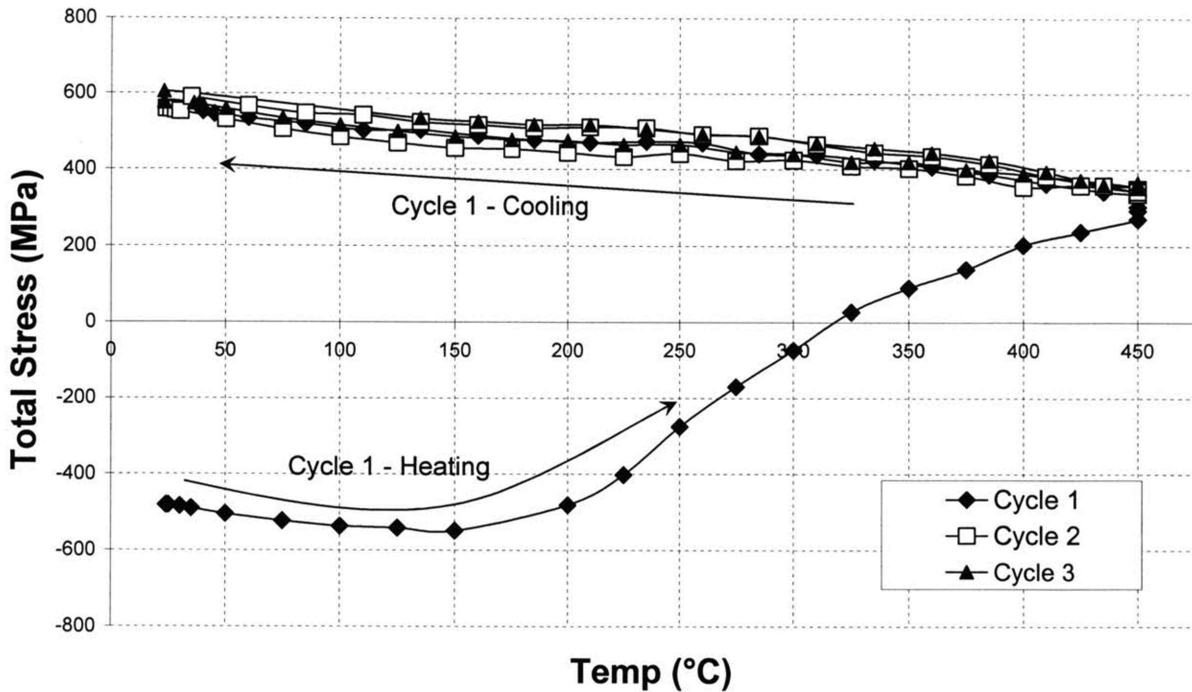

Figure 4-11: Total residual stress vs. temperature during post-deposition thermal cycles for a 241nm thick YSZ film deposited at standard conditions. Data indicates a shift in the intrinsic stress component beginning at approximately 150°C. Stress evolution and hysteresis is typical of all room-temperature deposited samples.

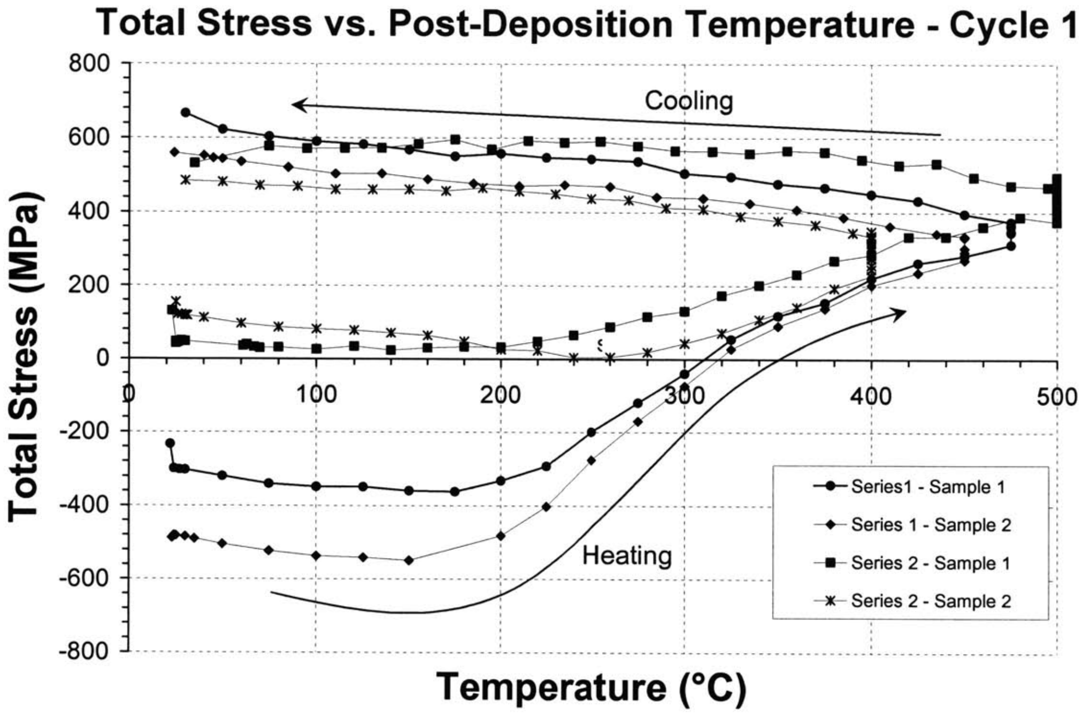

Figure 4-12: Residual stress vs. post deposition temperature for the first temperature cycle of several samples deposited under standard conditions and comparable thicknesses (249-295nm).

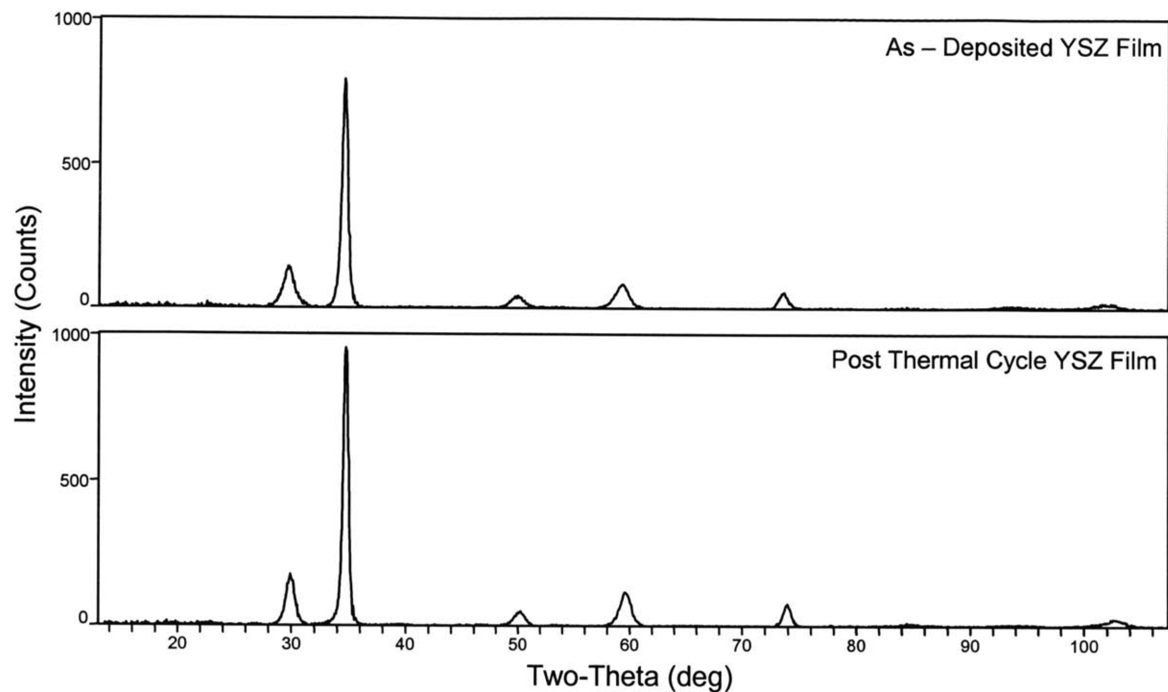

Figure 4-13: XRD profiles of as-deposited (top) and post thermal cycle (bottom) films. Both scans indicate purely cubic phase with slight increases in peak intensities and peak shifting.

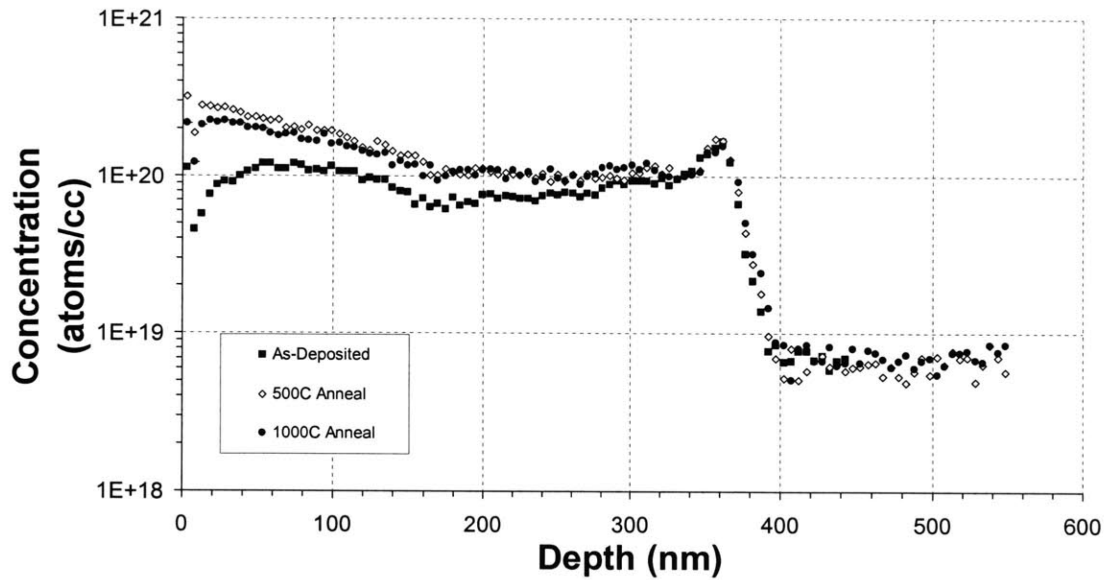

Figure 4-14: SIMS Argon concentration profiles for as deposited, 500°C (1 hr @ 5 °C/min) and 1000°C (4hr @ 10 °C/min) anneals.

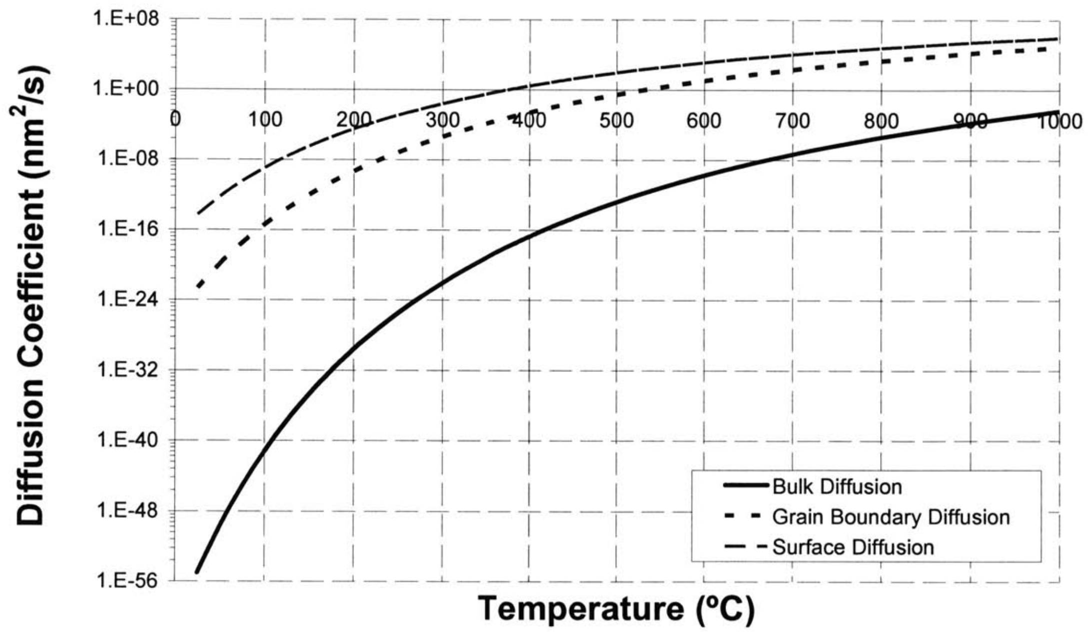

Figure 4-15: Diffusion coefficients for FCC metals given by Ohring [18].

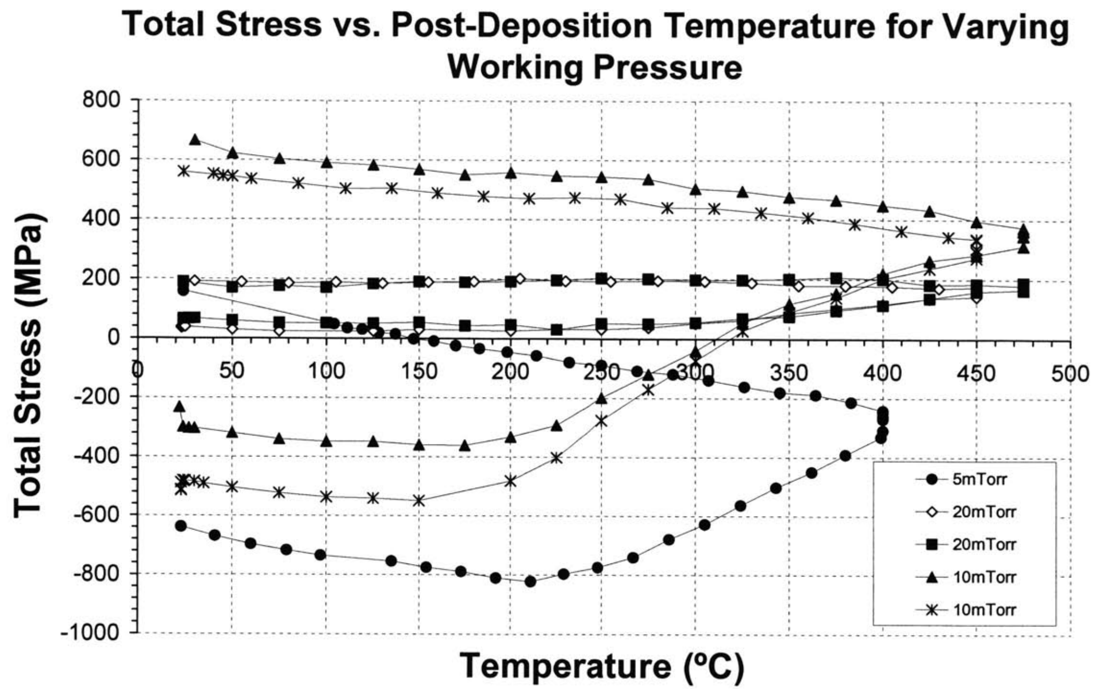

Figure 4-16: Residual stress vs. post deposition pressure for films deposited at room temperature under varying working pressure (film thicknesses within 250nm-350nm, all other conditions standard).

		Atom fractions		
Technique	**Sample**	**O**	**Zr**	**Y**
SIMS	Average Room-temperature depositions	64.3	30.4	5.0
	600°C Deposition	69.0	45.0	6.0
WDS	Room-temperature deposition	69.5	27.2	3.3
	500°C Deposition	69.2	27.2	3.6
Stoichiometric		66.0	31.0	3.0

Table 4-3: Compositional characterization of films deposited at room and elevated substrate temperatures (WDS data provided by J. Hertz).

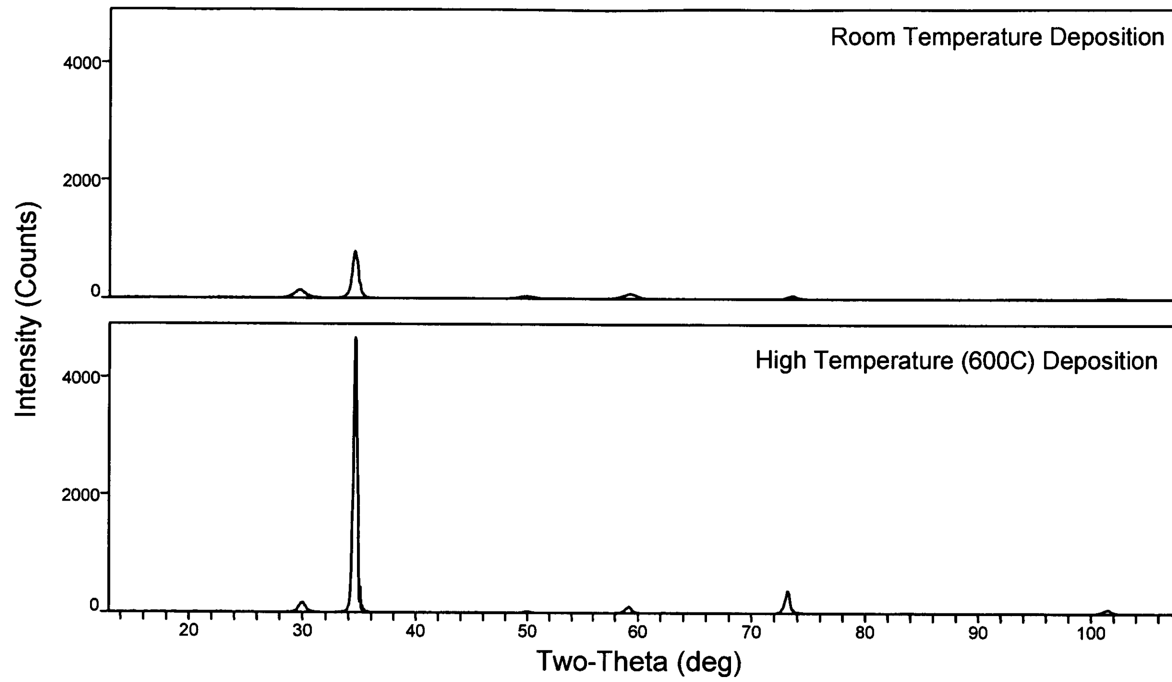

Figure 4-17: XRD profile of films deposited under room temperature (top) and 600°C substrate temperature (bottom).

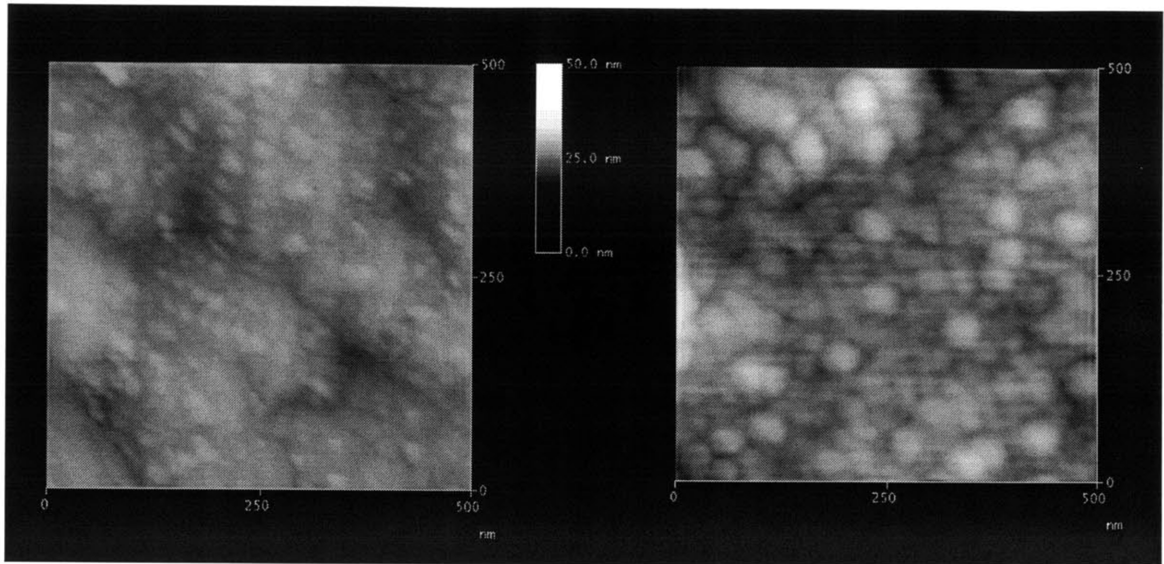

(a) **(b)**

Figure 4-18: AFM images of YSZ films deposited at (a) room temperature and (b) 600°C substrate temperature.

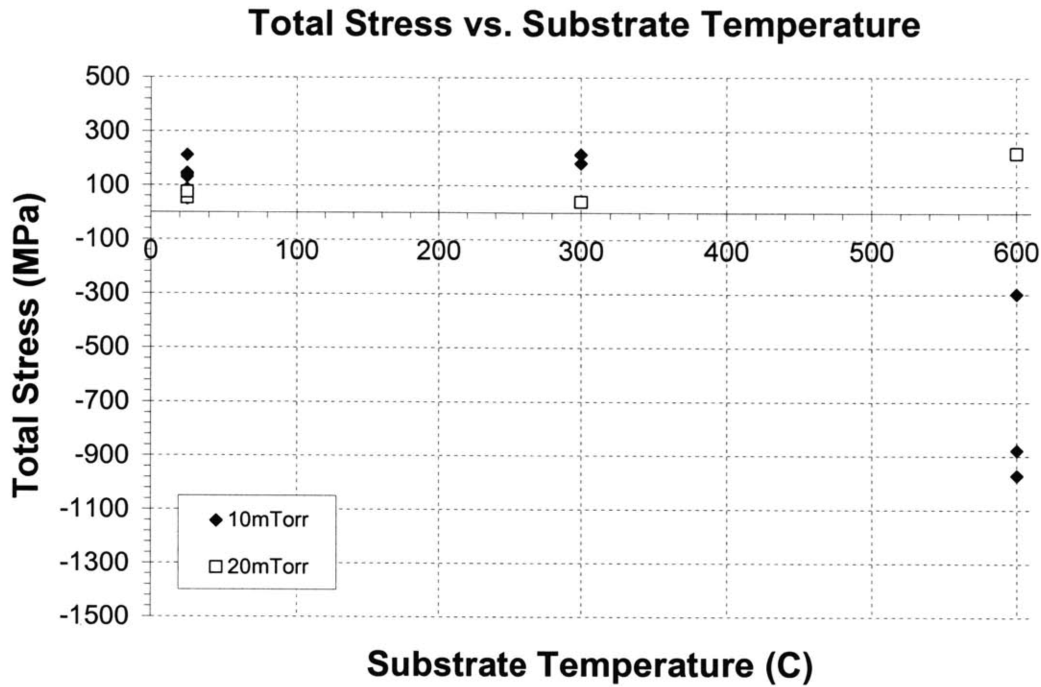

Figure 4-19: Total measured stress vs. substrate temperature for depositions at 10mTorr and 20mTorr working pressures. 20mTorr samples were deposited during the series 1 time period. 10mTorr samples were deposited during the series 2 time period . Film thicknesses are typically between 250nm-350nm. All other conditions are standard.

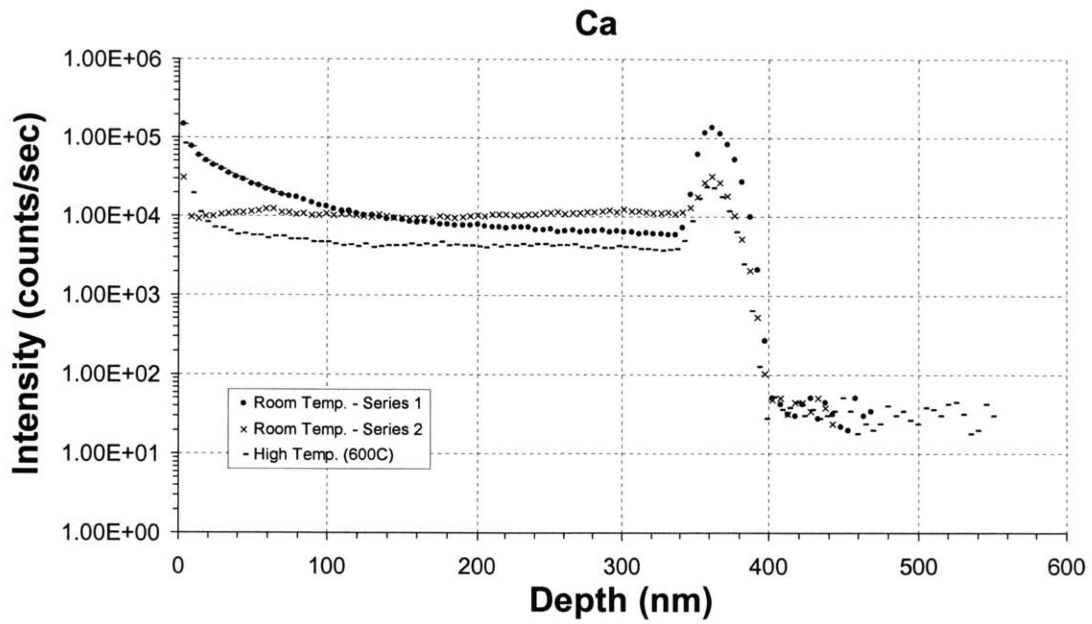

(a)

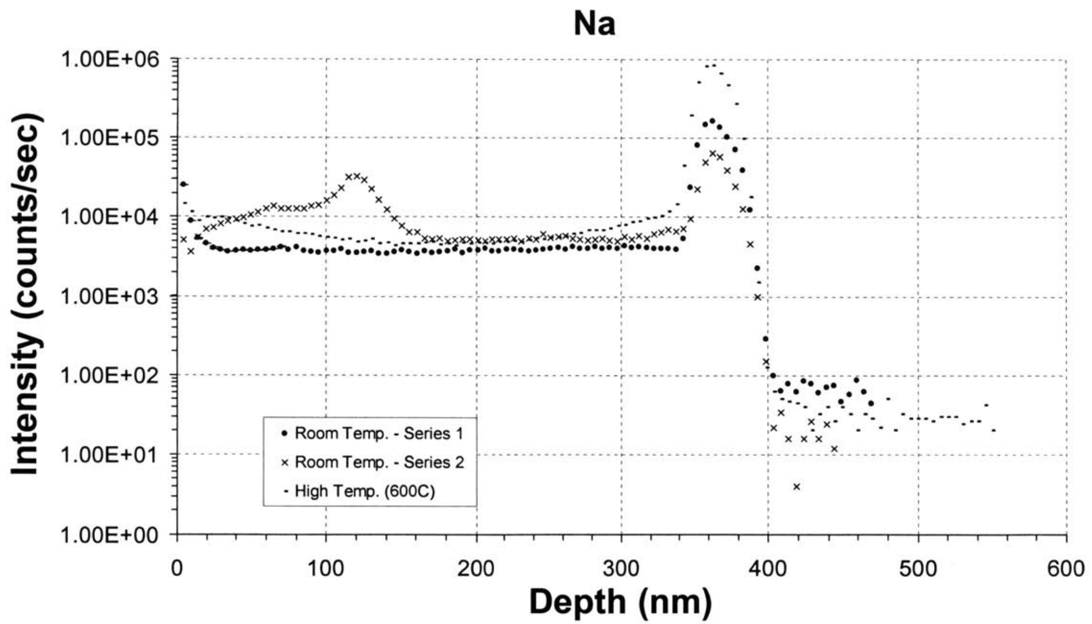

(b)

Figure 4-20: SIMS profiles for trace (a) Ca, (b) Na, (c) Al, and (d) Ti impurities in high-temperature deposited YSZ films.

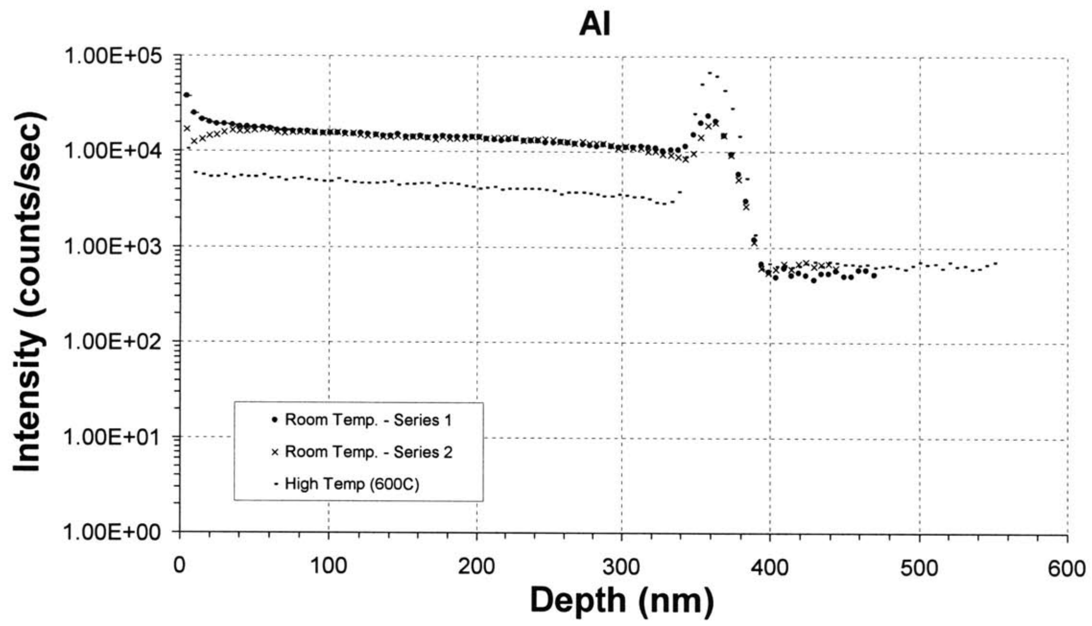

(c)

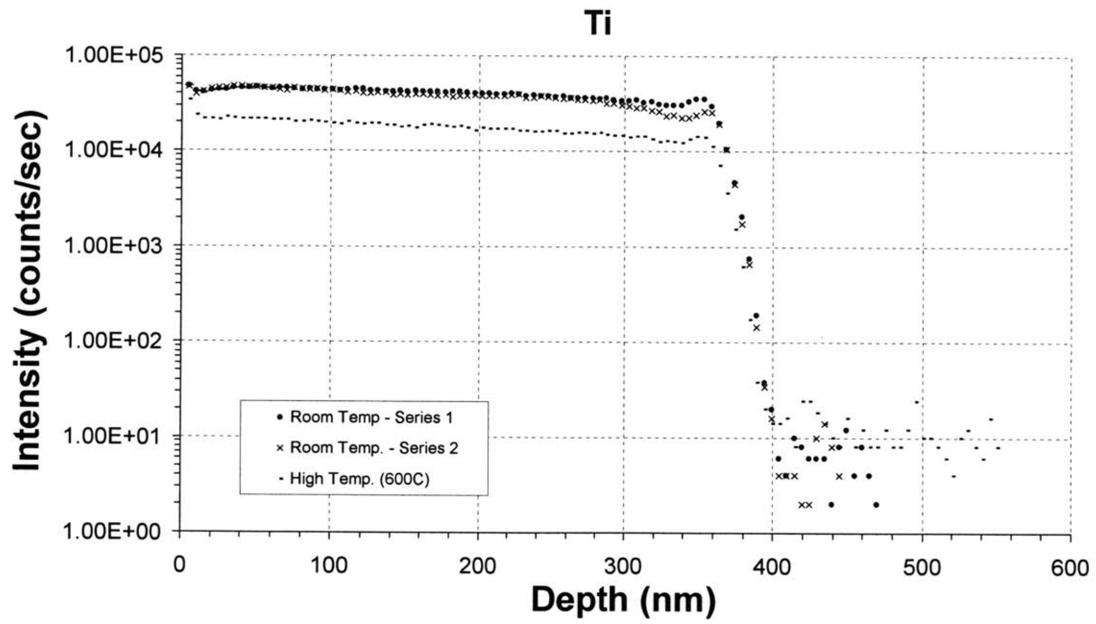

(d)

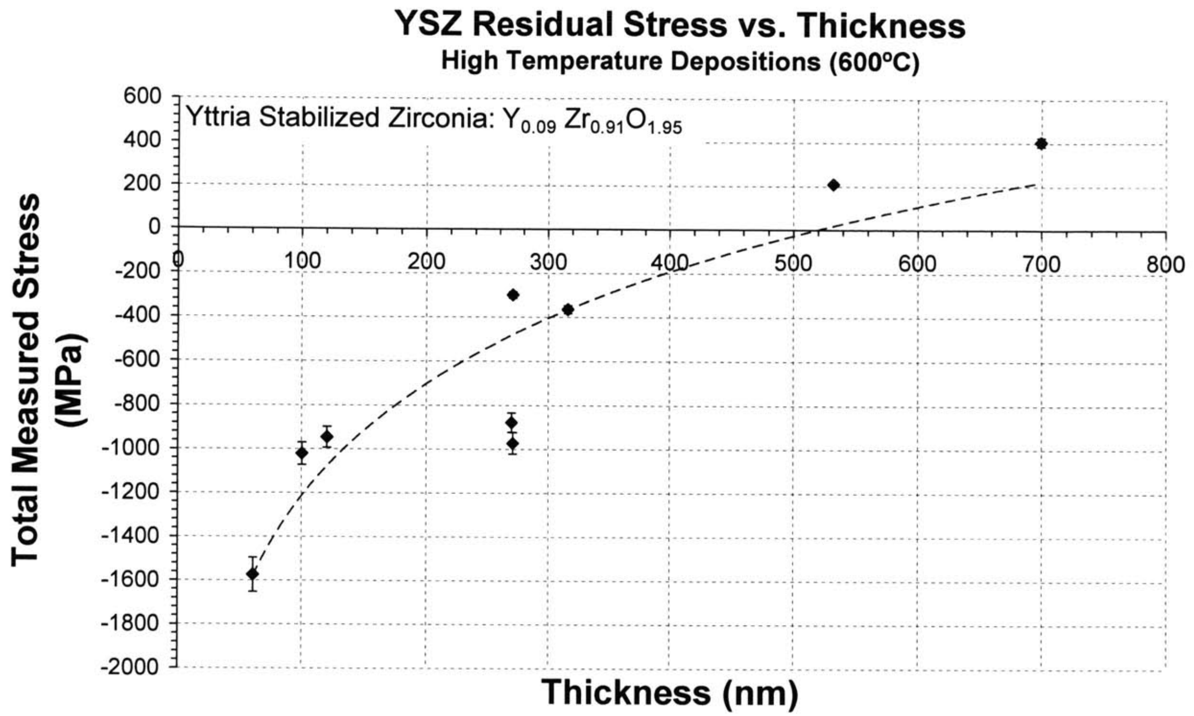

Figure 4-21: Total residual stress versus film thickness in YSZ deposited with a substrate temperature of 600°C.

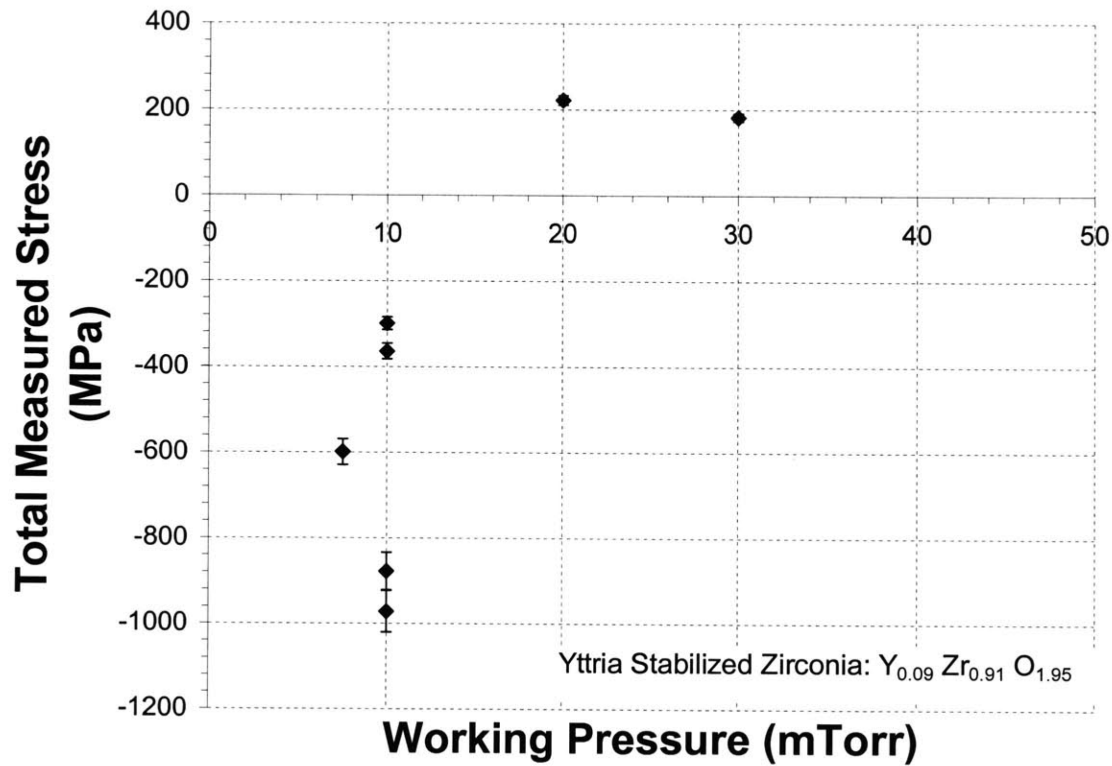

Figure 4-22: Total residual stress versus working pressure of deposition for YSZ films deposited with a substrate temperature of 600°C. Error bars indicate estimated uncertainty as discussed in section 3.2.2.

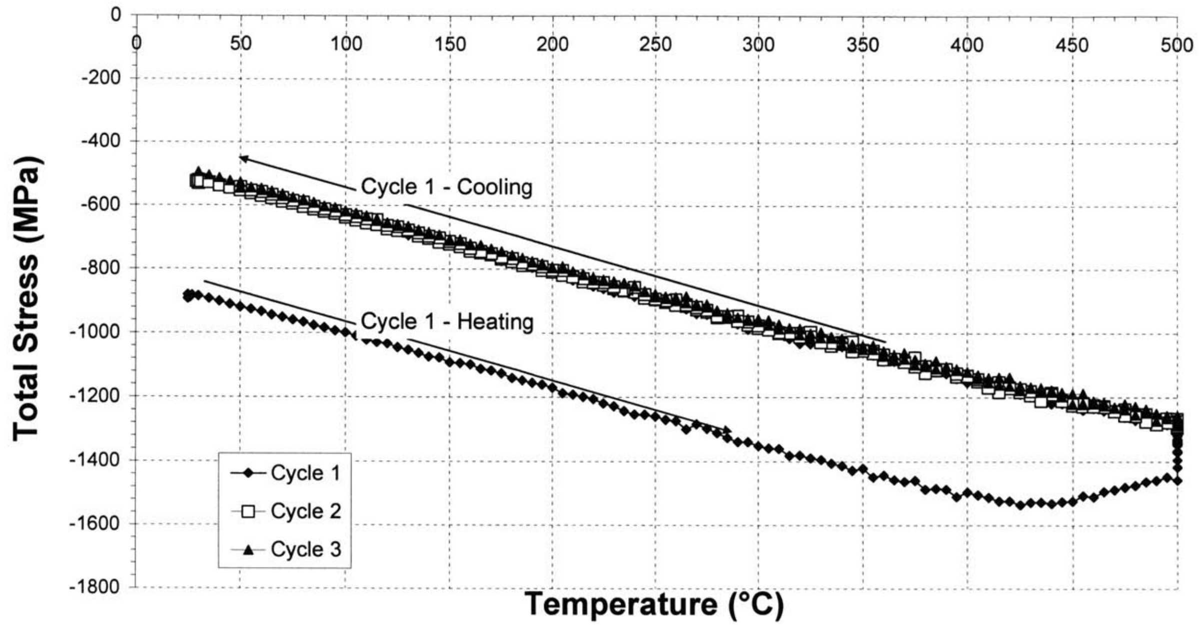

Figure 4-23: Total residual stress vs. post deposition anneal temperature for a high-temperature deposited (600ºC) film.

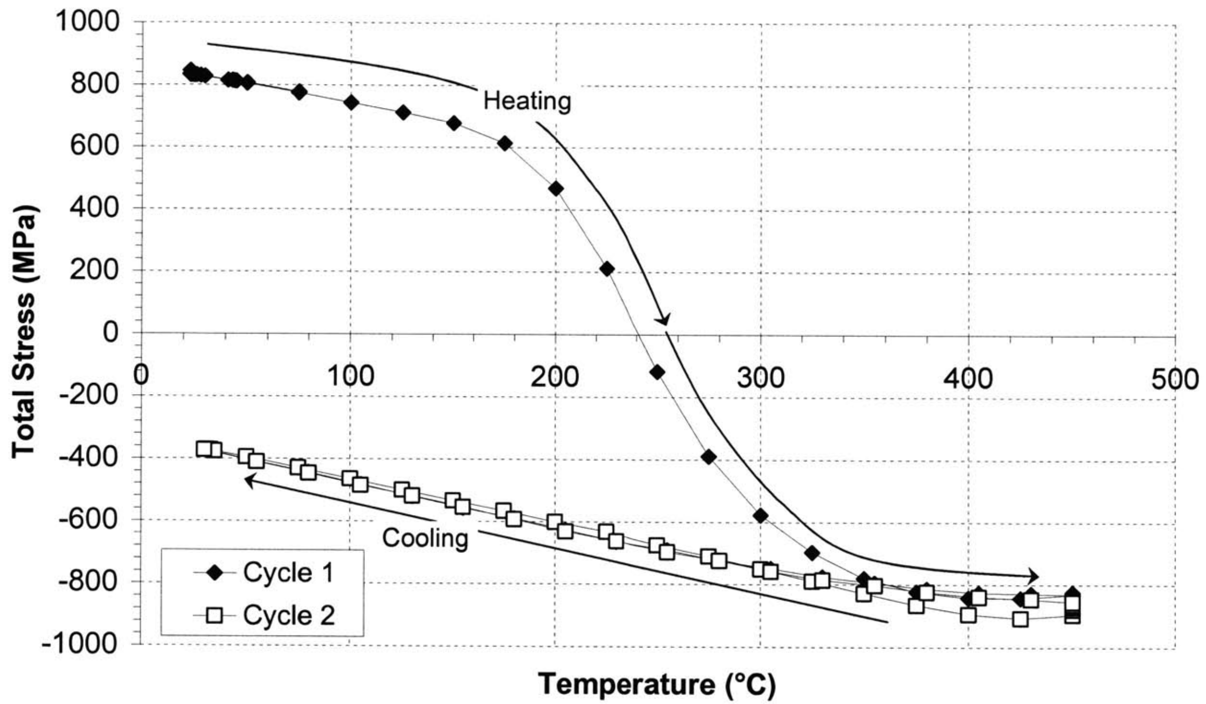

Figure 4-24: Total residual stresss in a co-sputtered Pt-YSZ composite film versus post-deposition temperature.

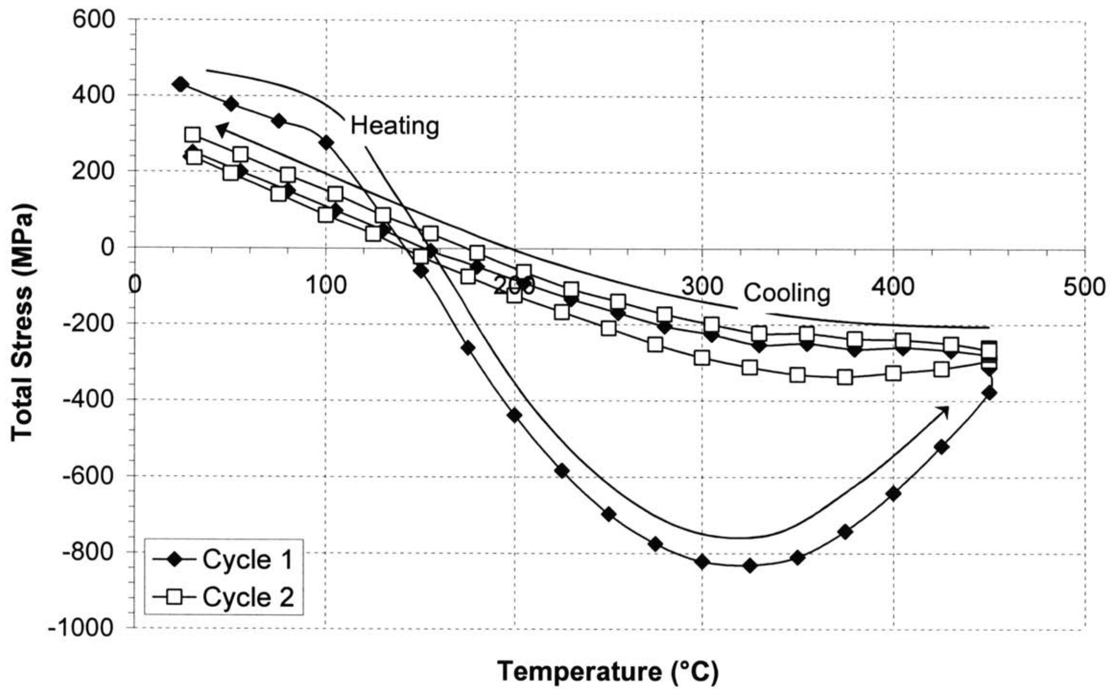

Figure 4-25: Total average residual stress in a trilayer stack of Pt-YSZ/YSZ/Pt-YSZ on Si versus post deposition temperature.

Substrate	Thickness (nm)	Curvature Change (1/m)	Res. Stress by Stoney's Equation (MPa)
Si	6.24	1.66E-04	225.15
SiN/Si	19.49	-1.25E-04	-54.22

Table 4-4: Thickness and stress characteristics of sputtered Ti adhesion layers.

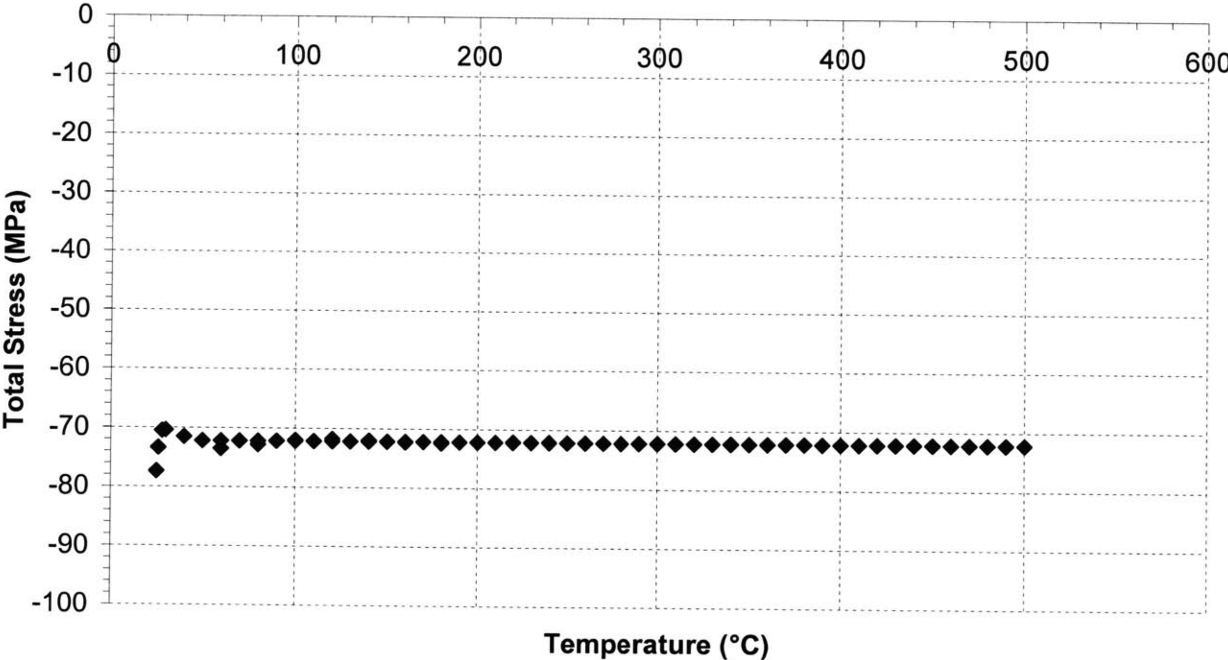

Figure 4-26: Residual stress of 20nm Ti film versus post deposition temperature. Results indicate that the film is not continuous or has delaminated.

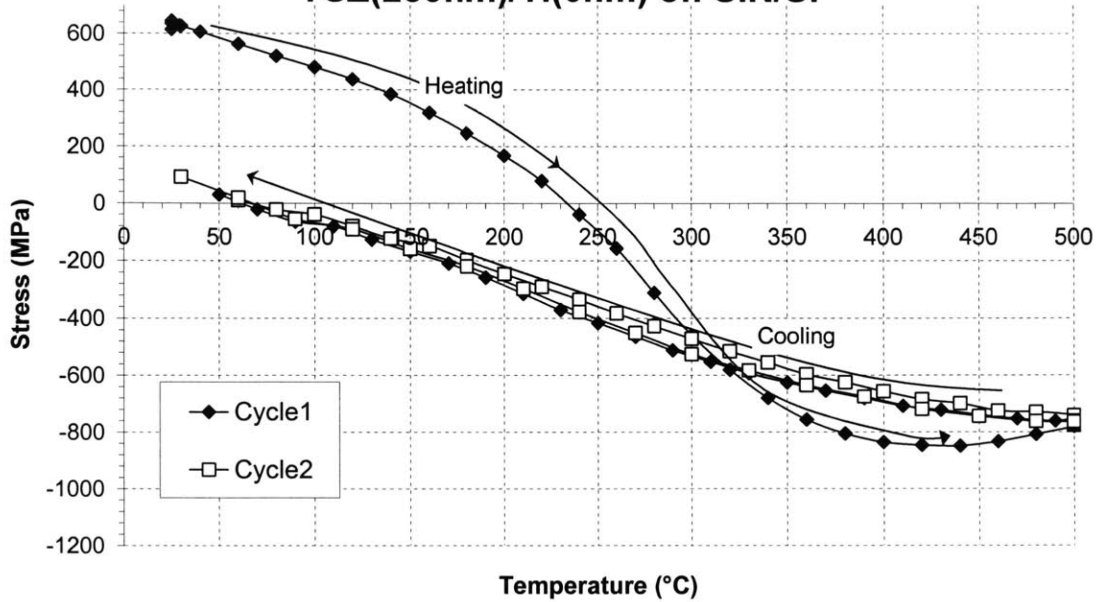

(a)

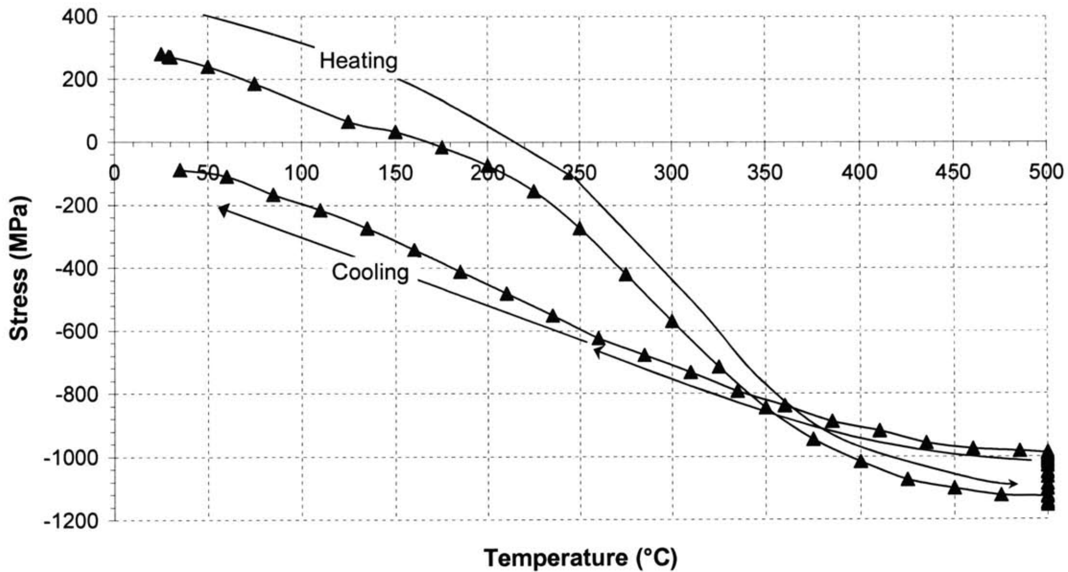

(b)

Figure 4-27: Total average stress of Pt-YSZ/YSZ/Pt-YSZ stacks (layer thickness approximately 250nm each) with Ti a stacks on an Si wafer coated with silicon nitride. Data indicates that the final stress state may be (a) mildly tensile or (b) compressive.

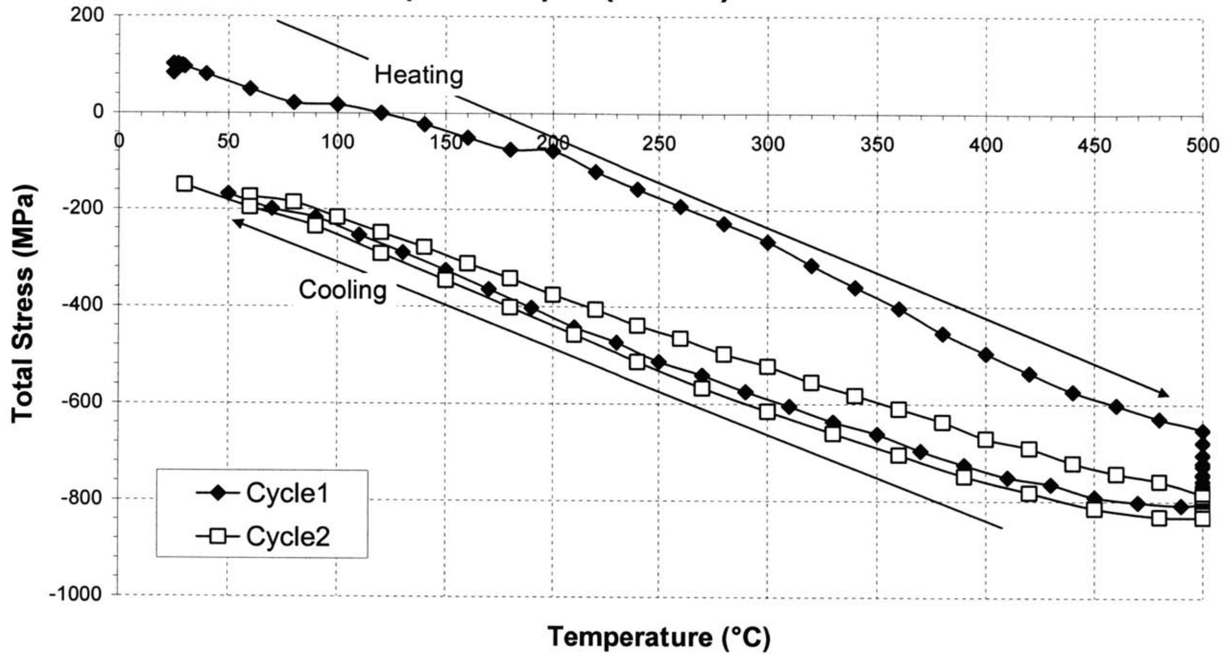

Figure 4-28: Total average residual stress versus post-deposition temperature for a Pt-YSZ/YSZ/Pt-YSZ/Ti stack of increased Ti film thickness deposited on an Si wafer coated with silicon nitride.

Chapter 5: Mechanical Property Characterization of Sputtered YSZ Thin Films

Thermostructural design of multilayered membranes in μSOFCs requires accurate knowledge of the thermo-mechanical properties of the constituent films. As discussed by Spearing, in preliminary design stages, it is generally acceptable to use bulk properties, as has been done thus far in this thesis [93]. However, it is widely recognized that the mechanical properties of a film may vary significantly from its bulk counterparts. This is particularly true for strength properties when the characteristic length scale of the film (generally the film thickness) approaches that of the length scale of the controlling deformation mechanism [94]. Such "size effects" on strength have been confirmed both theoretically and experimentally [95-98]. Further, while it is generally believed that comparably significant variations from the bulk in other mechanical properties, such as Young's modulus, Poisson's ratio and coefficient of thermal expansion (CTE), should not be expected, differences would arise due to the possibility that the density and composition of films can differ from materials in bulk form. Such differences could lead to variations in modulus, CTE, etc. in films versus their bulk counterparts. Furthermore, the presence of microstructural differences in films from their bulk counterparts, such as crystallographic texture, will also lead to changes in fundamental mechanical properties such as Young's modulus. In this chapter, preliminary work investigating the modulus of elasticity and CTE of YSZ films is presented to compliment the residual stress characterization presented in Chapter 4. The first part of this chapter presents a discussion of the influence of crystallographic texture on the mechanical properties of YSZ. This discussion is drawn upon in

the subsequent sections, along with microstructural and residual stress characterization presented in Chapter 4, to evaluate the mechanical properties of sputtered YSZ films. The first part of this discussion (section 5.2) focuses on inferences of mechanical properties taken from the thermal cycling experiments presented earlier. This is followed by results from nanoindentation experiments in section 5.3. In both sets of experimental results, measured properties are linked to likely microstructural characteristics of the films. In addition, experimental limitations are discussed to motivate development of future schemes for mechanical property evaluation.

5.1 Polycrystalline YSZ: Aggregate Mechanical Properties and Influence of Crystallographic Texture

The elastic constants of YSZ crystals are well reviewed and studied by Ingel and Lewis [99, 100] and Kandil *et al.* [101]. Typical elastic stiffness constants for the cubic YSZ system with yttria concentration of 3.9 mol%, comparable to those used in the work presented here, are: c_{11} = 410 GPa, c_{12} = 110 GPa, c_{44} = 55 GPa. Thus, the cubic single crystal stiffness (**C**) and compliance (**S**) matrices are:

$$\mathbf{C} = \begin{pmatrix} c_{11} & c_{12} & c_{12} & 0 & 0 & 0 \\ c_{12} & c_{11} & c_{12} & 0 & 0 & 0 \\ c_{12} & c_{12} & c_{11} & 0 & 0 & 0 \\ 0 & 0 & 0 & c_{44} & 0 & 0 \\ 0 & 0 & 0 & 0 & c_{44} & 0 \\ 0 & 0 & 0 & 0 & 0 & c_{44} \end{pmatrix} = \begin{pmatrix} 410 & 110 & 110 & 0 & 0 & 0 \\ 110 & 410 & 110 & 0 & 0 & 0 \\ 110 & 110 & 410 & 0 & 0 & 0 \\ 0 & 0 & 0 & 55 & 0 & 0 \\ 0 & 0 & 0 & 0 & 55 & 0 \\ 0 & 0 & 0 & 0 & 0 & 55 \end{pmatrix} GPa \qquad (5\text{-}1)$$

$$\mathbf{S}=\mathbf{C}^{-1}=\begin{pmatrix} s_{11} & s_{12} & s_{12} & 0 & 0 & 0 \\ s_{12} & s_{11} & s_{12} & 0 & 0 & 0 \\ s_{12} & s_{12} & s_{11} & 0 & 0 & 0 \\ 0 & 0 & 0 & s_{44} & 0 & 0 \\ 0 & 0 & 0 & 0 & s_{44} & 0 \\ 0 & 0 & 0 & 0 & 0 & s_{44} \end{pmatrix}=\begin{pmatrix} 27.5 & -5.82 & -5.82 & 0 & 0 & 0 \\ -5.82 & 27.5 & -5.82 & 0 & 0 & 0 \\ -5.82 & -5.82 & 27.5 & 0 & 0 & 0 \\ 0 & 0 & 0 & 180 & 0 & 0 \\ 0 & 0 & 0 & 0 & 180 & 0 \\ 0 & 0 & 0 & 0 & 0 & 180 \end{pmatrix} 10^{-4}\frac{1}{GPa} \quad (5\text{-}2)$$

From these elastic constants, several insights can be drawn regarding the expected properties of a YSZ film both with and without texture. First, the randomly oriented, fully crystallized, polycrystalline, isotropic Young's modulus (E) and Poisson's ratio (ν) will lie between the Reuss (R) and Voight (V) estimates, as presented by Hill [102]. Those bounds are defined by:

$$\nu_{R,V}=\frac{1}{2}\left(1-\frac{3G_{R,V}}{3K_{R,V}+G_{R,V}}\right) \quad (5\text{-}3)$$

$$E_{R,V}=\frac{1}{\dfrac{1}{3G_{R,V}}+\dfrac{1}{9K_{R,V}}} \quad (5\text{-}4)$$

Where, for a cubic material, the quantities G_R, G_V, K_R, and K_V are given by:

$$K_R=K_V=\frac{1}{3}(c_{11}+2c_{12}) \quad (5\text{-}5)$$

$$G_V=\frac{(c_{11}-c_{12})+3c_{44}}{5} \quad (5\text{-}6)$$

$$G_R=\frac{5}{4(s_{11}-s_{12})+3s_{44}} \quad (5\text{-}7)$$

Using eqs. (5-1) and (5-2) in eqs. (5-3) through (5-7) gives $\nu_R = 0.343$, $\nu_V = 0.307$, $E_R = 197.8$ GPa, $E_V = 243.1$ GPa. Appropriate combinations of these bounds indicate that the biaxial modulus ($E/(1+\nu)$) of a randomly oriented YSZ polycrystalline material may range from 285

GPa – 370 GPa. This compares well with the biaxial modulus of 321GPa presented in Chapter 4 using typically quoted bulk material properties.

The properties of the YSZ films produced in this work may also be significantly affected by the presence of crystallographic texture. As presented in Chapter 4, it is believed that the YSZ films produced in this work possess some degree of (100) texture (*i.e.,* crystals with their [100] directions normal to the film surface) with random in-plane orientation. Establishing the influence of this texture on mechanical properties due to loadings normal and parallel to the film surface is of interest for the design of structures comprised of YSZ films. For clarity, a (100) textured crystal indicating the other critical directions in this discussion is shown in Figure 5-1.

The variation of modulus and Poisson's ratio within textured single crystals is discussed in detail by Nye [103] and examined specifically for YSZ by Ingel [99]. Directions in a cubic material are typically defined by (l_1, l_2, l_3) where $l_{1,2,3}$ are the direction cosines referred to the [100], [010], and [001] directions, respectively. Transforming the fourth order compliance tensor ($\mathbf{S} = S_{ijkl}$) such that the axis aligned with the [100] crystal direction is now aligned with the direction of interest allows Young's modulus for the given direction to be determined by $E = 1/s_{11}'$, where s_{11}' is the s_{1111}' element of the transformed compliance tensor written in the standard contracted form given by Nye [103]. In general, Young's modulus for a given direction (l_1, l_2, l_3) can be determined by:

$$\frac{1}{E} = s_{11}{}' = s_{11} - 2(s_{11} - s_{12} - \frac{1}{2}s_{44})(l_1{}^2 l_2{}^2 + l_2{}^2 l_3{}^2 + l_1{}^2 l_3{}^2) \qquad (5\text{-}8)$$

Similarly, Poisson's ratio is generally defined as $\nu = -s_{12}'/s_{11}'$ and it can be shown that for cubic crystals subject to stress in the (l_1,l_2,l_3) direction giving rise to strain in a transverse direction (m_1,m_2,m_3), Poisson's ratio can be determined by:

$$\nu = -\frac{s_{12} + \left(s_{11} - s_{12} - \frac{1}{2}s_{44}\right)\left(l_1^2 m_1^2 + l_2^2 m_2^2 + l_3^2 m_3^2\right)}{s_{11} - 2\left(s_{11} - s_{12} - \frac{1}{2}s_{44}\right)\left(l_1^2 l_2^2 + l_2^2 l_3^2 + l_1^2 l_3^2\right)} \qquad (5\text{-}9)$$

From expressions (5-8) and (5-9), Young's modulus and Poisson's ratio in the [100] direction can be determined by letting $(l_1,l_2,l_3) = (1,0,0)$ and $(m_1,m_2,m_3) = (0,\cos(\theta), \sin(\theta))$ where θ is the angle in the (100) plane measured from the [010] direction. Applying these directions in eqs. (5-8) and (5-9) and integrating from $\theta = 0$ to 2π for the average Poission's ratio gives $E_{[100]} = 363.4$ GPa and $\nu_{[100]avg} = 0.212$ for a fully (100) textured YSZ film with random in-plane orientation.

Texture will also result in variations in mechanical properties in the plane of a film. For the work done here, the primary property of interest is the biaxial modulus in the plane of the film: $E/(1-\nu)$. In general, the biaxial modulus in a particular plane could be determined using eqs. (5-8) and (5-9). However, it is convenient for this work that for any cubic single crystal material of (100) texture, the biaxial modulus in the (100) plane is independent of direction and given by the relationship [103, 104]:

$$\left(\frac{E}{1-\nu}\right)_{(100)} = \left[\frac{1}{s_{11} + s_{12}}\right] = \left[c_{11} + c_{12} - \frac{2c_{12}^2}{c_{11}}\right] \qquad (5\text{-}10)$$

Using the values given in eq. (5-1) gives a biaxial modulus of 461 GPa for a single crystal (100) fully textured YSZ material. This may be considered an upper bound on the biaxial modulus of a polycrystalline film of (100) texture with random in-plane orientation, as is the case with the films prepared in this work. The remaining sections of this chapter will use these

bounds on material properties for randomly oriented and textured films to provide insight into experimental data.

5.2 Mechanical Property Estimates Based on Thermal Cycling Data

Thermal cycling data presented in Chapter 4 may be used to infer mechanical properties of the deposited YSZ films. Specifically, this data has been used to consider the product of biaxial modulus and coefficient of thermal expansion (CTE) as well as the ultimate tensile strength of the film.

5.2.1 Biaxial Modulus and Coefficient of Thermal Expansion (CTE)

It has been established that the total (*i.e.*, measured) residual stress is a result of two components: extrinsic and intrinsic. In the thermal cycling data presented previously in Chapter 4, the extrinsic stress present is due to CTE mismatch between the YSZ film and substrate. Therefore, the total residual stress presented previously can be taken as:

$$\sigma_{tot} = \sigma_{thermal} + \sigma_{intrinsic} = \frac{E_f}{(1-\nu_f)}(\alpha_s - \alpha_f)(T - T_o) + \sigma_{intrinsic} \qquad (5\text{-}11)$$

From this, assuming no variation in intrinsic stress with temperature and taking into account any variation of modulus and CTE of the film and substrate with temperature, one can see that the slope (m) of the total stress versus temperature plots presented previously is representative of the product of the film biaxial modulus and difference in CTE between the substrate and film:

$$m = \frac{E_f}{(1-\nu_f)}(\alpha_s - \alpha_f) \qquad (5\text{-}12)$$

It is reasonable to assume that the single crystal Si substrate properties are close to those presented in Chapter 4 and do not vary from sample to sample. Therefore, differences between the slope expected for a film with bulk material properties and observed slopes of the stress vs.

temperature curves are due to differences between the bulk and observed film biaxial modulus and/or CTE. Similarly, variations of slopes among films deposited under different conditions are also considered to be indicative of variations in film mechanical properties. Again noting that the use of this relationship in equation (5-12) assumes that the intrinsic stress component does not vary with temperature. The subsequent discussion accounts for this in only applying eq. (5-12) in those regions of the stress-temperature behavior where the intrinsic stress does not appear to change (*i.e.,* linear portions of the curves with no hysteresis).

Linear least-squares fits were used to determine the slope of the initial heating (*i.e.*, before the onset of stress hysteresis) and full cooling portions of the first thermal cycle as well as the heating and cooling portions of subsequent cycles. These are compared to the expected value based on bulk properties. In determining this expected value, the temperature dependence of the CTE of silicon, as given in [92], and the Young's modulus of YSZ, as presented in [101], are taken into account. The average theoretical slope from 20°C – 200°C is 2.26 MPa/°C. Expected versus measured slopes are summarized in Table 5-1. All room-temperature deposited films exhibit behavior indicative of a much lower modulus-CTE product than that typical of bulk material. The data available also suggests that there may be a change in mechanical properties with deposition pressure. That is, lower deposition pressures appear to promote properties closer to the bulk values. Also, there is an apparent dependence of film properties with the substrate temperature of deposition. High temperature deposited film results are closer to bulk property values.

The apparently extremely low modulus and/or CTE exhibited by room temperature samples may be explained by the microstructural observations made in Chapter 4. Specifically, x-ray diffraction profiles for room temperature versus high temperature deposited films indicated

that the room temperature films have lower crystallinity. Thus, it is likely that an amorphous/crystalline mixture of YSZ is present in room-temperature deposited films. The presence of this amorphous phase would reduce the in-plane biaxial modulus or effective CTE of the film.

Similar differences in microstructure due to deposition conditions may also explain the apparent dependence of properties with deposition pressure and deposition temperature. Regarding high temperature deposition, again, the more fully crystalline high temperature deposited films would likely have properties nearer typically quoted bulk values. With respect to variations with deposition pressure, high pressure depositions commonly result in films with higher porosity (*i.e*,. lower density), giving lower biaxial moduli.

Several things about this method for evaluating the mechanical properties of the film should be discussed. First, an extension of this technique may provide further insight. Depositing a film on a second substrate material, performing a stress vs. cycle experiment, and extracting this second slope would allow for the independent solution of biaxial modulus and CTE. However, this would also require characterization of the film microstructure to ensure that crystal structure, degree of crystallinity and texture are all comparable such that this technique remains appropriate. Finally, it is important to note that such techniques whereby thermal cycle data is used to infer mechanical properties have been used in the past with varying degrees of confidence and success. The possible introduction of creep deformation mechanisms and possible changes in phase and microstructure during the annealing process generally call into question the accuracy of such a technique in evaluating film properties. However, it is recognized that the lack of hysteresis during the second and subsequent cycles of YSZ films indicate that such mechanisms are not significant.

5.2.2 YSZ Strength Properties

During stress vs. temperature experiments, two room-temperature, standard deposition films were observed to crack due to the tensile stress generated during the cooling portion of their initial thermal cycle. The stress vs. temperature behavior of these films is shown in Figure 5-2. Both films shown were 274nm thick. Evidence of film cracking is seen in the sharp reduction in observed stress. Cracking was subsequently confirmed by viewing the films under an optical microscope. An example of this cracking is shown in Figure 5-3. The magnitude of stress at which this cracking behavior begins can be taken as an estimate of the ultimate strength of the film. In the films shown here, the apparent strength is between 710-750MPa. This compares to 650MPa typically quoted for bulk YSZ. The observed difference here is not unexpected considering the commonly larger strength values for film materials versus the same material in bulk form.

5.3 Nanoindentation Tests of Sputtered YSZ

As a first attempt at experimentally measuring the Young's modulus of these sputter-deposited YSZ films directly, a series of nanoindentation experiments were performed on room-temperature, unannealed, standard deposition YSZ films. Nanoindentation was selected because it was an accessible technique that makes use of a simple test sample (an unpatterned film deposited onto a substrate). The experimental techniques employed in this work follow the methods of Oliver and Pharr [105, 106], the most relevant details of which are discussed below. Although these techniques have developed into somewhat of a standard, there still exists a wide range of experimental variables that may affect the properties extracted from nanoindentation tests. Therefore, the goal of this first series of tests was not only to provide information on Young's modulus but also to provide insight into the best set of experimental indentation test

conditions for evaluating mechanical properties not only for YSZ, but also for other μSOFC materials under development. In the discussion below, important background on the experimental procedure is presented first, followed by a discussion of the results obtained for the work done here with emphasis on the particular results that will serve to guide future tests.

5.3.1 Background on Nanoindentation Testing

Evaluation of the mechanical behavior of materials using instrumented indentation techniques has enjoyed much attention in recent years. More recently, these techniques have found applications for nano-structured bulk and thin film materials not only for evaluating mechanical properties but also for exploring other phenomena such as plastic deformation and strength size effects. The work here focuses on the extraction of mechanical properties from the load-displacement behavior of a material deformed with an indenter of a particular geometry. These and similar experimental techniques rely heavily on classical contact mechanics solutions such as those presented by Hertz [107] and Boussinesq [108]. The details of these solutions are beyond the scope of this thesis and are not presented here. However, much of the background discussion below draws on the commonly cited work of Oliver and Pharr [105, 106] who, using these contact mechanics solutions and building upon and critically reviewing the work of Nix [25, 109], have established much of the commonly accepted practices for mechanical property evaluation via instrumented indentation techniques.

Nanoindentation techniques have traditionally been employed to evaluate two material properties: hardness and Young's modulus. Hardness is determined by the ratio of the indentation load (P) and the projected contact area at that load (A):

$$H = \frac{P}{A} \quad (5\text{-}13)$$

Load-displacement data is also used to determine the reduced elastic modulus (E_r) of the material by the relationship:

$$E_r = \frac{\sqrt{\pi}S}{2\beta\sqrt{A}} \quad (5\text{-}14)$$

Where S is the slope of the initial (*i.e.,* elastic unloading) portion of the unloading region of the curve, β is a constant dictated by the indenter geometry (β = 1.034 for a Berkovich three-sided pyramid tip, as used here) and A is the contact area at maximum load. This reduced modulus takes into account the fact that there is not only deformation of the material, but also (assumed elastic) deformation of the indenter. The relationship between the reduced (E_r), indenter (E_i) and material (E) modulus is:

$$\frac{1}{E_r} = \frac{1-\nu^2}{E} + \frac{1-\nu_i^{\,2}}{E_i} \quad (5\text{-}15)$$

where ν and ν_i are the Poisson's ratio of the material and the indenter, respectively. Thus, the modulus of the indented material is given by:

$$E = (1-\nu^2)\left[\frac{1}{E_r} - \frac{1-\nu_i^{\,2}}{E_i}\right]^{-1} \quad (5\text{-}16)$$

Where E_i = 1140 GPa and ν_i = 0.07 for the diamond tip used here and typically used in indentation testing.

Equations(5-13) and (5-14) make it apparent that the ability to determine hardness and Young's modulus of a test material is driven by the ability to determine accurately the contact

area of indentation at maximum load. In traditional, macroscale hardness indentation testing, this contact area is easily determined by direct measurement, typically under an optical microscope. As indentation depths and sizes have reduced over time in order to investigate phenomenon at smaller length scales, the residual indent patterns have become so small so as to make direct measurement of the contact area for every test impractical. Instead, it is common practice to determine a mathematical relationship relating the measured contact depth (h_c) to the contact area (A) for a given indenter geometry. This "area function" is determined prior to testing a material of unknown properties in one of two ways, each employing a series of indents at varying loads/depths made into a material of isotropic, depth independent, known modulus and hardness. The most common material used for this procedure is fused silica (E = 69.6 GPa). In the first technique, the contact area after unloading is measured directly using electron or atomic force microscopy. This measured area is fit to a polynomial function of the contact depth to give the area function used in subsequent testing of unknown materials. This first technique has the disadvantage of requiring sometimes difficult imaging of the indentation patterns. Furthermore, since the contact area used is that after unloading, it is also sbject to possible error caused by the elastic recovery of a portion of the contact impression. These two factors motivate the second technique, first introduced by Oliver and Pharr [105], and used in the experimental results discussed below. In this technique, an iterative process is used that not only determines an area funtion but also determines the load frame compliance (C_f), which must also be taken into account when determining the contact depth. In this procedure, the specimen and load frame are modeled as springs in series with compliances (C_s) and (C_f), respectively. Thus the total (*i.e.,* measured) compliance (C) is given by:

$$C = C_s + C_f \quad (5\text{-}17)$$

The specimen compliance is the inverse of the stiffness referred to in (5-14). Therefore the total compliance can be re-written as:

$$C = C_f + \frac{\sqrt{\pi}}{2\beta E_r}\frac{1}{\sqrt{A}} \quad (5\text{-}18)$$

With the reduced modulus of the calibration material known and the stiffness determined from the unloading portion of the load-displacement curve, one can use an initial guess of the area function to determine an initial estimate of C_f from (5-18). The initial area function used is that for a perfect indenter tip (*i.e.,* a tip of perfect geometry with no blunting etc.). For the standard Berkovich tip, this ideal area function is $A(h_c)_{berk} = 24.5h_c^2$. With an initial estimate of C_f, the contact area for each indent is re-calculated by rearranging (5-18) as:

$$A = \frac{\pi}{4}\frac{1}{E_r^2}\frac{1}{(C - C_f)^2} \quad (5\text{-}19)$$

These areas are then used to re-evaluate the area function, typically of the form:

$$A(h_c) = C_0 h_c^{\,2} + C_1 h_c^{\,1} + C_2 h_c^{\,1/2} + C_3 h_c^{\,1/4} + \ldots + C_n h_c^{\,2^{-(n+1)}} \quad (5\text{-}20)$$

The process is then repeated with this new area function until convergence is achieved.

With the resulting converged area function and load frame compliance, the reduced modulus is determined using eq. (5-18) and the experimentally determined compliance (*i.e.,* the inverse of the initial slope of the unloading curve). In the technique presented by Oliver and Pharr, it was shown that this slope/compliance is best determined by fitting the unloading portion with a power law fit of the form:

$$P = \alpha(h - h_f)^m \quad (5\text{-}21)$$

Where h_f is the residual indentation depth. The slope (S) is determined by differentiating the fitted relationship and evaluating it at the maximum indentation depth (h_{max}).

5.3.2 Experimental Methods

The test apparatus and sample preparation procedures used in the nanoindentation testing of room-temperature sputtered YSZ films are presented below.

5.3.2.1 Test Apparatus

Two indenting systems were used for evaluating the mechanical properties of sputtered YSZ films. The vast majority of the data was collected using a Hysitron Triboindenter. This system utilizes a piezoelectric loading apparatus and a three parallel-plate capacitor system to measure load and displacement. The system has a 10μN - 12mN maximum load range with a 1nN measurement resolution and a 5μm maximum displacement with 0.2 pm measurement resolution. The second system used was a Micro Materials NanoTest 600 machine with a load range of 10μN-20N and displacement range of up to 30μm with measurement resolutions down to 50μN and 0.01nm. In this system, load is applied using a voice coil system. Load measurements are inferred from measured currents in the solenoid after calibration against weight balances. Displacement is measured using a parallel plate capacitor based system.
In both systems, a three-sided pyramid Berkovich tip is used. The load frame compliances for these systems were determined using data from a series of indents on fused silica with loads ranging from 10μN – 10mN along the iterative procedure outlined by Oliver and Pharr and discussed above. In the Hysitron system, the area function used in the analysis is also experimentally determined from these indents. However, the data taken on the Micro Materials

system was analyzed using the ideal area function for a Berkovich tip.[vii] These area functions and load frame compliances are given in Table 5-2.

5.3.2.2 Sample Preparation and Test Conditions

YSZ films were sputtered at standard conditions onto 4" Si substrates. From these substrates, 0.5 – 1" square samples were cut from the center 2-3" of the wafer and mounted on the appropriate mounting fixture. In the Hysitron apparatus, this mounting fixture was a square plate of magnetic stainless steel. In the Micro Materials machine, this apparatus was a stainless steel cylinder. For both fixtures, the substrate was bonded using a thin layer of cyanoacrylate based adhesive (*i.e.*, "superglue"). Two deposited films were tested, one film approximately 1 micron thick and the other approximately 2 microns thick. These film thicknesses were used to enhance the probability that the substrate would not dramatically affect the extracted properties. Films are tested in their as-deposited state, no annealing or cycling has been performed.

After moving the indenter to a pre-programmed position, a typical indent begins with a rest period of 10s. During this time, any measured displacement is assumed to be due to thermal drift of the system. These measured displacements are used to create a drift correction factor that is applied to the loading and unloading portions of the test to remove the effects of thermal expansion on the measured loads and displacements. After the initial rest period, the sample is loaded at a specified loading rate to its maximum load, held at that maximum load for a specified period of time and then unloaded from the sample. The purpose of the hold period at maximum load was to investigate the presence of time-dependent creep-like behavior over the time scale of a particular test. In these tests, maximum loads ranged from 0.5 – 5mN with loading rates from

[vii] This is the standard operating procedure for this apparatus as it is tpyically used for relatively large indentation depths where non-ideal area functions have little effect on the analyzed data.

approximately 30 – 100μN/s. This load range was selected because resulting indentation depths are sufficiently small so as to minimize the influence of the substrate on the extracted properties. An initial rest period of 10s was used along with a hold time of either 5 s or 30 s. For a particular set of test conditions, a 6 x 6 grid of indents was performed with each indent separated by a minimum of several microns so as to avoid boundary effects of neighboring indentations.

5.3.2.3 Results

In Figure 5-4 and Figure 5-5 the observed elastic modulus as a function of average maximum load and indentation depth are presented. There was no observed correlation between film properties and other experimental conditions, such as loading rate and hold time. Therefore, for reasons that will become apparent in the subsequent discussion, the data is separated according to the indentation system and tip used. Each data point represents an average of a minimum of 35 indents. Error bars represent one standard deviation. In extracting the film modulus from the reduced modulus, the bulk value of Poisson's ratio ($\nu = 0.31$) was used.

One of the most noticeable behaviors is the differences in measured modulus given by Hysitron Tip A and the other tips used. This observation is most likely due to the inapplicability of the area function used in the analysis for the depths tested. As described above, the standard procedure for determining the indenter area function utilizes indents into fused silica with load ranges from 10μN – 10mN. Depths for these calibration indents typically range from 10's of nm to 100's of nm, with the majority of the data being taken at indentation depths above 100nm. For larger indentation depths, the depth-area relationship typically behaves more like an ideal Berkovich tip. However, in shallow indents, the depth-area relationship is affected by the inherent curvature of the tip as well as additional blunting of the tip with its use over time. Thus, it is frequently the case that the depth-area relationships for shallow indents (*i.e.*, indents on the

order of the tip radius) are better described by indentation with a spherical indenter of the same radius. The tip radii used in the data presented here are quoted from the manufacturer as being between 50nm – 100nm, making the area function a highly likely source of error in the current data at shallow indents. In order to quantitatively support this, the load-displacement behaviors from the inconsistent data done at shallow indents were re-analyzed using the ideal area function of a perfect sphere:

$$A(h_c)_{sphere} = -\pi h_c^2 + 2\pi R h_c \tag{5-22}$$

Where R is the indenter radius, taken as R=100nm. The resulting moduli are presented in Table 5-3. This re-analyzed data is more consistent with that data taken at higher indentation loads and depths, indicating the likely influence of the inappropriate area-functions. This conclusion is further supported when considering the differences in extracted modulus for indents at approximately the same depths but using different tips, such as those indents done with Tip A and B with depths between 50-70nm. Here, the two tips may have different radii, presumably with the radius of Tip B less than the radius of Tip A, so as not to be as strongly affected by the indentation depth. However, it is more likely that Tip A is more strongly affected by shallower indentation depths because, at the time of the experiment, it had been used more extensively in previous indentation experiments, causing it to blunt and wear more extensively than Tip B. Again, although the area function generally captures the effect of tip wear, it is known to be insufficient at the shallowest indentation depths. Apppropriate use of data taken at such depths requires the area function to be determined more precisely at those depths. This recommendation, along with other recommendations for future use of nanoindentation data in the mechanical property characterization of μSOFC materials are discussed in more detail in later sections.

Not considering the likely erroneous data due to the the shallow indentation effect described above, extracted Young's modulus of the film when measured by nanoindentation ranges from ~220 GPa – 280GPa. This is approximately equal or above both bulk values and upper bounds for a randomly oriented polycrystalline YSZ material presented in section 5.1. A strong possibility for the presence of a higher modulus in the out-of-plane direction is the likely presence of a (100) texture as presented in Chapter 4 and discussed with respect to expected/aggregate properties at the beginning of this chapter. In general, the question of the directionallity of the measured Young's modulus for nanoindentation tests performed on materials with high degrees of anisotropy is unresolved. As discussed by Oliver and Phar, one viewpoint is that deformation ocurs primarily in the direction normal to the film and thus the modulus will be strongly influenced by the modulus in the normal direction [105]. However, others believe that sufficient deformation ocurrs in directions oblique or parallel to the film surface for those directions to have significant influence on the measured modulus. In the data presented here, however, both viewpoints may explain the presence of a slightly higher measured modulus for YSZ. As presented above, the moduli of (100) textured YSZ crystals in directions both normal and parallel to the [100] direction are higher than those for randomly oriented polycrystalline YSZ. Of course, the deposited films are not fully textured and are likely of mixed crystalline and amorphous phases. Thus the measured modulus falling between these bounding values is to be expected.

5.4 Conclusions

A preliminary experimental evaluation of some mechanical properties of sputtered YSZ films has been presented using inferences from stress vs. temperature profiles and nanoindentation testing. Stress vs. temperature profiles indicate that YSZ films generally exhibit

a much lower in-plane biaxial modulus – CTE product than either a bulk randomly oriented YSZ material or a (100) textured film with random in-plane orientation. In contrast, when taking into account the effects of tip blunting and an inadequate area function for indentation tests at depths less than 100nm, nanoindentation tests of room-temperature deposited YSZ films indicate a Young's modulus that falls between the bounds for a randomly oriented polycrystal and a fully (100) textured crystal. Both observations may be explained in large part by the presence of a mixed amorphous/crystalline microstructure in room temperature YSZ sputtered films. Therefore, the combination of these observations with the microstructure characterization and trends in residual stress in room vs. high temperature deposited films discussed in chapter 4 lead to the belief that room-temperature YSZ films are composed of columnar crystalline phases with intergranular amorphous regions extending through the film thickness in a structure like that depicted in Figure 5-6.

More generally, these results provide important guidelines for future testing of YSZ films and other μSOFC materials owing to the exhibited combined influence of texture, microstructural phase, deposition conditions and experimental technique on the measured mechanical properties of sputtered YSZ films.

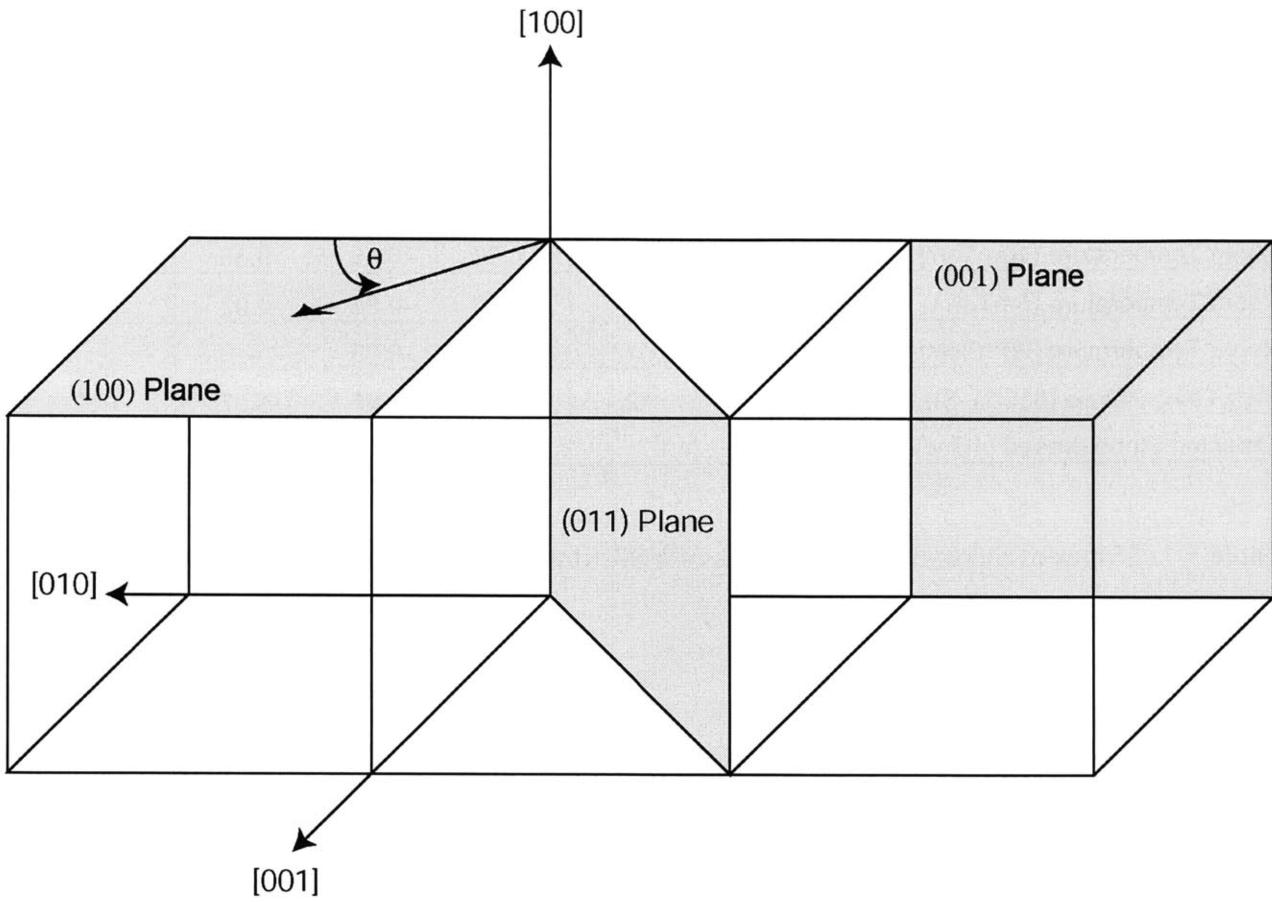

Figure 5-1: Relevant crystal directions and planes for (100) textured cubic crystals.

Deposition Conditions	No. of Samples	Slope (MPa/°C)			
		Cycle 1 - Heat	*Cycle 1 - Cool*	*Cycle 2+ - Heat*	*Cycle 2+ - Cool*
		Avg	**Avg**	**Avg**	**Avg**
Room Temperature (10mTorr)	7	-0.39	-0.45	-0.36	-0.36
Room Temperature (5mTorr)	1	-0.95	-0.96	-1.03	-1.01
Room Temperature (20mTorr)	1	-0.10	-0.05	-	-
High Temperature (600C), Standard Conditions	2	-1.82	-1.55	-1.57	-1.62
Expected Slope (based on bulk properties)	-2.26				

Table 5-1: Slopes of thermal cycling curves of YSZ films deposited under various conditions.

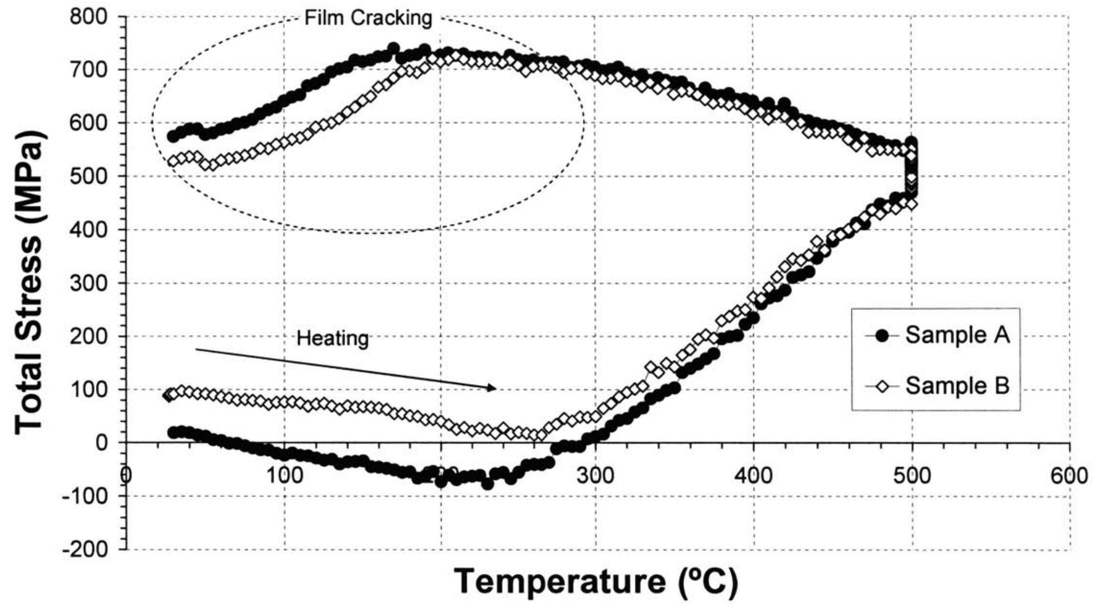

Figure 5-2: Residual stress vs. post deposition temperature of two room temperature YSZ films. Films crack during cool-down, allowing for inference of film strength.

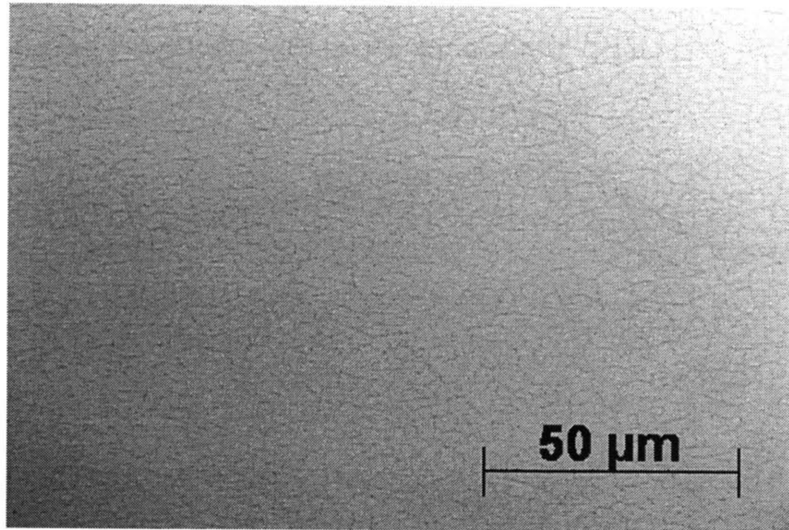

Figure 5-3: Cracking of thermally cycled YSZ film (Sample B from Figure 5-2).

		Test Apparatus			
		Hysitron - Tip A (0.5 mN max load)	Hysitron - Tip A (1mN max load)	Hysitron - Tip B	Micro Materials
	Load Frame Compliance (nm/mN)	3.25	0.89	1.1	0.691
Area Function coeffs.	**C0**	28.7425	24.5000	12.7675	24.5000
	C1	6.521E+02	9.720E+03	3.471E+02	0
	C2	4.552E+03	-1.367E+05	8.064E+02	0
	C3	7.147E+03	-1.659E+05	0	0
	C4	3.958E+03	4.079E+04	0	0
	C5	3.215E+00	7.607E+05	0	0

Table 5-2: Load frame compliances and area functions of nanoindentation tests performed.

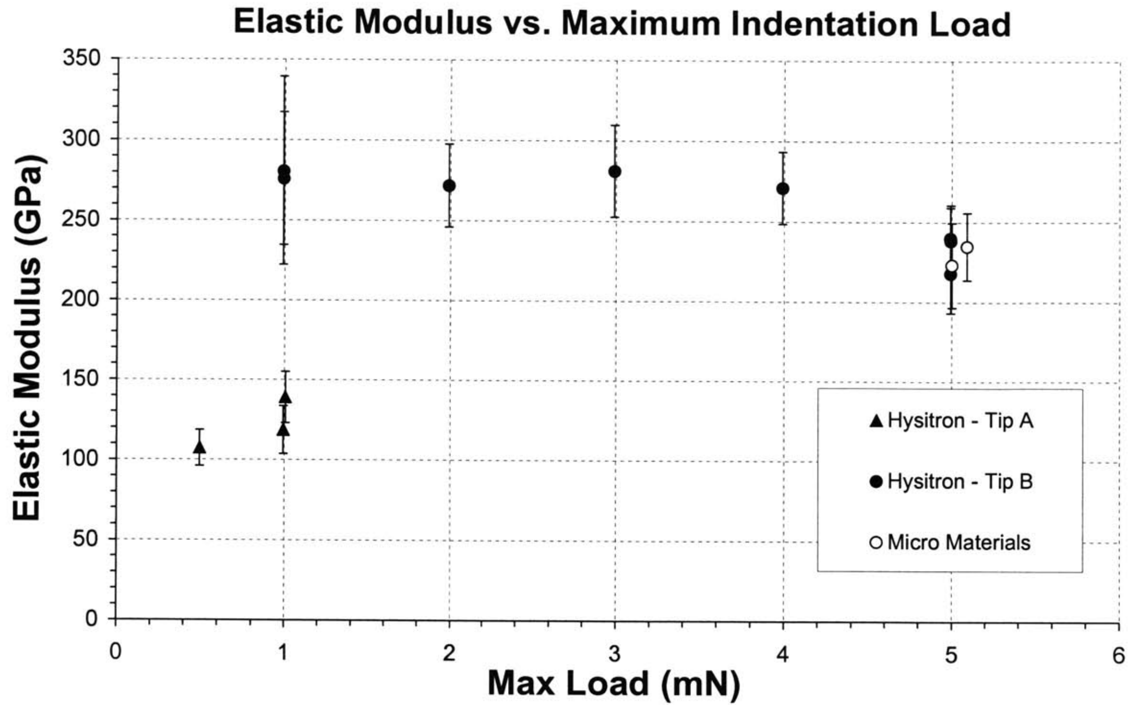

Figure 5-4: Modulus of elasticity vs. max indentation load for YSZ films sputtered under standard conditions. Data points are averages of a minimum of 35 indents. Error bars indicate one standard deviation.

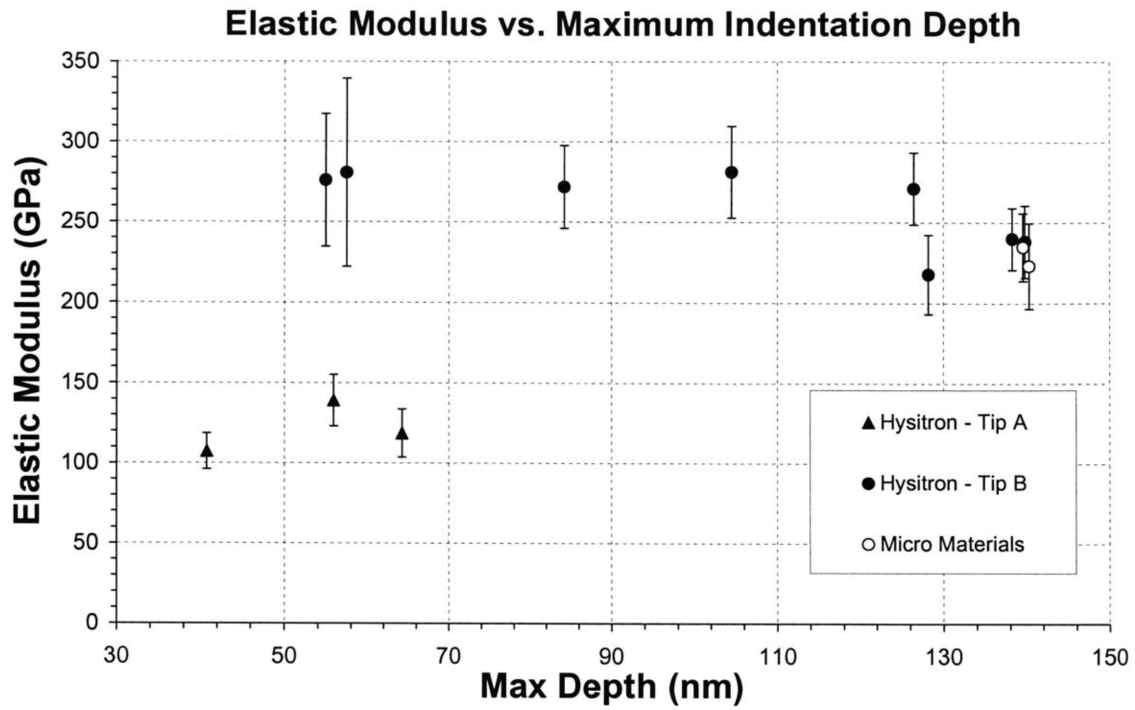

Figure 5-5: Modulus vs. maximum indentation depth for YSZ films sputtered at standard conditions and tested by nanoindentation. Error bars indicate one standard deviation.

Sample	h_{max} (nm)	Film Modulus (GPa) Determined by:	
		Experimental Berkovich Area Function	Ideal Sphere Area Function (R=100nm)
A	40.8	107	304
B	55.9	139	417
C	64.3	119	272

Table 5-3: Elastic Modulus of YSZ films indented at shallow depths and analyzed with the experimental and ideal sphere area functions

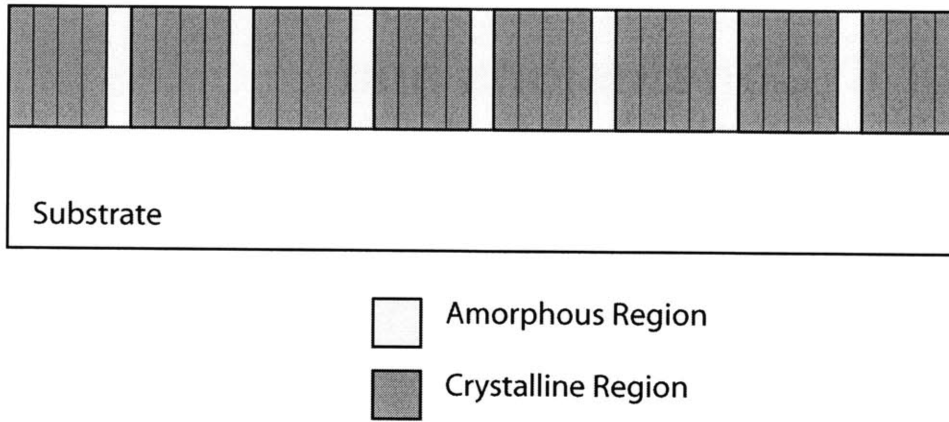

Figure 5-6: Inferred cross-sectional view of microstructure of room temperature sputtered YSZ films with mixed amorphous and columnar crystalline phases. (Not to scale)

Chapter 6: Conclusions and Recommendations for Future Work

A summary of significant results and contributions provided by the work in this thesis is first presented. This is followed by a brief discussion of the implications of these results on the design of microfabricated solid oxide fuel cell (μSOFC) devices. Finally, avenues for future work are presented.

6.1 Summary of Results and Contributions

This work has addressed the need for a preliminary understanding of material microstructure and properties in the development of a μSOFC. Much of the focus of this work is on characterizing the residual stress of sub-micron thick sputter deposited yttria stabilized zirconia (YSZ), a likely μSOFC electrolyte material. The major conclusions and contributions of this work are highlighted below and are grouped according to those related to room temperature (25°C, standard) and high temperature (600°C) deposited YSZ films.

The major conclusions regarding YSZ films deposited at room temperature are:

- Due to electron bombardment during the sputtering process, the substrate temperature reaches ~185°C during deposition at nominally "room temperature".
- YSZ films sputtered under "standard" conditions (*i.e.*, $<1 \times 10^{-6}$ Torr base pressure, 10mTorr working pressure, 9:1 Ar/O_2) at room temperature and thicknesses < 1μm have nearly stoichiometric composition with evidence of columnar microstructure.

- Crystalline phases of sputtered YSZ films under "standard" conditions on single crystal (100) silicon are fully cubic and indicate a likely (100) normal texture. However, when compared to XRD results from high temperature films, it appears likely that room-temperature films are not fully crystalline and likely possess mixed amorphous and crystalline regions.
- Preliminary mechanical property assessments of room-temperature films via thermal cycling and nanoindentation indicate the possibility of low in-plane moduli compared to bulk values for YSZ, whereas the out-of-plane modulus appears more comparable to the bulk. This combination of mechanical property and microstructural characterization are consistent with the presence of intergranular amorphous regions in the room-temperature YSZ films.
- As-deposited residual stresses of room-temperature sputtered YSZ films are large. Those deposited under "standard" conditions range from approximately -1.3GPa to 200MPa for thicknesses between ~10nm and ~1μm; thinner films are highly compressive and thicker films exhibit less compressive or mildly tensile stress.
- Increasing film stress with thickness for "standard" films is also accompanied by general grain evolution (*i.e.* evolution of grain clusters) and increased grain size (grain size increases from ~17nm – 40nm with film thicknesses increasing from ~250nm – 1μm).
- As-deposited stress is a strong function of working pressure. For a given film thickness, variations in working pressure of deposition can lead to a transition in as-deposited stress from compressive to tensile. For ~250nm thick films, this transition occurs between 10mTorr and 20mTorr.

- Secondary ion mass spectroscopy (SIMS) characterization data indicate that impurity content is likely not a significant stress generation or relief mechanism.
- The two dominant mechanisms that control the as-deposited residual stress state of sputtered YSZ films are compressive stress generated by implanted surface interstitials (*i.e.,* "atomic peening") and tensile stress generated during the coalescence and growth of (columnar) grains. Reduction in compressive stress levels with thickness, working pressure and time (*i.e.,* for different series of depositions) can all be explained through the decreasing severity of the "atomic peening" compressive stress mechanism and domination of tensile stresses developed during grain coalescence.
- Stress hysteresis during thermal cycling of room-temperature deposited YSZ up to 500°C can be as large as ~1GPa tensile, causing a transition in stress state from compressive to tensile. This hysteresis is mechanistically explained by relief of compressive "peening" stresses via free surface diffusion (as opposed to bulk or grain boundary diffusion), allowing for a net tensile film stress. Results indicate that this stress hysteresis is not due to diffusive release of implanted sputtering gasses.
- Preliminary mechanical property characterizations of room-temperature YSZ films indicate an in-plane modulus-CTE product, inferred from thermal cycling data, ranging from 0.05 – 1.62 MPa/°C, significantly lower than the typical bulk value of 2.26 MPa/°C. However, the out-of-plane Young's modulus, as measured by nanonindentation, appears comparable to or slightly higher than bulk values (~200 - 250GPa) but lower than the single crystal modulus in the [100] direction (410 GPa). Again, these observations are likely due to the presence of mixed amorphous/crystalline phases in room temperature deposited films where the crystalline phase exhibits a predominantly (100) texture.

The following are the major conclusions regarding YSZ films deposited at high temperatures (600°C):

- X-ray diffraction profiles of YSZ films deposited at high temperature (600°C) indicate increased crystallinity compared to room temperature depositions. As mentioned previously, this motivates the more general conclusion that room temperature deposited YSZ films have mixed amorphous/crystalline domains.
- As-deposited stresses in high temperature (600°C) deposited YSZ films are large and range from approximately -1.4GPa to 400MPa with thicknesses from 50nm to 700nm.
- High temperature depositions exhibit similar trends as room temperature deposited films, namely decreased compressive stress with increasing thickness and working pressure. These trends are again explained by competing compressive and tensile stress mechanisms due to atomic peening and grain coalescence/growth. However, higher magnitudes of stress are observed. That is, where stress is compressive, it is more compressive and where stress is tensile it is more tensile than room temperature films. This behavior may be attributed to enhanced crystallinity which would serve to increase the magnitude of net compressive stress in the peening-dominated regimes (*i.e.,* thinner films and low working pressures) as well as the magnitude of tensile stress in the grain-coalescence dominated regimes (*i.e.* thicker films and higher working pressures).

Finally, preliminary work on co-sputtered Pt-YSZ and representative fuel cell trilayers (Pt-YSZ/YSZ/Pt-YSZ) indicates that the as-deposited and post thermal cycle residual stress states

may be either compressive or tensile. There appear to be contributions from peening stresses, plastic deformation, and perhaps other unidentified mechanisms influencing the final stress state.

6.2 Implications for μSOFC Device Design and Fabrication

As discussed in Chapter 1, μSOFC device structures may fail by a variety of mechanisms, driven in-part by large residual tensile or compressive stresses quantified for YSZ in this thesis. Generally speaking, compressive stresses will increase the likelihood of buckling while significant tensile stress will cause fracture. Both large compressive and tensile stress will increase the likelihood of decohesion or delamination failures. Thus, one may use the results of this work to determine the appropriate set of deposition conditions necessary to produce released structures under intermediate levels of stress. Specifically, reducing the level of net compressive stress may be achieved by depositing thicker films or depositing at working pressures greater than 20mTorr. However, considering an estimate of the compressive stress generated in a released YSZ membrane on silicon heated to 600°C (~1500MPa), it is unlikely that compressive stress can be eliminated in a structure at operating temperatures. Alternatively, it is possible that large freestanding fuel cell membranes may function properly in a post-buckled regime, provided fracture can be avoided. In this case, it is desirable to have an initial stress state that is either sufficiently compressive or mildly tensile such that the membrane is driven sufficiently compressive during operation. Such a design motivates the deposition of YSZ films at low to intermediate thicknesses and working pressures.

This work also illustrates the need for consideration of high-temperature processing steps during the design of fabrication and packaging routes. It is clear that the intrinsic stress state changes significantly with temperature. Therefore, any subsequent high temperature processes

during fabrication and packaging must be considered within the context of the structural stability of unreleased films or released membranes. For example, it was established that the generation of tensile stress during post deposition thermal cycles may lead to tensile stresses large enough to cause cracking of unreleased films. In order to guard against this, one could deposit films at higher pressures, which were observed to exhibit lower levels of tensile stress evolution. Also, in a final μSOFC structure, fabrication routes could be designed such that all supporting structural layers are deposited prior to any high temperature thermal cycling processes and membrane release to guard against cracking/fracture of the electrolyte layer. These above considerations firmly establish the importance of this work in the development of viable μSOFC devices.

6.3 Recommendations for Future Work

This work represents progress in important materials and mechanical aspects of μSOFC device development. However, these results lead to several additional questions and areas for continued investigation. Those questions and areas are presented below.

- The as-deposited residual stress state should be characterized for a wider range of processing conditions. For example, thicker films may be of interest for enhanced thermostructural stability. In addition, characterization of variations with additional processing parameters such as gas ratios, sputtering power and target (*i.e.,* film) composition should be undertaken to develop greater understanding of residual stress management.
- In order to firmly establish the reason for the decrease in compressive film stress over time (*i.e.*, series 1 versus series 2 depositions), characterization of film stress vs.

thickness for a new (*i.e.,* unworn) sputtering target should be undertaken. One would expect a new target to lead to more compressive film stresses.

- More data is required on high and intermediate temperature depositions to adequately map the range of stress states achievable.
- It would generally be desirable to investigate the stress evolution with temperature up to temperatures near 800-1000°C, as these temperatures more closely mimic operating conditions of SOFC's. This work was limited by the apparatus available for such investigation. Thus, either the use of another yet unidentified apparatus or the design of a new apparatus should be considered.
- In addition to stress development at higher temperatures, the crystallographic structure of room and high temperature deposited YSZ should be monitored when taken to higher temperatures, primarily to further investigate the possibility of crystallization during post-deposition annealing. Such tests may be done using the same Bruker D8 Diffractometer used in this thesis with a heating stage accessory capable of temperatures near 1000°C. (Note: This accessory was not available during the course of this work, but has become available since the completion of this thesis.)
- More consideration should be given to the stress mechanisms active in the potential Pt-YSZ anode/cathode material and its influence on the net stress state of fuel cell stacks. A similar approach as that taken in this thesis is recommended.
- As μSOFC device concepts continue to develop, an appropriate subset of these experiments must be performed for material systems more closely resembling those that will be used in an μSOFC device. Because the electrolyte layer will likely be deposited onto an anode/cathode material, rather than a Si wafer, its microstructure may be

different than the films deposited here. However, it is believed that the trends and mechanisms observed here will generally be present in any material system utilizing the YSZ electrolyte.

- It is clear that the mechanical properties of these deposited films vary significantly from their bulk counterparts. This is likely due in part to the presence of mixed amorphous/crystalline phases. This brings about two recommendations:
    - More rigorous and traditional mechanical property characterization techniques (*i.e.,* bulge testing, beam bending and micro tensile testing) should be explored. However, it should be noted that additional nanoindentation tests should also be pursued, specifically a parallel set of tests on high temperature films, where one would expect a further increase in the modulus normal to the film due to the apparent enhanced crystallization and texture. Additionally, nanoindentation tests may be coupled with more rigorous testing methods to establish baseline property measurements from which variations with changing processing parameters can be quickly inferred due to the relative simplicity of the nanoindentation technique.
    - Advanced techniques, specifically using X-ray diffraction, should be explored to quantify crystalline vs. amorphous phase content of deposited films. This should be done in parallel with the mechanical property work described above and should also be used to further asses the validity of the conclusions reached in this work regarding the underlying residual stress mechanisms active in sputtered YSZ films.
- Thermo-mechanical testing of representative μSOFC device structures should be carried out and compared to predictions from structural models utilizing the residual stress data

presented here as an input. Such tests may ultimately reveal the need for further stress characterization techniques, specifically those related to stress gradients through film thickness.

This thesis has provided important insight into the materials issues related to the development of structurally viable μSOFC devices. These contributions, as well as completion of the additional work identified above will help lead to the development and potentially wide-spread use of μSOFC devices.

References

[1] B. Sorensen, *Hydrogen and Fuel Cells: Emerging technologies and applications*. Amsterdam: Elsevier Academic Press, 2005.

[2] S. Singhal and K. Kendall, *High Temperature Solid Oxide Fuel Cells: Fundamentals, Design and Applications*. New York, NY: Elsevier, 2003.

[3] "Basic Research Needs for the Hydrogen Economy," Argonne National Laboratory, U.S. Department of Energy, Chicago, IL May 13-15 2003.

[4] B. C. H. Steele, "Material science and engineering: The enabling technology for the commercialisation of fuel cell systems," *Journal of Materials Science*, vol. 36, pp. 1053-1068, 2001.

[5] B. C. Steele and A. Heinzel, "Materials for fuel-cell technologies," *Nature*, vol. 414, pp. 345-352, 2001.

[6] B. C. H. Steele, "Materials for high-temperature fuel cells," *Philosophical Transactions: Mathematical, Physical and Engineering Sciences*, vol. 354, pp. 1695-1710, 1996.

[7] A. Jankowski, R. Graff, J. Hayes, and J. Morse, "Testing of solid-oxide fuel cells for micro to macro power generation," presented at Joint International Meeting of the Electrochemical Society, Honolulu, HI, 1999.

[8] A. Jankowski, J. P. Hayes, R. T. Graff, and J. D. Morse, "Micro-fabricated thin-film fuel cells for portable power requirements," *Materials Research Society Symposium Proceedings*, vol. 730, 2002.

[9] X. Chen, N. J. Wu, L. Smith, and A. Ignatiev, "Thin-film heterostructure solid oxide fuel cells," *Applied Physics Letters*, vol. 84, pp. 2700-2702, 2004.

[10] P. Charpentier, P. Fragnaud, D. M. Schliech, and E. Gehain, "Preparation of thin film SOFCs working at reduced temperature," *Solid State Ionics*, vol. 135, pp. 373-380, 2000.

[11] Z. Shao, S. M. Haile, J. Ahn, P. Ronney, Z. Zhan, and S. Barnett, "A thermally self-sustained micro solid-oxide fuel-cell stack with high power density," *Nature*, vol. 435, pp. 795-798, 2005.

[12] K. Honegger, E. Batawi, C. Sprecher, and R. Diethelm, "Thin Film Solid Oxide Fuel Cell (SOFC) for Intermediate Temperature Operation (700C)," presented at Fifth International Symposium on Solid Oxide Fuel Cells, 1997.

[13] C. D. Baertsch, K. F. Jensen, J. L. Hertz, H. L. Tuller, V. T. S. Vengallatore, S. M. Spearing, and M. A. Schmidt, "Fabrication and structural characterization of self-supporting electrolyte membranes for a micro solid-oxide fuel cell," *Journal of Materials Research*, vol. 19, pp. 2604-2615, 2004.

[14] J. E. Ashton and M. E. Waddrups, "Analysis of anisotropic plates," *Journal of Composite Materials*, pp. 148-165, 1969.

[15] M. Madou, *Microfabrication*. Boca Raton: CRC Press, 2002.

[16] S. M. Rossnagel, "Sputter deposition for semiconductor manufacturing," *IBM Journal of Research and Development*, vol. 43, pp. 163-179, 1999.

[17] J. Hopwood, "Plasma-assisted deposition," in *Handbook of Nanophase Materials*, A. Goldstein, Ed.: Marcel Dekker Inc., 1997, pp. 141-197.

[18] M. Ohring, *Materials Science of Thin Films*, 2nd ed: Academic Press, 2002.

[19] S. Berg, H. O. Blom, M. Moradi, and C. Nender, "Process modeling of reactive sputtering," *Journal of Vacuum Science and Technology A*, vol. 7, pp. 1225-1229, 1989.

[20] H. Windischmann, "Intrinsic stress in sputter-deposited thin films," *Critical Reviews in Solid State and Materials Sciences.*, vol. 17, pp. 547, 1992.

[21] H. D. Hagstrum, "Reflection of noble gas ions at solid surfaces," *Physical Review*, vol. 38, pp. 340, 1961.

[22] G. K. Wehner and G. S. Anderson, "The nature of physical sputtering," in *Handbook of Thin film Technology*, L. I. Maissel and R. Glang, Eds. New York: McGraw-Hill, 1970.

[23] L. B. Freund and S.Suresh, *Thin Film Materials: Stress, Defect Formation and Surface Evolution*. Cambridge, UK: Cambridge University Press, 2003.

[24] D. W. Hoffman, "Perspective on stresses in magnetron-sputtered thin films," *12*, vol. 12, pp. 953-961, 1994.

[25] M. F. Doerner and W. D. Nix, "Stresses and deformation processes in thin films on substrates," *Critical Reviews in Solid State and Materials Sciences.*, vol. 14, pp. 225-268, 1988.

[26] R. W. Hoffman, "The mechanical properties of non-metallic thin films," in *Physics of Nonmetallic Thin Films*, vol. B-14, *NATO Advanced Study Institute Series*, C. H. S. Dupuy and A. Cachard, Eds. Plenum, NY, 1976, pp. 273.

[27] F. A. Doljack and R. W. Hoffman, "The origin of stress in thin nickel films," *Thin Solid Films*, vol. 12, pp. 71, 1972.

[28] W. D. Nix and B. M. Clemens, "Crystallite coalescence: A mechanim for intrinsic tensile stresses in films," *Journal of Materials Research*, vol. 14, pp. 3467-3473, 1999.

[29] L. B. Freund and E. Chason, "Model for stress generated upon contact of neighboring islands on the surface of a substrate," *Journal of Applied Physics*, vol. 89, pp. 4866-4873, 2001.

[30] Abermann, Kramer, and Maser, "Structure and internal stress in ultra-thin silmver films deposited on MgF2 and SiO substrates," *Thin Solid Films*, vol. 52, pp. 215-229, 1978.

[31] C. V. Thompson and R. Carel, "Stress and grain growth in thin films," *Journal of the Mechanics and Physics of Solids*, vol. 44, pp. 657-673, 1996.

[32] P. Chaudhari, "Grain growth and stress relief in thin films," *Journal of Vacuum Science and Technology*, vol. 9, pp. 520-522, 1971.

[33] J. A. Floro, S. J. Hearne, J. A. Hunter, and P. Kotula, "The dynamic competition between stress generation and relaxation mechanisms during coalescence of Volmer-Weber thin films," *Journal of Applied Physics*, vol. 89, pp. 4886-4897, 2001.

[34] J. A. Floro, E. Chason, R. C. Cammarata, and D. Srolovitz, "Physical origins of intrinsic stresses in Volmer-Weber thin films," *MRS Bulletin*, pp. 19-25, 2002.

[35] J. A. Floro, E. Chason, R. C. Cammarata, and D. J. Srolovitz, "Physical origins of intrinsic stresses in Volmer-Weber thin films," *MRS Bulletin*, pp. 19-25, 2002.

[36] R. C. Cammarata and T. M. Trimble, "Surface stress model for intrinsic stresses in thin films," *Journal of Materials Research*, vol. 15, pp. 2468-2474, 2000.

[37] R. W. Hoffman, "Stress in thin films: the relevance of grain boundaries and impurities," *Thin Solid Films*, vol. 34, pp. 185-190, 1976.

[38] H. M. Choi and S. K. Choi, "Origin of intrinsic stress in Y2O3 films deposited by reactive sputtering," *Journal of Vacuum Science and Technology A*, vol. 13, pp. 2832-2835, 1995.

[39] X. Zhang, K. S. Chen, R. Ghodssi, A. A. Ayon, and S. M. Spearing, "Residual stress and fracture in thick tetraethylorthosilicate (TEOS) and Silane-Based PECVD Oxide Films," *Sensors and Actuators A: Physical*, vol. 91, pp. 379-386, 2001.

[40] E. V. Kornelsen, "The ionic entrapment and thermal desorption of inert gases in tungsten for kinetic energies of 40eV to 5keV," *Canadian Journal of Physics*, vol. 42, pp. 364, 1964.

[41] C. T. Wu, "Intrinsic stress of magnetron-sputtered niobium films," *Thin Solid Films*, vol. 64, pp. 103, 1979.

[42] J. A. Thornton, J. Tabock, and D. W. Hoffman, "Internal stress in metallic films deposited by cylindrical magnetron sputtering," *Thin Solid Films*, vol. 64, pp. 111, 1979.

[43] P. Sigmund, "Theory of sputtering I: Sputtering yield of amorphous and polycrystalline targets," *Physical Review*, vol. 184, pp. 383, 1969.

[44] H. Windischmann, "An intrinsic stress scaling law for polycrystalline thin films prepared by ion beam sputtering," *Journal of Applied Physics*, vol. 62, pp. 1800, 1987.

[45] D. W. Hoffman and M. R. Gaerttner, "Modification of evaporated chromium by concurrent ion bombardment," *Journal of Vacuum Science and Technology*, vol. 17, pp. 425, 1980.

[46] D. Nir, "Intrinsic stress in diamond-like carbon films and its dependence on deposition parameters," *Thin Solid Films*, vol. 146, pp. 27, 1987.

[47] Z. Ji, A. Haynes, E. Voelkl, and J. M. Rigsbee, "Phase formation and stability in reactively sputter deposited yttria-stabilized zirconia coatings," *Journal of the American Ceramics Society*, vol. 84, pp. 929, 2001.

[48] E. C. Subbarao, "Zirconia: An Overview," in *Advances in Ceramics*, vol. 3, A. H. Heuer and L. W. Hobbs, Eds.: American Ceramic Society, 1981.

[49] Z. Ji and J. M. Rigsbee, "Growth of tetragonal zirconia coatings by reactive sputter deposition," *Journal of the American Ceramics Society*, vol. 84, pp. 2841, 2001.

[50] *High Temperature Solid Oxide Fuel Cells - Fundamentals, Design and Applications*. Oxford, UK, 2003.

[51] P. Gao, L. J. Meng, M. P. d. Santos, V. Teixeira, and M. Andritschky, "Study of ZrO_2 - Y_2O_3 films prepared by rf magnetron reactive sputtering," *Thin Solid Films*, vol. 377/378, pp. 32-36, 2000.

[52] J. Will, A. Mitterdorfer, C. Kleinlogel, D. Perednis, and L. J. Gauckler, "Fabrication of thin electrolytes for second-generation solid oxide fuel cells," *Solid State Ionics*, vol. 131, pp. 79-96, 2000.

[53] R. W. Knoll and E. R. Bradley, "Correlation between the stress and microstructure in bias-sputtered ZrO_2 - Y_2O_3 films," *Thin Solid Films*, vol. 117, pp. 201-210, 1984.

[54] D. Ruddell, B. Stoner, and J. Y. Thompson, "Effect of deposition interruption and substrate bias on the structure of sputter-deposited yttria-stabilized zirconia thin films," *Journal of Vacuum Science and Technology A*, vol. 20, pp. 1744-1748, 2002.

[55] W. T. Pawlewiez and D. D. Hays, "Microstructure control for sputter deposited ZrO2, ZrO2-CaO, and ZrO2 - Y2O3," *Thin Solid Films*, vol. 94, pp. 31-45, 1982.

[56] R. W. Knoll and E. R. Bradley, "Microstructure and phase composition of sputter-deposited zirconia-yttria films," *Materials Research Society Symposium Proceedings*, vol. 30, pp. 235-243, 1984.

[57] B. Y. Liaw, R. E. Rocheleau, and Q. Gao, "Thin film yttria-stabilized tetragonal zirconia," *Solid State Ionics*, vol. 92, pp. 85, 1996.

[58] D. Ruddell, B. Stoner, and J. Y. Thompson, "The effect of deposition parameters on the properties of yttria-stabilized zirconia thin films," *Thin Solid Films*, vol. 445, pp. 14-19, 2003.

[59] K. Stamper, D. W. Greve, and T. E. Schlesinger, "Deposition of textured yttria-stabilized ZrO_2 films on oxidized silicon," *Journal of Applied Physics*, vol. 70, pp. 2046-2051, 1991.

[60] A. F. Jankowski and J. P. Hayes, "Reactive sputter deposition of yttria-stabilized zirconia," *Surface and Coatings Technology*, vol. 76-77, pp. 126-131, 1995.

[61] J. O. Carneiro, V. Teixeira, A. Portinha, F. Vaz, and J. A. Ferreira, "A real time scale measurement of residual stress evolution during coating deposition using electric extensometry," *Reviews of Advanced Materials Science*, vol. 7, pp. 32-40, 2004.

[62] Y. K. Lee and J. W. Park, "Optical properties and stresses of RF magnetron sputtered yttria-stabilized zirconia thin films," *Journal of Materials Science Letters*, vol. 15, pp. 1513-1516, 1996.

[63] T. G. Bifano, H. T. Johnson, P. Bierden, and R. K. Mali, "Elimination of stress-induced curvature in thin-film structures," *Journal of Microelectromechanical Systems*, vol. 11, pp. 592-597, 2002.

[64] V. T. Srikar, K. Turner, T.-Z. A. Ie, and S. M. Spearing, "Structural design considerations for micromachined solid oxide fuel cells," *Journal of Power Sources*, vol. 125, pp. 62-69, 2004.

[65] V. Ziebart, O. Paul, and H. Baltes, "Strongly buckled square micromachined membranes," *Journal of Microelectromechanical Systems*, vol. 8, pp. 423-432, 1999.

[66] K. F. Jensen, "Microchemical systems for fuel processing and conversion to electrical power - MURI Review," U.S. Army Research Office, 42236-CH-MUR, 2005.

[67] V. T. Srikar and S. M. Spearing, "A critical review of microscale mechanical testing methods used in the design of microelectromechanical systems," *Experimental Mechanics*, vol. 43, pp. 238-247, 2003.

[68] G. G. Stoney, "The tension of metallic films deposited by electrolysis," *Proceedings of the Royal Society of London, Series A*, vol. 82, pp. 172-175, 1909.

[69] M. Finot, I. A. Blech, S. Suresh, and H. Fujimoto, "Large deformation and geometric instability of substrates with thin-film deposits," *Journal of Applied Physics*, vol. 81, pp. 3457-34-64, 1997.

[70] L. B. Freund, J. A. Floro, and E. Chason, "Extensions of the stoney formula for substrate curvature to configurations with thin substrates or large deformations," *Applied Physics Letters*, vol. 74, pp. 1987-1999, 1999.

[71] F. J. v. Preissig, "Applicability of the classical curvature-stress relation for thin films on plate substrates," *Journal of applied Physics*, vol. 66, pp. 4262-4268, 1989.

[72] D. E. Fahnline, C. B. Masters, and N. J. Salamon, "Thin film stress from nonspherical substrate bending measurements," *Journal of Vacuum Science and Technology A*, vol. 9, pp. 2483-2487, 1991.

[73] T. S. Park, S. Suresh, A. J. Rosakis, and J. Ryu, "Measurement of full-field curvature and geometrical instability of thin film-substrate systems through CGS interferometry," *Journal of the Mechanics and Physics of Solids*, vol. 51, pp. 2191-2211, 2003.

[74] M. Finot and S. Suresh, "Small and large deformation of thick and thin-film multi-layers: effects of layer geometry, plasticity and compositional gradients," *Journal of the Mechanics and Physics of Solids*, vol. 44, pp. 683-721, 1996.

[75] A. J. Rosakis, R. B. Singh, Y. Tsuji, E. Kolawa, and N. R. Moore, "Full field measurements of curvature using coherent gradient sensing - application to thin-film characterization," *Thin Solid Films*, vol. 325, pp. 42-54, 1998.

[76] P. Romanus, Advanced Energy Inc. December 3 2003.

[77] J. Hertz, "Personal Communications," 2003-2005.

[78] D. C. Baird, *Experimentation: An Introduction to Measurement Theory and Experiment Design*. Englewood Cliffs, NJ: Prentice-Hall, 1962.

[79] "Tencor FLX 2320 User Manual."

[80] R. C. Garvie, R. H. Hannick, and R. T. Pascoe, "Ceramic Steel?," *Nature*, vol. 258, pp. 703-704, 1975.

[81] R. C. Garvie, "Stabilization of the tetragonal structure in zirconia microcrystals," *Journal of Physical Chemistry*, vol. 82, pp. 218-224, 1978.

[82] P. G. Quigley, R. A. Rao, and C. B. Eom, "Time dependence and spatial distribution of the deposition rate of YBa2Cu3O7 thin films in 90degree off-axis sputtering.," *Journal of Vacuum Science and Technology A*, vol. 15, pp. 2854-2858, 1997.

[83] T. J. Chung, H. Song, G. H. Kim, and D. Y. Kim, "Microstructure and phase stability of yttria-doped tetragonal zircoina polycrystals heat treated in nitrogetn atmosphere," *Journal of the American Ceramics Society*, vol. 80, pp. 2607-2612, 1997.

[84] D. Fong, "Stresses in Cu Thin Films and Ag/Ni Multilayers," in *Division of Engineering and Applied Sciences*. Cambridge: Harvard University, 2001, pp. 198.

[85] M. Harting, T. Ntsoane, and R. Bucher, "Influence of annealing on the residual stress in sputter-deposited platinum films," *Advanced Engineering Materials*, vol. 4, pp. 607-609, 2002.

[86] T. Hodge, S. Bidstrup-Allen, and P. Kohl, "Stresses in thin film metallization," *IEEE Transactions on Components, Packaging and Manufacturing Technology - Part A*, vol. 20, pp. 241-251, 1997.

[87] Y. Estrin, G. Gottstein, E. Rabkin, and L. S. Shvindlerman, "Grain growth in thin metallic films," *Acta Materiala*, vol. 49, pp. 673-681, 2001.

[88] R. W. Balluffi and J. M. Blakely, "Special aspects of diffusion in thin films," *Thin Solid Films*, vol. 25, pp. 363, 1975.

[89] N. A. Gjostein, *Diffusion*. Metals Park, OH: American Society for Metals, 1973.

[90] C. Laberty-Robert, F. Ansart, C. Deloget, M. Gaudon, and A. Rousset, "Powder synthesis of nanocrystalline ZrO2-8%Y2O3 via a polymerization route," *Materials Research Bulletin*, vol. 36, pp. 2083-2101, 2001.

[91] I. Kosacki, T. Suzuki, V. Petrovski, and H. Anderson, "Electrical conductivity of nanocrystalline ceria and zirconia thin films," *Solid State Ionics*, vol. 136-137, pp. 1225-1233, 2000.

[92] Y. Okada and Y. Tokumaru, "Precise determination of lattice parameter and thermal expansion coefficient of silicon between 300 and 1500K," *Journal of Applied Physics*, vol. 56, pp. 314-320, 1984.

[93] S. M. Spearing, "Materials Issues in Microelectromechanical Systems (MEMS)," *Acta Metallurgica Materiala*, vol. 48, pp. 179-196, 2000.

[94] E. Arzt, "Overview No. 130: Size effects in materials due to microstructural and dimensional constraints: A comparative review," *Acta Metallurgica Materiala*, vol. 46, pp. 5611-5626, 1998.

[95] H. D. Espinosa and B. C. Prorok, "Size Effects on the Mechanical Behavior of Gold Thin Films," presented at ASME 2001 International Mechanical Engineering Congress and Exposition: Symposium on Mechanical Properties of MEMS Structures, New York, 2001.

[96] N. A. Fleck, G. M. Muller, M. F. Ashby, and J. W. Hutchinson, "Strain gradient plasticity: Theory and experiment," *Acta Metallurgica Materiala*, vol. 42, pp. 475-487, 1994.

[97] W. N. Sharpe, S. Brown, G. Johnson, and W. Knauss, "Round-robin tests for modulus and strength of polysilicon," presented at Materials Research Society Spring Meeting: Microelectromechanial Structures for Materials Research, San Franciso, CA, 1998.

[98] W. N. Sharpe, K. Jackson, K. Hemker, and Z. Xie, "Effect of Specimen Size on Young's Modulus and Fracture Strength of Polysilicon," *Journal of Microelectromechanical Systems*, vol. 10, pp. 317-326, 2001.

[99] R. Ingel and D. Lewis, "Elastic anisotropy in zirconia single crystals," *Journal of the American Ceramics Society*, vol. 71, pp. 265-271, 1988.

[100] R. P. Ingel and D. Lewis, "Lattice parameters and density for Y_2O_3-stabilized ZrO_2," *Journal of the American Ceramics Society*, vol. 69, pp. 325-332, 1986.

[101] H. M. Kandil, J. D. Greiner, and J. F. Smith, "Single-crystal elastic constants of yttria-stabilized zirconia in the range 20 to 700C," *Journal of the American Ceramics Society*, vol. 67, pp. 341-346, 1984.

[102] R. Hill, "The elastic behaviour of a crystalline aggregate," *Proceedings of the Physical Society of London. Sect. A*, vol. 65, pp. 439-454, 1952.

[103] J. F. Nye, *Physical Properties of Crystals*. Oxford: Oxford Science Publications, 1957.

[104] W. A. Brantley, "Calculated elastic constants for stress problems associated with semiconductor devices," *Journal of Applied Physics*, vol. 44, pp. 534-535, 1973.

[105] W. C. Oliver and G. M. Pharr, "An improved technique for determining hardness and elastic modulus using load and displacement sensing indentation experiments," *Journal of Materials Research*, vol. 7, pp. 1564-1583, 1992.

[106] W. C. Oliver and G. M. Pharr, "Measurement of hardness and elastic modulus by instrumented indentation: Advances in understanding and refinements to methodology," *Journal of Materials Research*, vol. 19, pp. 3-20, 2004.

[107] H. Hertz, *J. reinc und angewandte Mathematik*, vol. 92, pp. 156, 1882.

[108] J. Boussinesq, *Applications des Potentiels a l'etude de equilibre et du mouvement des solides elastiques*. Paris: Gauthier-Villars, 1885.

[109] M. F. Doerner and W. D. Nix, *Journal of Materials Research*, vol. 1, pp. 601, 1986.